Seconda Università degli Studi di Napoli

Facoltà di Ingegneria

Corso di Laurea in Ingegneria Aerospaziale

TESI di LAUREA

Performance Evaluation and Simulation of the Laser Altimeter for Topographic Analysis of Ganymede during Europa Jupiter System Mission

Relatore

Ch.mo Prof. Ing. **Marco D'Errico**
Dipartimento di Ingegneria Aerospaziale e Meccanica

Candidato

Carlo Cauli
Matr. 831/223

Correlatore

Dott.ssa **M. Rosaria Santovito**
Consorzio di Ricerca su Sistemi di Telesensori Avanzati
Co.Ri.S.T.A. - Napoli

Anno Accademico 2007-2008

Ai miei genitori, insostituibili

A Veronica, l'amore della mia vita

TABLE of CONTENTS

INTRODUCTION

This study has been developed at CO.RI.S.T.A. (Consortium for Research on Advanced Remote Sensing Systems) in Naples in the framework of *Europa Jupiter System Mission* (*EJSM*), a future mission of *ESA Cosmic Vision* program, devoted to the exploration of Jupiter and its four major moons (the so-called Galilean satellites). *EJSM* will see the collaboration of the *NASA* (National Aeronautics and Space Administration), *ESA* (European Space Agency) and *JAXA* (Japan Aerospace Exploration Agency) which are separately studying three spacecrafts, for three different targets in Jovian system.

The spacecraft under *ESA* responsibility, called *Jupiter Ganymede Orbiter* (*JGO*), will study the two moons Ganymede and Callisto. On board of *JGO* is foreseen a laser altimeter in order to obtain a topographic map of Ganymede surface. The altimeter will be completely developed in Europe on the heritage of BepiColombo Laser Altimeter (*BELA*) which will map Mercury surface in next years. Researchers of CO.RI.S.T.A. are members of the *ESA* science team devoted to the study of this optical payload.

The task of this work is to analyze how the performance of the laser altimeter, in orbit around Ganymede, will be influenced by the scenario of the mission. For this aim it has been developed a software in *MatLab* environment which, starting from mission parameters, gives results about spacecraft orbit and laser altimeter performance. It is conceptually divided into two main blocks: the orbit propagator and the altimeter performance model.

The study is organized in five chapters.

Chapter 1 presents *EJSM* in detail: mission objectives and architecture, *JGO* orbital tour and its subsystems on board.

Chapter 2 introduces Ganymede, analyzing its orbital properties, the geology, the composition and the main features of its surface, and its atmosphere and magnetosphere.

Chapter 3 deals with the laser altimeter, illustrating how a laser works, the principle of operation and the components of a laser altimeter and its past, present and future spatial applications with a special emphasis on that designed for *JGO*.

Chapter 4 explains the structure of the developed MatLab code.

Chapter 5 presents the results of performance analysis of *JGO* laser altimeter.

CHAPTER 1

Europa Jupiter System Mission

1.1 Placing of *EJSM* in *ESA Cosmic Vision*

Cosmic Vision is the program proposed by *European Space Agency* over the period *2012-2025* in order to answer to the big questions about Universe uptaking of new clever spacecraft and the latest advanced technologies. Key themes are [1]:

- *what are conditions for planet formation and how can life was born?*
- *how does the Solar System work?*
- *what are the fundamental physical laws of the Universe?*
- *how did the Universe originate and what is it made of?*

At these questions correspond many objectives as:

- map the birth of stars and planets by investigating their formation areas and conditions for their evolution;
- search for planets around stars looking for biomarkers in their atmosphere;
- explore the surface and subsurface or solid bodies in the Solar System to find life;
- study the magnetic and plasma field environment of the Sun, the Earth, the Jovian system and outer planets;
- study Jupiter in situ, its atmosphere and internal structure and its moons;
- obtain direct information analysing samples from asteroid;
- probe the limits of general relativity, fundamental constants and physical theories;
- study the gravitational radiation background generated at the Big Bang;
- investigate the environment of black holes and other compact objects;
- investigate the physical processes that lead to Universe expansion;
- find the very first gravitationally-bound structures that were assembled in the Universe and trace the subsequent co-evolution;
- examine the accretion process of matter falling into black holes;

Because there are many goals, within the program a large number of different mission with different purposes were proposed and as of this writing they are under selection process. According to budget, they can be divided into two categories [1]:

- *M-class mission* (not beyond 300 million euros):
  - *EUCLID* mapping the geometry of dark universe
  - *SPICA* infrared space telescope for cosmology and astrophysics
  - *PLATO* next generation planet finder
  - *MARCO POLO* near Earth object sample return mission
  - *CROSS SCALE* investigating multi-scale coupling in space plasmas
- *L-class mission* (not beyond 650 million euros):
  - *XEUS / IXO* X-ray observatory for the extreme and evolving universe
  - *TANDEM / TSSM* mission to Titan and Saturn system
  - *LAPLACE / EJSM* mission to Europa and Jupiter system
  - *LISA* space interferometer to detect gravitational waves

Out of 50 concepts proposed, only three medium-class missions and three large class-missions will be selected for assessment or feasibility studies starting in *October/November 2008*. Afterwards, further working group evaluation will downselect concepts from *3* to *2* in *October 2009* while competitive definition phase for choice of the priority mission will end only in *November 2011*. Then a payload formal agreement phase and an industrial implementation will follow in *September 2012* until launch foreseen in *2017-2018*. In particular, two Outer Planet missions are being studied simultaneously: the *Europa/Jupiter System Mission (EJSM)* (figure *1.1*) and the *Titan/Saturn System Mission (TSSM)*. The selected mission will address science and technology theme that will be used to develop a comprehensive outreach programme on the exploration of the outer planets.

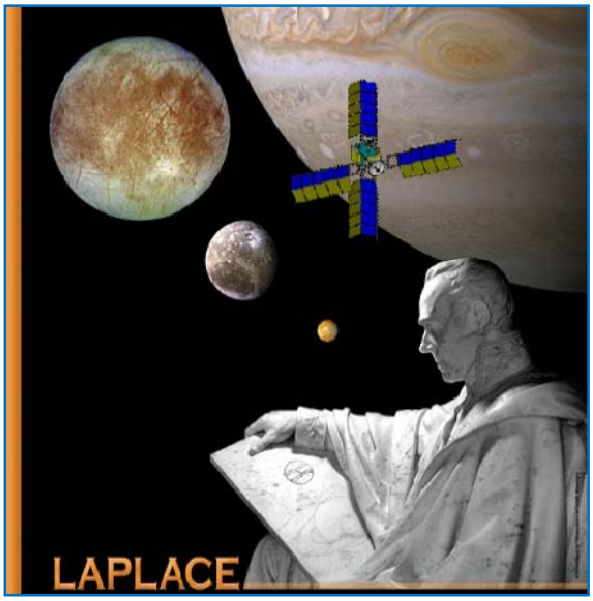

FIGURE 1.1 Artist representation for the EJSM mission [2]

This is the scenario in which *Europa Jupiter System Mission* is inserted: it is a *L-class* multi-platform mission aiming at an in-depth, quantitative study and scientific exploration of the Jovian system and its moons with special emphasis on studying Europa's habitability in a global context [3].

It is considered to unravel the many remaining mysteries of its formation from the solar nebula 4,5 milliards of years ago, its evolution to its present state, the diversity of mechanisms by which its different classes of object interact and evolve, and the condition that lead to the emergence of habitats for life among its moons [4].

It ideally follows all past missions that have studied Jovian System like Pioneer, Voyager, Ulysses, Cassini and Galileo in an epoch in which the "mini-solar system" represented by Jupiter and its moons has an even more central place in planetary exploration and in our knowledge of Universe since we prepare to celebrate the 400^{th} anniversary of Jupiter System discovery by Galileo in the distant January of *1610*.

By now, it's only a conceptual mission that, if selected among its class, will become reality, if not it will be an important idea for future exploration of Solar System.

1.2 Importance of Jupiter System and scientific objectives

As we saw above, the exploration of Jovian System and its fascinating moons, in particular Europa, is one of the priorities of Cosmic Vision program because there are many interesting facets of this world related to the key questions which we need to answer to. Indeed we can consider Jovian system as a small planetary system on its own right, made up of the mixture of gas and icy materials that built the external region of solar nebula, that displays evident signs of a long period of accretion, internal differentiation and dynamic interactions [5].

All these aspects has led to the formation of a unique satellite system in which three of the Galilean moons (Io, Europa and Ganymede) are locked in the so-called Laplace resonance [3]. The coupling implies an exchange of energy and angular momentum among themselves and with Jupiter that contributes to various degree to internal heating of the satellites with important consequences for their evolution, activity and habitability.

This satellite system is moreover embedded in a fast rotating magnetosphere and coupled to Jupiter's atmosphere by tidal interactions.

Europa surely represents the most fascinating world because it is believed to shelter an ocean between its icy crust and its silicate mantle, very geodynamically active, and so it

is one of the most promising candidate for the search for life and the main conditions for habitability in the solar system [5].

The most recent simulation studies of the dynamical evolution of the early Solar System show two important aspects: firstly they strongly suggest that the formation scenario of the Jupiter system displays many similarities with the formation of the solar system as a whole, in terms of dynamical evolution of Jovian sub-nebula; secondly Jupiter has played a key role in the formation and evolution of its sister giant planets and of the populations of small water-rich bodies, influencing the amount of water on the terrestrial planets and so their habitability. Moreover, understanding how Jupiter System works can improve our knowledge of hundreds of extra-solar gas planets discovered around other stars.

For the large variety of characteristics of this planetary system, *EJSM* is presented as a multidisciplinary mission that focuses on two of the relevant themes of the Cosmic Vision Plan:

- *What are the conditions for planet formation and the emergence of life?*
- *How does the Solar System work?*

and has one integrated overarching science goal:

- *How and to what extent did habitable worlds emerge from the formation and evolution of giant planets systems?*

To introduce mission scientific objectives, we can separate this major questions into three interrelated ones representing mission goals so that investigation can be planned around them [4].

1 – *How did the Jupiter System form?*

What have been the conditions for its formation?
How do they relate to the formation scenario of the solar system and other planetary systems?
How do they contribute to the possible emergence of life?

The history of the Jovian system can be divided into three many phases: the formation of Jupiter, the formation of its satellite system and its secular evolution to its present day state. Understanding the formation of Jupiter and its moons requires that we look at the traces of the first and second phase [5].

One of the most important open issues in the field of Solar System formation is the identification of the mechanism leading to giant planet formation.

To decipher that, it will be crucial to finally establish if Jupiter does have a solid core. *EJSM* will probe the inner structure of Jupiter up the deeper layers applying a seismological technique which will allow to answer the question of the existence of a central core but also to estimate the extension of the metallic hydrogen mantle [4].

In addition to that, the mission will permit the comparative study of regular satellites mainly in terms of their isotopic abundances, which is essential to improve our understanding of the thermodynamics of the proto-Jovian nebula. Finally, it will investigate the irregular moons to track down their origins and evolutionary features in the context of Solar System evolution of the Late Heavy Bombardment [4].
So the strategies of *EJSM* mission about this goal can be presented in three points [5] [6]:

- **Jupiter**: study of Jupiter's formation and interior (by determination of the planet's gravitational moments and seismology approach based on the oscillations of it) that can provide the whole internal density profile of Jupiter, the mass of its internal core and the amount of heavy elements;
- **Galilean satellites**: study of constrain formation scenarios and cratering history of the Galilean satellites that will provide information for dating the whole system.
- **Small bodies**: observing the irregular undifferentiated moons that will allow knowing their physical nature and testing the capture hypothesis but also looking back to the early phase of solar system evolution.

2 – *How does the Jupiter System work?*

What are the mechanisms controlling the way it works and coupling its variety of objects to make it work as a single integrated system?
How does the system contribute to the conditions for habitability?

The Jupiter system comprises a broad variety of objects, including Jupiter itself, more then *55* outer irregular small satellites, the four inner satellites (Metis, Adrastea, Amalthea and Thebe), the four large Galilean satellites Io, Europa, Ganymede and Callisto and a ring system in the inner region. All these bodies show a gravitational interaction among themselves and an electrodynamic one of variable concentration and strength with Jupiter's magnetospheric particles and field.

The complex interplay between these components is key to understand the present state of each Galilean satellite, including the presence of an ocean, its internal structure, activity and surface characteristics [4]. The tidal interaction between Jupiter and Io heats Io's interior and is responsible for its volcanic activity.

Io, Europa and Ganymede are coupled in a stable resonance which maintains their orbital period in a ratio of $1:2:4$ ad forces the orbital eccentricity of these satellites. This so-called Laplace resonance redistributes among them the energy, a possible explanation for the maintenance of a subsurface ocean at Europa. Moreover, there are hydrodynamic and radiative processes that govern the motion of different layers of Jupiter's atmosphere.

For all these reason, the Jupiter system is really unique by the diversity of its interactions. *EJSM* will perform a comprehensive study of the satellites, magnetosphere and atmosphere and their mutual coupling processes, and will investigate in detail the diversity of Galilean satellites, their physical characteristics, composition and geology of their surface.

So science objectives of *EJSM* about this theme are divisible in four group [6]:

- **Jupiter**: explore the internal and external structure and dynamics of Jupiter;
- **Ganymede**: understand the evolution of Ganymede by investigating its surface, interior and environment;
- **Magnetosphere**: study the Jovian magnetodisk and magnetosphere considering Jupiter as a fast magnetic rotator and giant particle accelerator;
- **Satellites**: investigate surface characteristics, internal structure and interactions of the moons in the Jovian system.

3 – *Is Jupiter's Europa really habitable?*

Does Europa actually harbour life?
Does it represent the "habitable zone" of the Jupiter System?

Europa, like other icy satellites, is believed to have an ocean beneath its active icy crust. But what makes Europa unique is that this ocean could be in contact with its silicate mantle where the conditions are very close to those existing on the Earth's ocean sea-floor.

For this reason, Europa is one of the best candidates for the search for life in our solar system and deserves a dedicated mission.

One of *EJSM* spacecraft will investigate in detail the conditions for the potential satellite's habitability: the presence of liquid water in a subsurface ocean, chemical and

dynamical characteristics of Europa's surface and subsurface including the presence of building block elements of life, an adequate energy source to sustain the necessary metabolic reactions, examination of possible geo-markers of some oceanic environmental properties (temperature, pH, pressure) and finally potential bi-signatures at the surface [4].

Another potential player in Europa's habitability (mainly on its surface) is surely the very hard radiaton environment due to the close position of the moon respect to Jupiter, that influences so much biological chemistry.

Therefore, we can summarised scientific goals about Europa in four points [6]:

- **Ocean**: characterize the extent of the ocean and its relation to the deeper interior;
- **Ice**: characterize the ice shell and any subsurface water, including their heterogeneity, and the nature of surface-ice-ocean exchange;
- **Chemistry**: determine global surface compositions and chemistry, especially as related to habitability;
- **Geology**: understand the formation of surface features, including sites of recent or current activity, and identify and characterize candidate sites for future in situ exploration.

1.3 Mission profile: multi-platform architecture and model payload

Due to the broad spectrum of scientific themes and of technological challenges and a large community of interested disciplines, *Europa Jupiter System Mission* will be developed with an international collaboration between *NASA*, *ESA* and *JAXA* [5]. The baseline mission configuration would include three spacecraft [3] [4] [5]:

- **Jupiter Europa Orbiter (JEO)**: developed and launched by *NASA*, *JEO* is a nadir-pointing platform optimized for global coverage of the surface, subsurface and internal structure of Europa. It would perform Jupiter system science observations once in orbit around Jupiter and later, when placed in orbit around Europa, a multi-month mapping of the moon before impacting its surface;
- **Jupiter Ganymede Orbiter (JGO)**: developed and launched by *ESA*, is a three-axis stabilized platform optimized for remote sensing observations of distant objects and in situ measurements. It's trajectory around Jupiter would include flybys of the four

Galilean moons and possibly of other Jovian moons. In the final mission phase, the spacecraft will orbit around Ganymede for studying it;

- **Jupiter Magnetospheric Orbiter (JMO**): developed and launched by *JAXA*, is a spinning platform optimized for in situ fields and particles measurements. It would monitor the Jovian magnetosphere, the moon exospheres and their interactions.

The core of *EJSM* mission is to perform a comprehensive study of the four Galilean satellites by optimizing the role of each platform. *JEO* will focus on the two "rocky" inner Galilean moons: before going into orbit around Europa, it will perform several flybys of Io. Following a similar approach, *JGO* will focus on the two "icy" outer Galilean moons: before going into Ganymede orbit, it will perform multiple flybys of Callisto.

With two orbiter around Europa and Ganymede, it will be possible an in-depth comparison of this pair of "false twin" to understand the origin of their geophysical dichotomy.

The science objectives of the mission can only be met by a combination of measurements performed with the various instruments on board the different platforms.

Because the radiation environment (mainly for the Europa Orbiter) is expected to be significantly high, implementation of mitigation strategies against radiation effects may play a fundamental role in the choice of payload accommodation options.
Anyway, under consideration are three main classes of instruments [3]:

- **Internal structure investigations**: ground-penetrating Radar, Laser altimeter, Magnetometers, radio science experiment, micro-gradiometer;
- **Remote sensing investigations**: cameras, spectro-imager, ENA low and high energy Imager, gamma/neutron spectrometer, sub-mm sounder, thermal IR imaging spectrometer, UV auroral imager, UV imaging spectrometer, V-NIR imaging spectrometer, X-ray imaging spectrometer;
- **Fields and particle investigations**: dust collector/analyzer, energetic particle detectors, ion and neutral mass spectrometer, plasma spectrometers, radio and plasma wave instrument.

1.4 *JGO*: mission analysis

Jupiter Ganymede Orbiter, as seen above, is *EJSM* spacecraft addressed to a partial observation of Jupiter and its magnetosphere but mainly to the study of its "icy" moons: Ganymede, the primary scientific target for global mapping and magnetosphere investigation, and Callisto. In this paragraph we will explain in detail mission parameters.

1.4.1 Orbital tour

The whole mission foresees several orbital phases and manoeuvres from launch to spacecraft disposal to meet all its objectives. The following scheme summarized the journey [7]:

- *Launch*
- *VEEGA transfer to Jupiter*
- *JOI insertion in orbit around Jupiter*
- *Series of Ganymede swing-bys to reduce velocity*
- *Transfer to Callisto*
- *Callisto science phase*
- *Transfer to Ganymede*
- *Ganymede science phase*

All the considerations and choices done are based on two fundamental requirements: minimize ΔV and reduce the amount of radiation that in Jupiter system is much elevate. In particular, the maximum radiation dose permitted for *JGO* is $100\ krad$ under $8\ mm$ Al shielding, value that influences the duration of the science phase and therefore of the mission itself.

Launch. At the moment the adopted solution at the moment foresees a launch into direct escape with declination of 0° by *Ariane 5* vector in *March 2018* from Kourou for a payload of about $60\ kg$ without staging and passenger spacecraft and with a complete ΔV for operations.

Total mass into escape is $3480\ kg$ (including $190\ kg$ of the adaptor and a dry mass of $1254{,}5\ kg$ keeping margins into account). It will be employed a chemical main propulsion system with a specific impulse of $325\ s$.

Finally, it has to be considered a correction of launcher dispersions of 30 m/s, while the escape velocity is 3,52 km/s [7]. Figures *1.2 a* and *b* show respectively an *Ariane 5* launcher and how the *JGO* spacecraft will be accommodated into it.

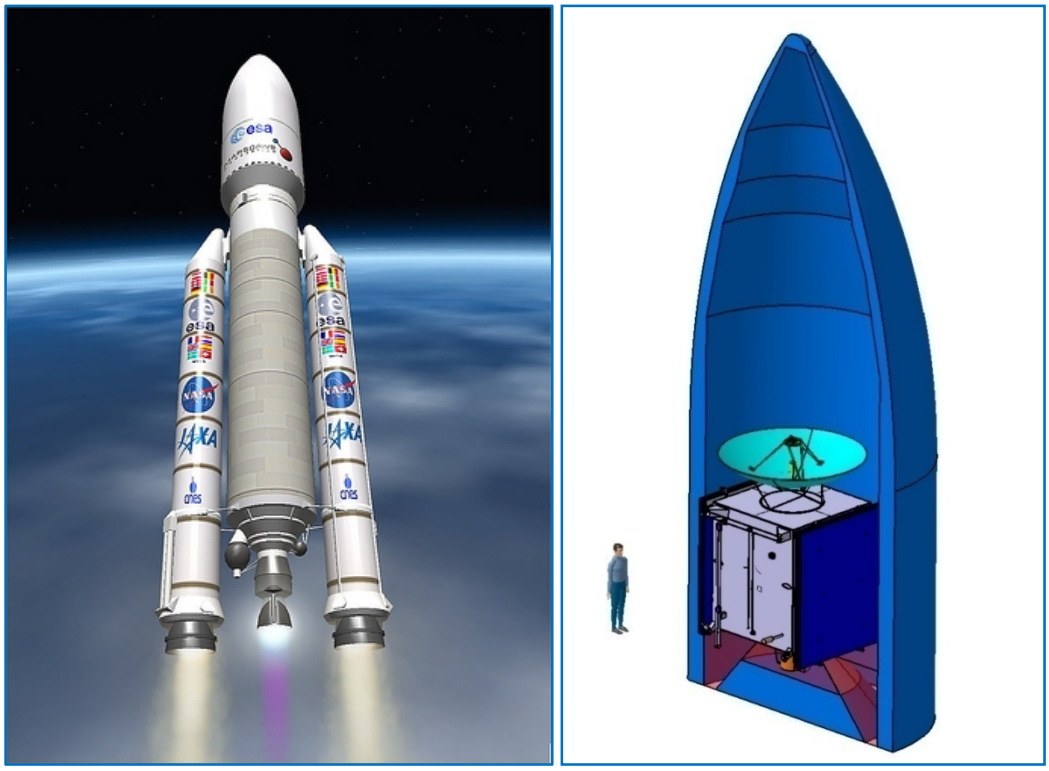

FIGURE 1.2 a) Ariane 5 vector [8] *; b) Accommodation of JGO in the launcher* [2]

Transfer to Jupiter. As for some past missions with Jupiter or Saturn as target, the most used way to get to the outer planets is based on a series of swing by, taking advantage from the gravity assistance by another celestial body (generally a planet).

This approach derives from the impossibility to reach directly the target planet, because the distance that the spacecraft has to cover is so great and then the amount of propellant requested is not sustainable. In this way, even if transfer duration is increased, there is an enormous advantage in terms of ΔV for the mission.

A gravity assist (or swing by) is a flight technique that exploits the relative velocity of the central body respect to the Sun to make spacecraft's speed greater at the end of the manoeuvre. With this technique, it is sufficient to direct the spacecraft to the reference planet with an opportune trajectory, and, according to the conditions of approaching, to modify the satellite heliocentric velocity in order to run it to the target planet that will realize the gravity assist [9].

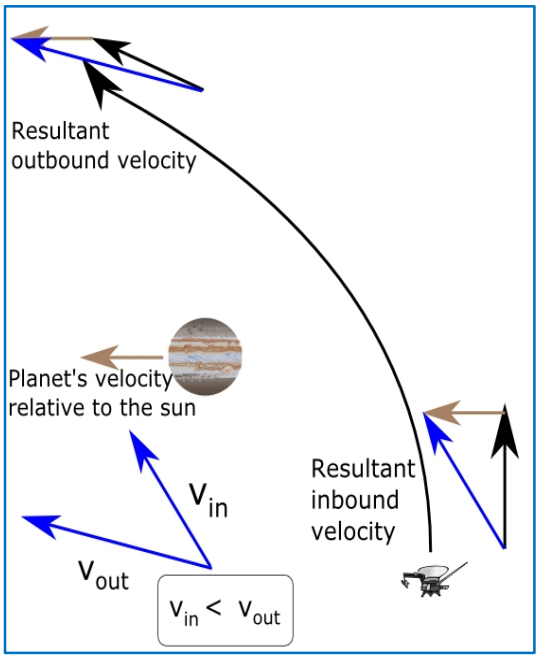

FIGURE 1.3 Gravity assist explanation [10]

The physical explanation of the manoeuvre is simple if we refer to the figure *1.3*. The spacecraft falls into the planet's influence sphere with a particular velocity V_{in} respect to the Sun (blue arrow in the picture *1.3*). The planet has its own velocity respect to the Sun (brown arrow in the picture *1.3*), therefore it is possible to know the velocity of spacecraft respect to the planet (it is sufficient to subtract the two speed obtaining the resulting speed, black arrow in figure *1.3*). Exploiting the gravitational field, trajectory of the satellite is changed and then also the direction (but not the module) of its velocity respect to the planet. In this way, because the planet speed is still the same in intensity and direction, also the spacecraft velocity V_{out} respect to the Sun is modified (in the figure *1.3* the blue vector has a bigger module and a different direction). Obviously, the trajectory and velocity desired at the exit is opportunely controlled varying the initial condition of the approach.

The interplanetary trajectory used for *JGO* is indicated with the acronym *VEEGA*, which is for Venus-Earth-Earth Gravity Assist because it foresees three successive swing-bys with a declination of zero degrees (all the maneuvers have place in the ecliptic plane) according to the following mission planning [7]:

- *Venus Swing-by (V1)* on *13 April 2019*, altitude 4992 *km*
- *Earth Swing-by 1 (E1)* on *6 May 2020*, altitude 7148 *km*
- *Earth Swing-by 2 (E2)* on *6 May 2022*, altitude 3985 *km*

The arrival is expected on *September/October 2024* after a flight of about 6,6 years. All the interplanetary transfer is represented above.

A representation of *VEEGA* is shown in figure *1.4*.

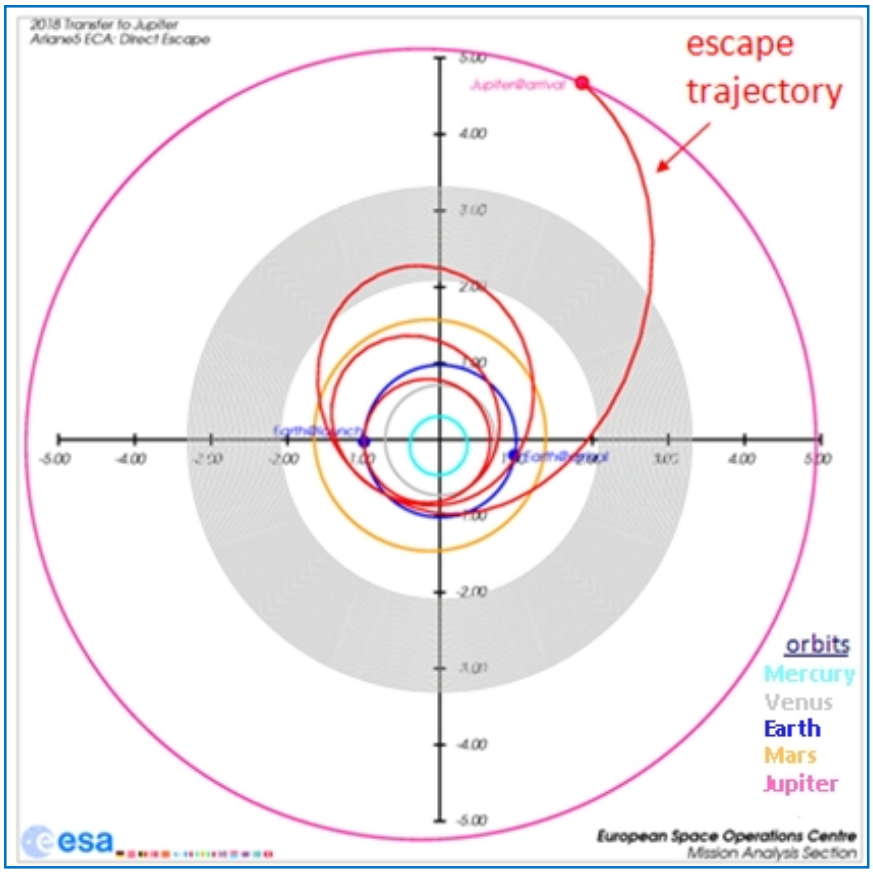

FIGURE 1.4 VEEGA Interplanetary transfer from Earth to Jupiter [2]

Insertion in orbit around Jupiter. The spacecraft will arrive in Jupiter system with an infinity velocity of 5,94 km/s and a declination respect to planet's equator of $-4.2°$.

Before starting its Jovian orbit, the mission foresees a gravity assist with Ganymede (*GGA*) to reduce the capture cost at an altitude of 300 km that will take the velocity to a value of 7,95 km/s. Then it begins the so-called Jupiter Orbit Insertion (*JOI*), a manoeuvre characterized by a $\Delta V = 962\, m/s$ that will put the spacecraft into a highly elliptical $25:1$ resonant with Ganymede orbit around the planet with a pericenter of 12,5 R_j and an apocenter altitude of 244 R_j. After a perijove raising manoeuvre close to the apocenter with a $\Delta V = 102\, m/s$, the infinity velocity will be passed to 6 km/s through a second gravity assist with Ganymede (*GGA2*).

The whole phase should start on *12 October 2024*, has a duration of 179 days and iy will be characterized by a radiation dose of 3 $krad$.

A representation of *GGA2* is shown in figures *1.5* and *1.6*, followed by an enlargement in the proximity of where gravity assists have place.

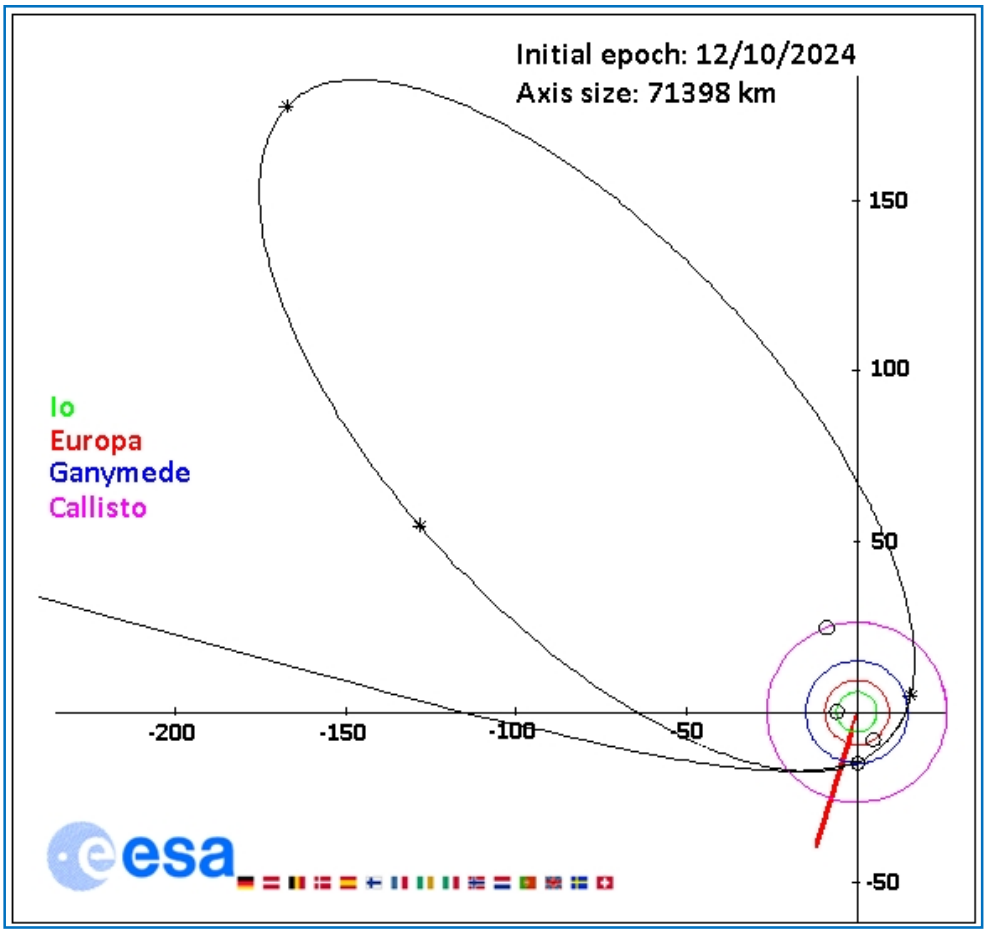

FIGURE 1.5 From Jupiter arrival to GGA2 [7]

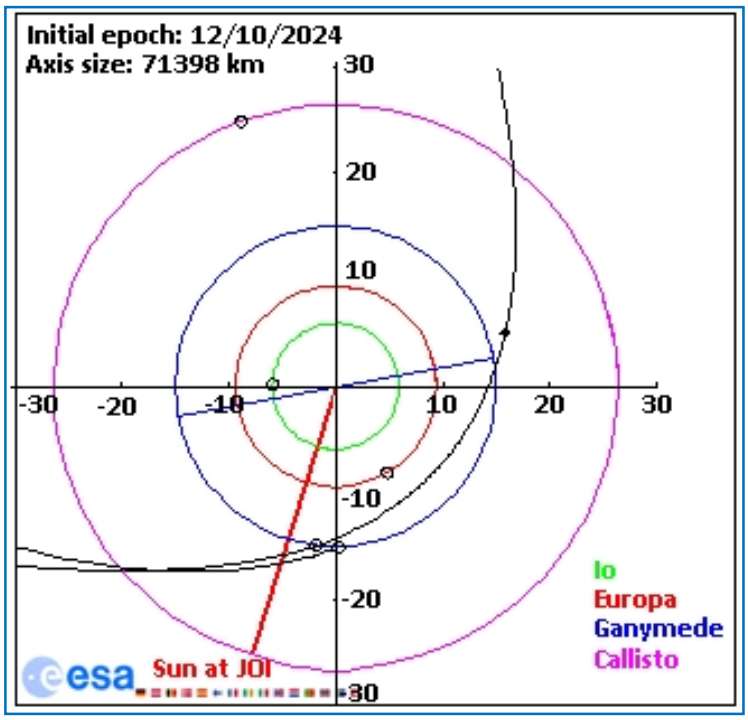

FIGURE 1.6 From Jupiter arrival to GGA2 (focus) [7]

Series of Ganymede swing-bys. Three further gravity assists with Ganymede are used for three aims (related to the Jovian orbit):

- reduce the apocenter (the orbital period)
- reduce the inclination
- reduce the infinity velocity (respect to Ganymede)

They will be in resonance with Ganymede's orbital period and take place in sequence, with ratios of 7: 1, 4: 1 and 3: 1.

At the end of this manoeuvres, we have a final perijove and apojove respectively of 12,3 R_j and 50 R_j and a infinity velocity respect to Ganymede of 5 km/s.

This phase from *GGA2* to *GGA5* (shown in figure *1.7*) should begin on *9 April 2025* lasting 100 days and give a contribute for the total radiation of 6 $krad$.
This Deep Space Manoeuvre (*DSM*) has a ΔV of 140 m/s.

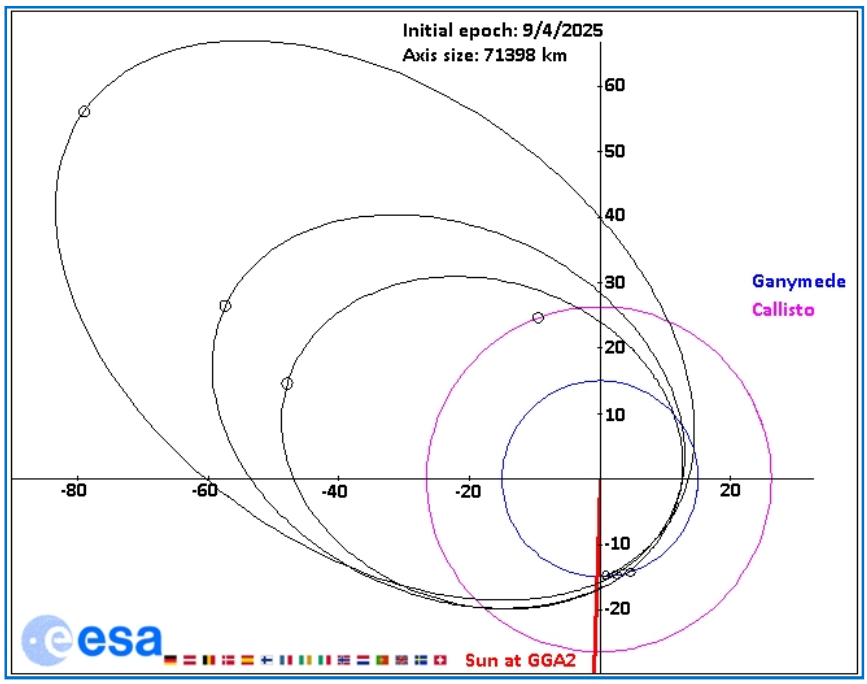

FIGURE 1.7 From GGA2 to GGA5 [7]

Transfer to Callisto. In order to reach Callisto with a proper low velocity and to start the science phase around it, other orbital corrections will be necessary, always exploiting gravitational assistance of Callisto itself and Ganymede, according to the sequence *GCGC (Ganymede-Callisto-Ganymede-Callisto)* described in figure *1.8*.

This part of orbital transfer should begin on *19 July 2025* and develop itself for 36 days: at the end of this transfer, the spacecraft will have a infinity velocity respect to

Callisto of 2,07 km/s. Finally, $DSM = 26\,m/s$ while the radiation dose is equal to 10 $krad$.

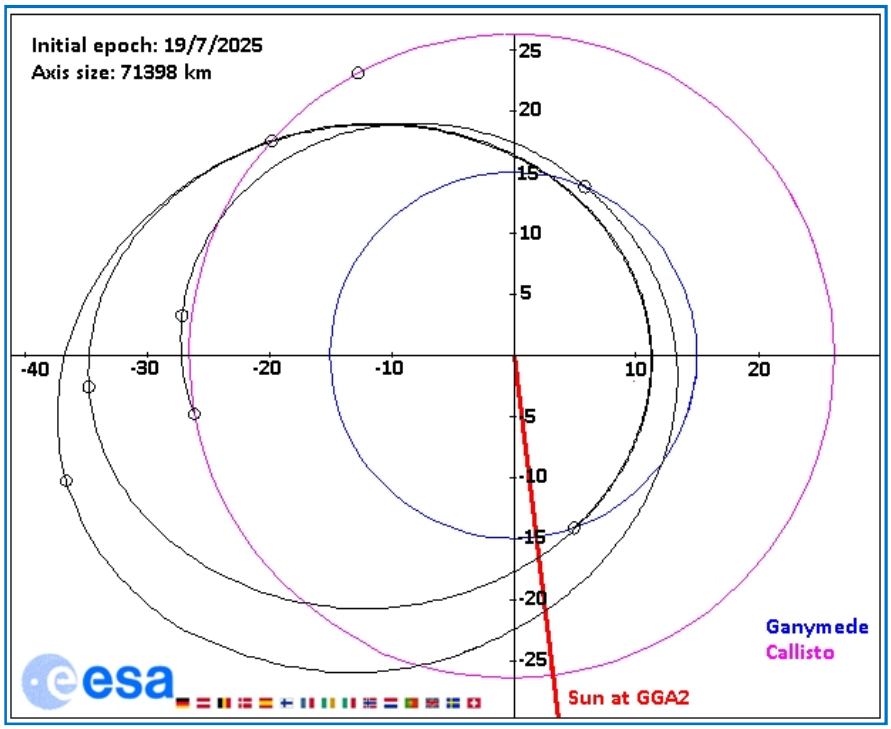

FIGURE 1.8 From GGA5 to Callisto [7]

Callisto science phase. The strategy adopted to investigate Callisto is not based on inserting into a close orbit around it, but foresees 19 fly-by around the moon.

Differently from a gravity-assist, a fly-by is a flight technique consisting of a simple "flying over" the celestial body, without falling, even for a short time, into an orbit around it (the same happens for a swing-by). It has to be noted that gravity assist technique needs a fly-by, but it is possible to have a fly-by without gravity assist.

To guarantee full coverage, the altitude for these passages has to be 200 km; in particular, for a best lateral coverage of the intermediate longitudes between the two primary ones and frequent passages we have to use 2: 3 resonances with the moon's orbital period.

During all this phase of pseudo-orbit, which has a duration of 383 days, the infinity velocity remains very close to 2,05 km/s. *DSM* and radiation dose are in order 152 m/s and 30 $krad$.

Transfer to Ganymede. Before starting the final phase of the mission for studying Ganymede, the spacecraft has to reach the moon with a low relative velocity in order to insert into the orbit around it.

For this purpose a sequence *CGG (Callisto-Ganymede-Ganymede)* gravity assist will be performed in order to reduce the infinity velocity respect to Ganymede and to reach a value of 936 m/s. All these manoeuvres should begin on *13 September 2026* and they will end after 76 days. The total *DSM* is 130 m/s while the radiation dose 3 $krad$. Figure *1.9* show the orbits of this phase.

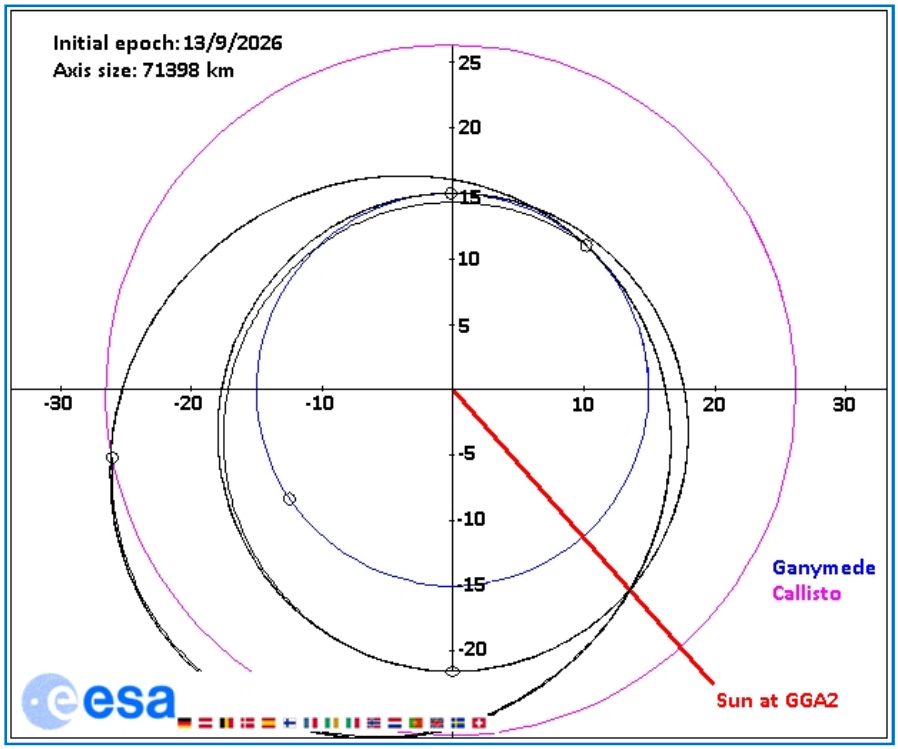

FIGURE 1.9 From Callisto science phase to Ganymede [7]

Ganymede science phase. This phase is the most important objective of the *JGO* mission: to study in detail Ganymede moon. This part of *EJSM* is divided into two sub-phases:

- *Elliptical orbit.* A Ganymede Orbit Insertion manoeuvre (*GOI*) with a $\Delta V \sim 610\ m/s$ will insert the spacecraft into a $200\ x\ 6000\ km$ altitude near-polar orbit ($i = 86°$) with initial argument of pericenter equal to 141.8° (to maximize lifetime), optimized for a good investigation of the Ganymede magnetosphere (figure *1.10*).

  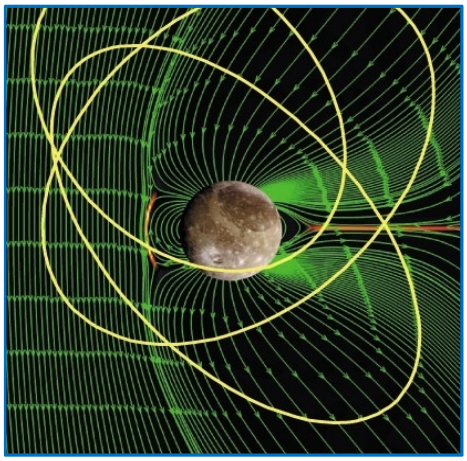

  FIGURE 1.10 Representation of elliptical orbit for magnetospheric studies [11]

  Following a free evolution of the orbit under the third body effect, during a lifetime of 80 days the pericenter increases while the apocenter decreases, showing a tendency to circularization. Also the argument of pericenter becomes greater, guaranteeing a good coverage of the equatorial latitude. Inclination and longitude of the ascending node remains almost constant, because the orbit is quasi-polar.

  Maximum eclipse duration is just 0,8 hour. A good global coverage is achieved, with most points on the surface visited by the orbiter more than once. At day 78 the velocity at the pericenter is $200\ m/s$ and a circularization maneuver of $345\ m/s$ can be performed.

- *Circular Orbit.* Figure *1.11* shows the circular $200\ km$ near-polar orbit (inclination close to 87.5°): in this phase starts the acquisition of scientific data for Ganymede. The low and constant altitude ($200\ km$) allows a global survey of the moon in order to map its surface: a good coverage will be achieved in less than 150 days. Eccentricity remains quasi-stable, as for inclination and ascending node. The lifetime of this orbit should be about 200 days with a maximum eclipse period of about 0,92 hour, but, in

  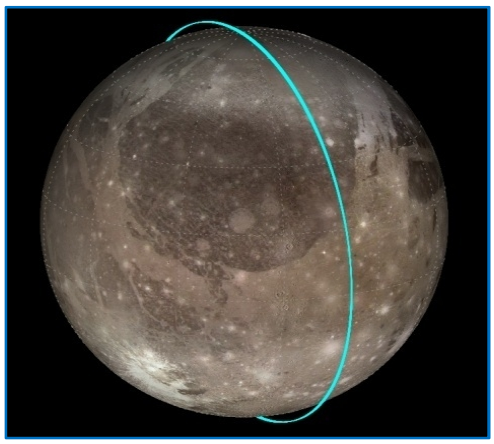

  FIGURE 1.11 Polar 200 km altitude orbit around Ganymede [11]

order to satisfy the maximum radiation dose assumption ($100\ krad$), it has to be estimated that the mission duration has to be set to 105 days. There is also the possibility to re-initialize the circular orbit with a cost of few m/s after approximately five months.

The end of the nominal mission is foreseen for *September 2027* after a period of about 9,5 years.

As mentioned above, the main constraint of this phase is the radiation dose. It is a function only of the duration of Ganymede science phase and does not depend on the orbit around the moon. If this constraint is made less stringent, mission duration (in particular the circular science phase around Ganymede) can be extended or it could be considered the possibility of flying above Europa or/and Io.

Finally, it has to be noted that the mission plan presents a phase of studying both for Ganymede and Callisto, but only for the first of the two moons can be achieved an insertion into orbit, while for the second just a pseudo-orbit solution through several fly-bys is feasible. In the table *1.1*, are summarized the main parameters characterizing the different orbital phases, while the figure *1.12* represents all the orbital tour.

Orbital phases	ΔV [m/s]	swing-bys	TOF [days]	eclipse [h]	Rad. [krad]	Nav. ΔV [m/s]
Interplanetary transfer	0	3	2400	0	?	165
insertion in Jovian orbit	1064	2	179	0	3	10
series of Ganymede swing-bys	140	3	100	1,7	6	30
transfer to Callisto	26	4	36	3,2	10	30
Callisto science phase	152	19	383	4,5	30	180
transfer to Ganymede	130	3	76	4,2	3	20
Ganymede science phase: elliptical orbit	610	0	80	3,8	21,5	5
Ganymede science phase: circular orbit	345	0	105/200	3,8	26,5/?	5
total	2437	34	9,2/9,4 years	21,2	100/?	445

TABLE 1.1 Main parameters for the orbital phases of JGO [2]

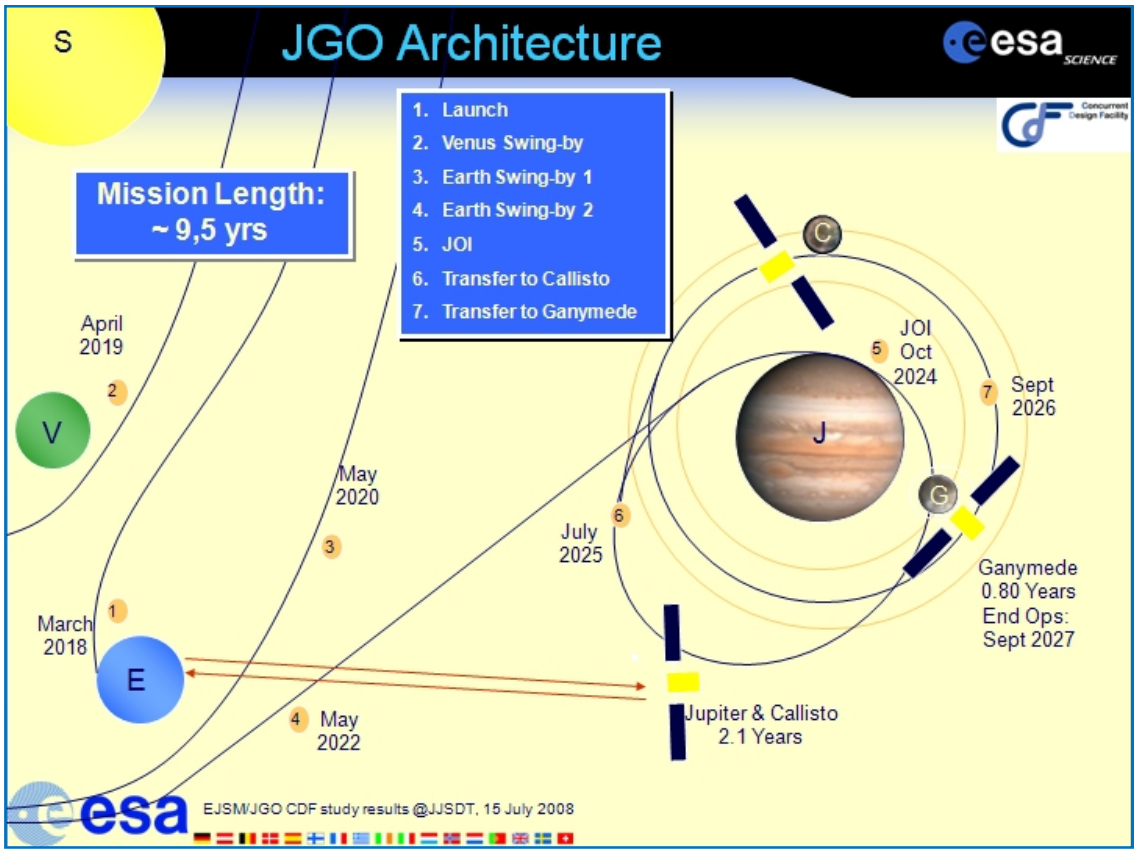

FIGURE 1.12 Orbital tour of JGO spacecraft [2]

1.4.2 Spacecraft subsystems

Structures and configurations. Figure *1.13* shows the structural body of the spacecraft and its main components.

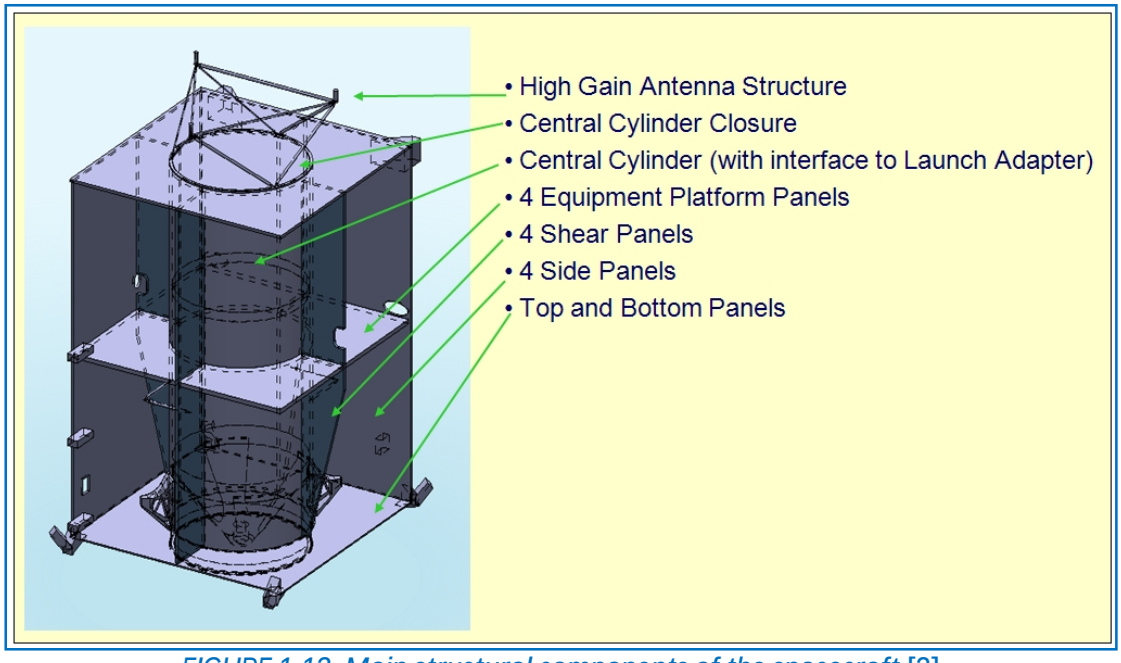

FIGURE 1.13 Main structural components of the spacecraft [2]

It is formed by two parallelepipeds, one resting on the other, separated by four equipment platform panels, with a central cylinder having an interface with launch adapter and a closure at the top. The whole body has as external faces side, top and bottom panels and is completed by an high gain antenna structure and a series of shear panels within the cylinder.

For *JGO* and for all the *EJSM* one of the most important design requirements is the shielding analysis due to the hostile radiation environment. Considering that *TID (Total Ionizing Dose)* after 260 days in orbit around Ganymede is $77\ krad$ while the maximum permissible amount of radiation has been set to $100\ krad$, mitigation strategies are necessary.

All the boxes (but not spacecraft primary structure) are surrounded with a $8\ mm$ shielding layer of aluminum, also if a composite shielding material is at the moment under study). Just to give an idea, for a payload mass of about $60\ kg$ and other spacecraft electronics, it is needed to allocate a shielding mass of $80\ kg$.
The figure *1.14* illustrates the internal appearance of the satellite in details.

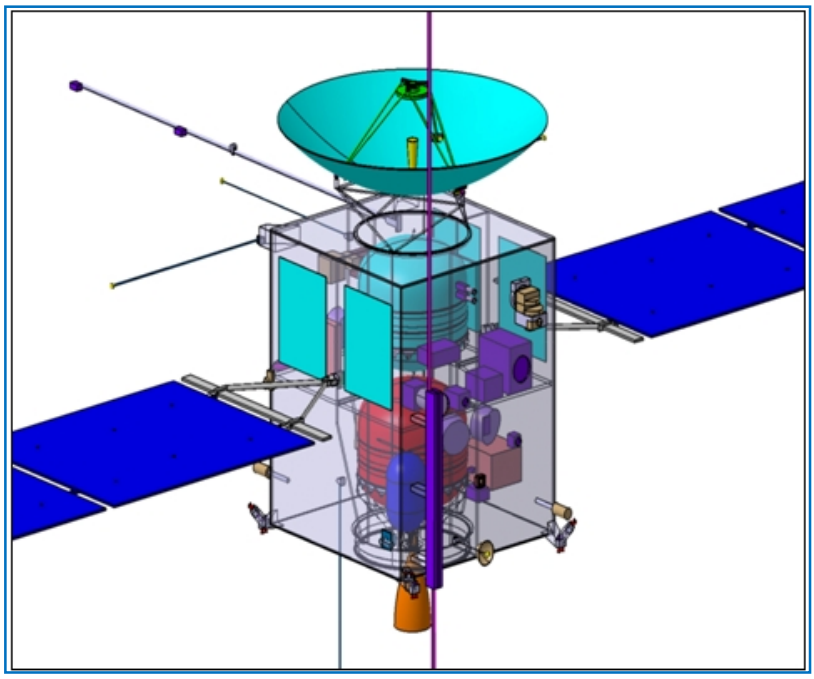

FIGURE 1.14 Internal view of the spacecraft [2]

Propulsion. All the propulsion subsystem is made up of only European components with a very high Technology Readiness Level (*TRL*) for all of them. The solution adopted foresees a bi-propellant *MON-MMH* system, with mixed oxides of Nitrogen as oxidizer

and monomethylhydrazine as comburent, that has to achieved the speed of about 3030,35 m/s and which is characterized by a mass of about 160 kg.

A European Apogee Motor (*EAM*) 500 *N* represents the main engine with a specific impulse of 325 *s*, while eight couples of *AOCS* 10 *N* thrusters allow to control and change spacecraft attitude.

The propulsion subsystem is completed by two *OST-22/X* tanks of 1108 liters and two pressurant tanks for helium. In figure *1.15*, we can see how engine and tanks are disposed within the spacecraft.

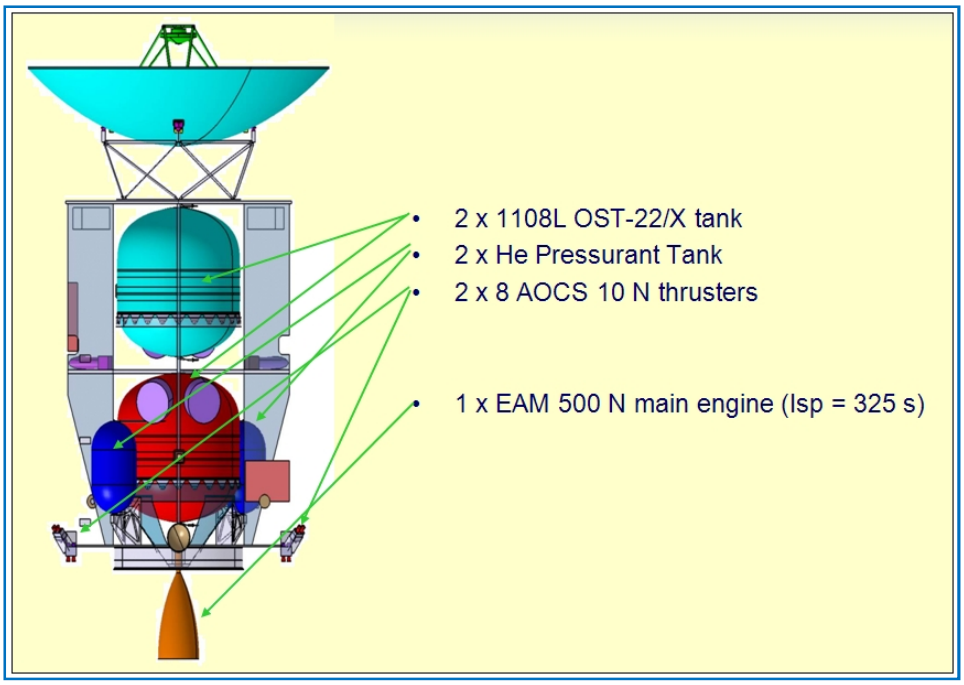

FIGURE 1.15 Main components of propulsion subsystem [2]

Payload. On the Jupiter Ganymede Orbiter the payload shall perform the following observations [2]:

- during the tour in the Jovian system including flybys of the irregular moons
- at Jupiter
- at Ganymede and Callisto

As of this writing it has been foreseen a payload total weight of 67,6 kg that with a margin of 20% becomes 80,4 kg.

With the table *1.2*, are listed all the forecasted instruments with a particular attention on their mass and power.

name	acronym	mass (kg)	size (cm)	power (W)	TRL
JGO Radio Science Trasponder	JRST	3	10 x 20 x 15	10,5	6
Ultra Stable Oscillator	USO		15.2 x 9.0 x 13.0		9
Magnetometrs	MAG	0,3	11 x 7 x 5 sensors 5 x 7 x 3 electronic	0,6	6
Micro Laser Altimeter	MLA	3	10 x 5 x 5	25	3
Sub-Surface Radar	SSR	12	37 x 25 x 13	20	5
Wide-Angle Camera	WAC	7,5		16	6 - 8
Medium Resolution Camera	MRC				6 - 8
Visible/InfraRed Hyperspectral Imaging Spectrometer	VIRHIS	17	50 x 40 x 30 optical head	20	5
UV Imaging Spectrometer	UVIS	6,5	30 x 30 x 20	3	4
Narrow Angle Camera	NAC	8		15	5
Langmuir Probe - plasma wave Instrument	LP-PWI	2,6		2	8
plasma package	PLP	7,7		15	6
total		67,6		127,1	

TABLE 1.2 Instruments on board the JGO [2] [12]

The figure *1.16* and *1.17* show respectively the external and the internal accommodation for all the instruments.

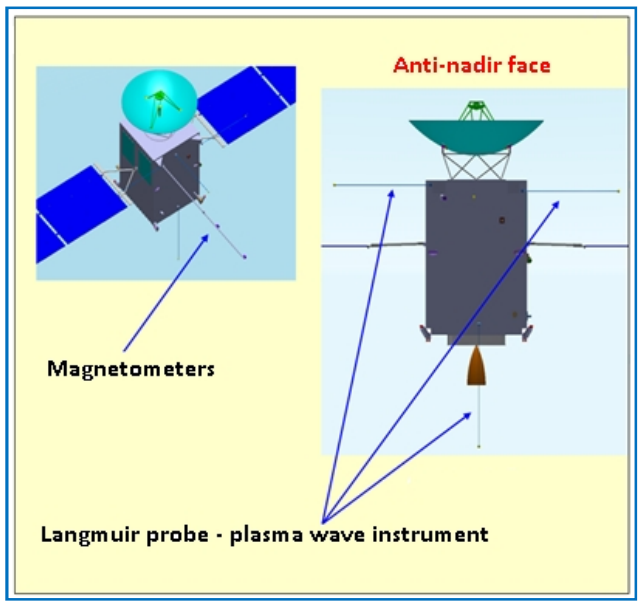

FIGURE 1.16 External payload accommodation [2]

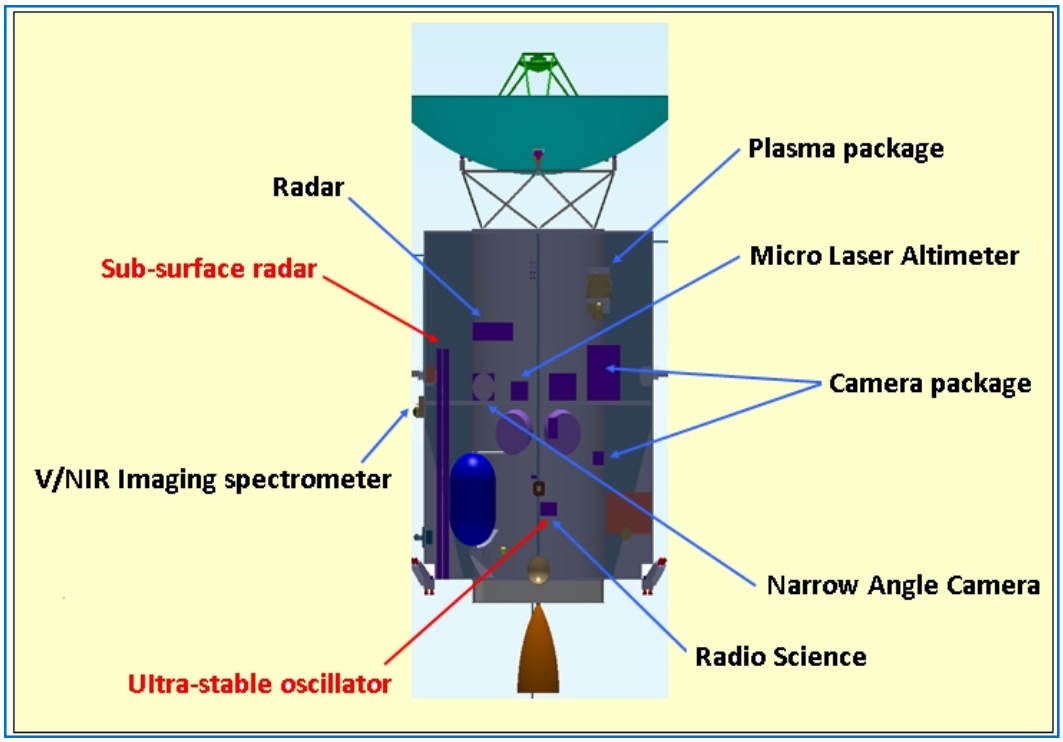

FIGURE 1.17 Internal payload accommodation [2]

Thermal. The solution adopted for thermal control foresees a passive subsystem that works without consumption of electrical energy. The way to regulate temperature is not the same for all the components, so we have different parts that make up the entire subsystem:

- optical solar reflector radiative surface of $1{,}26\,m^2$ (preferred to paints because of degradation issues due to radiation);
- louvers on radiators to adapt emissivity as function of power dissipated and minimize heating power demanding;
- high temperature *MLI (Multi-Layers Insulator)* on the spacecraft external surface (optimized for the hot environment next to Venus);
- *MLI* on tanks, thruster boxes and pipe lines;
- heaters/sensors for propulsion equipment temperature regulation;
- black paint on internal surfaces to minimize thermal gradients.

AOCS (*Attitude and Orbit Control Subsystem*). *JGO* is a three-axis stabilized spacecraft, so its attitude determination and control subsystem include the following elements:

- four reaction wheels;
- two star trackers;
- one internal measurement unit;
- two sun sensors;
- one navigation camera for critical maneuvers;
- six thrusters for correction maneuvers and wheels offloading;

Pointing requirements are respectively for *HGA (High Gain Antenna)* pointing, sun acquisition and science $\sim 0{,}01°$, $\sim 0{,}1°$ and $\sim 10"$, while pointing stability is $0{,}3"/s$ over $0{,}5\ s$.

Power. To dimension the Electrical Power Subsystem (*EPS*), is considered a series of requirements and assumptions:

- degradation effects based on $3 \cdot 10^{15}$ $1\ MeV$ electrons during the mission;
- Sun illumination of $51\ W/m^2$ at Jupiter orbit and of $2614\ W/m^2$ next to Venus;
- $-108°\ C$ as solar array temperature at Jupiter;
- deployable and rotating solar arrays;
- assessment of science operations and Communication to reduce the needed power;
- no solar concentrators considered;
- eclipse science mode as battery sizing case ($270\ min$).

Baseline design foresees the following components, correlated by its own characterizes:

- *Battery Regulated Bus*: $28\ V$;
- *Deployable solar array*: Ga-As *LILT (Low Intensity Low Temperature)* solar cells with an efficiency at BOL *(Beginning Of Life)* of 28% and a power in the same condition of $539\ W$ for a total surface of $51{,}1\ m^2$. The configuration is based on that of Rosetta solar array with four panels per wing instead of five and mechanisms exclusive. The total mass without margin is $252\ kg$;

- *Li-Ion Battery*: with a global capacity of $120\ Ah$, it is structured in an electrical scheme made up of 7 elements in series and 80 of this series in parallel. Not considering margin, its mass is $26{,}5\ kg$;
- *Power Control and Distribution Unit*: a low ripple buck converter and a *PPT (Peak Power Tracking)* for solar array regulation are forecasted for a total mass of $12{,}3\ kg$ (always without margin).

It is much important having an optimum pointing of the solar panels to the Sun during all operation modes. This requires that the instrument boresight is continuously rotated around the nadir axis in Ganymede circular orbit.

Communications. To cover a mean distance of $5\ AU$ (with a maximum of $6{,}1\ AU$) for Earth-spacecraft communication, will be used two omni-directional *LGAs (Low Gain Antennas)*, two *MGAs (Medium Gain Antennas)* and a $2{,}8\ m$ *HGA (High Gain Antenna)*.

Data rate is in the range $40 - 66\ kbps$, while as bands adopted we have the *X* for Telecommand and Telemetry and the *X* and *Ka* for science downlink and uplink and radio science.

Compose the terrestrial segment several *ESA* controlled *Ground Stations*, using the *ESA* ground station network called *ESTRACK*. Are foreseen three *X* band stations for Launch and Early Orbit Phase (*LEOP*) in Kourou, Cebreros and New Norcia, while just the Cebreros one, whose antennas have a *G/T* and an elevation respectively of $50\ dB$ and $10°$ for *X* band and of $55\ dB$ and $20°$ for *Ka* band, for cruise and observation phase at Jupiter, supported by New Norcia for critical phases as fly-bys and orbit insertions. *NASA* and *JPL (Jet Propulsion Laboratory)* provide emergency support.

Considering communication windows of eight hours, there are some advantages from this configuration: firstly range of angles for *HGA* pointing are too large so no pointing mechanism is necessary for this antenna (an optimum pointing of *HGA* to the Earth is always guaranteed); secondly no pointing of instruments will be done during communication periods.

Data handling system. The design for the subsystem responsible of data treatment on board is based on highly integrated control and data system studied for Bepi-Colombo mission and foresees an integrated processor with telecommand and telemetry modules plus redundancies, an integrated mass memory board and controller (a single flash-based Solid State Mass Memory *SSMM* board of 256 $Gbits$ fulfills the 10 days requirement) and an integrated payload computer board plus redundancy.

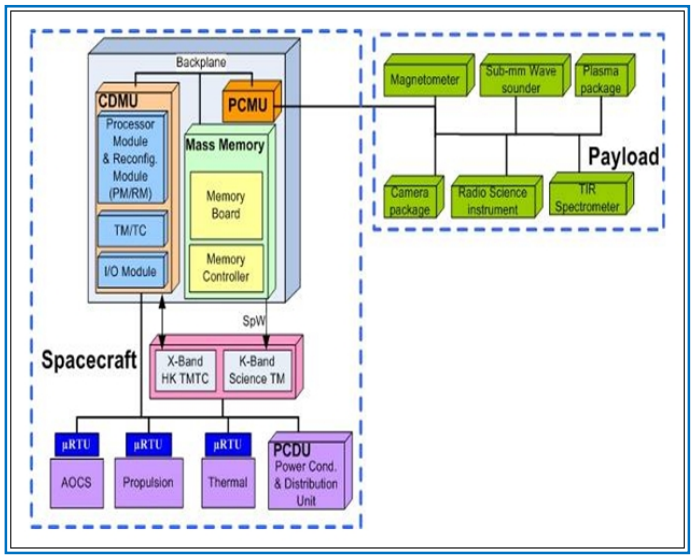

FIGURE 1.18 Representation of on board data handling subsystem [2]

The illustration *1.18* is a schematic representation of the subsystem in its totality (not all the instruments are reported).

Launch Options. About launch adaptors, for *EJSM* two kind of solutions are under investigation, the internal one with *Sylda* system and the external one based on *Speltra* adaptor (figure *1.19*). In both cases no change in configuration is required.

Indeed, if the launcher have to house also a passenger spacecraft (spacecraft launched atop one-another), two ways for separation are possible after a launch together: the two platform can be separated or after escape without any maneuvers or before the *JOI* but with some maneuvers. In these last cases spacecraft configuration has to be adapted (the second is the most difficult situation for adapting).

Considering that at launch, for a payload of 67,6 kg, dry mass is 1254,52 kg and the total mass is 3480 kg (including margin and adapter), we can compute launch margin that is equal to 590 kg (0,14%), knowing that the maximum mass at launch is 4070 kg.

If a passenger spacecraft is present, its entire mass has to be not greater then ~369 kg, including tailored interface to *JGO* and *JGO* structural renforcement.

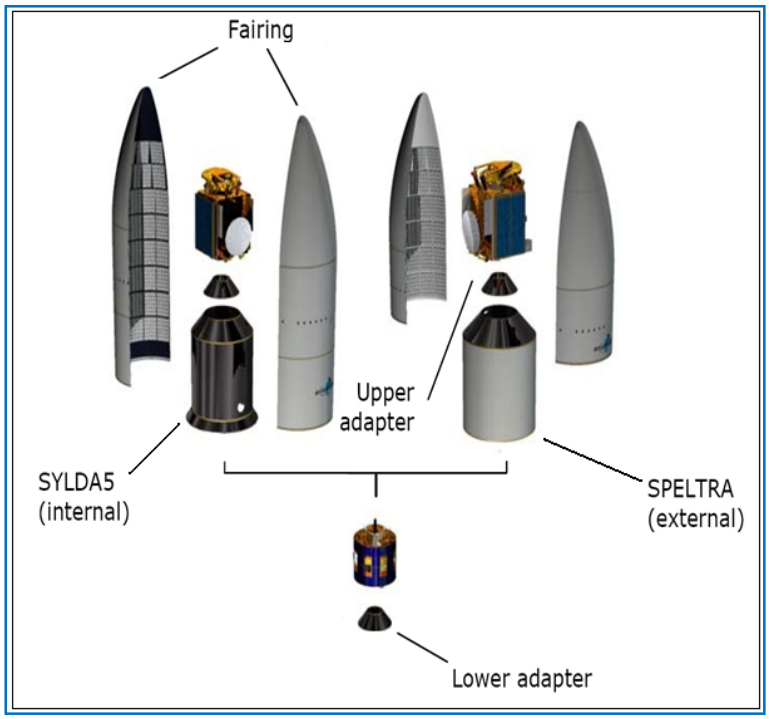

FIGURE 1.19 Comparing between Sylda and Speltra system [2]

To have a general vision of different contributes to the spacecraft dry mass by each subsystem , it is reported the table *1.3*:

dry mass contributions	without margin	margin		total
	kg	%	kg	kg
structure	118,87	19,03	22,62	141,49
thermal control	28,42	20,00	5,68	34,10
mechanisms	33,65	10,00	3,36	37,01
communications	38,63	5,60	2,16	40,79
data handling	13,30	10,00	1,33	14,63
AOCS	48,30	5,00	2,42	50,72
propulsion	160,05	5,47	8,75	168,80
power	290,84	10,00	29,08	319,92
harness	65,82	20,00	13,16	78,98
instruments (payload)	67,60	16,83	11,38	78,98
radiative shielding	80,00	0,00	0,00	80,00
total dry (excl. adapter)	945,47			1045,43
system margin (excl. adapter)		20,00		209,09
total dry with margin (excl. adapter)				1254,52

TABLE 1.3 Contributes to the spacecraft dry mass by each subsystem [2]

CHAPTER 2

Ganymede

2.1 Overview

Ganymede is a moon of Jupiter, the largest not only among the 63 natural satellites of the planet but also among the whole Solar System's satellites. With a radius of 2631 km, over $1/3$ than Earth's and greater than Mercury's and Pluto's, it is planet-sized world and belongs with Io, Europa and Callisto to the group of the Galilean moons of Jupiter.

Completing an orbit in a little more than seven days, Ganymede is the seventh satellite and the third among Galilean moons from Jupiter. Its discovery, like all Galilean moons, is dated *January 1610* and credited to the Italian scientist *Galileo Galilei*, which identified Ganymede like *Jupiter III* (third moon from Jupiter); the name adopted today was later suggested by astronomer *Simon Marius* and reminds to the mythological cupbearer of the Greek gods and Zeus's beloved.

Ganymede's geology, geophysics, surface composition and evolution are rather complex to analyze. The satellite's density of 1,936 g/cm^3 implies a bulk composition that is about 60% rock and 40% water, which is mainly in the form of ice and whose mass fraction is between $46 - 50\%$ (generally rocky materials have a density over 50% more than icy ones).

Because of the distance of Jupiter System from the Sun (over 5 AU), ice is stable under direct solar illumination thus water can stand only in a solid state. Some additional volatile ices such as ammonia may also be present. The abundance of ice, strongly reflecting incident radiation from the sun, is the main reason of the relatively high value of Ganymede's geometric albedo equal to 0,43.

The exact composition of Ganymede's rock is not known, but is probably close to the composition of *L/LL* type ordinary chondrites, which are characterized by less total iron, less metallic iron and more iron oxide than *H* chondrites. Gravity data from the *Galileo* spacecraft indicate also that Ganymede is strongly differentiated, maybe with an interior

made up of a mixture of rocky materials, probably concentrated in a central core, and an icy external mantle.

Ganymede is the only moon in the Solar System known to generate an internal magnetic field, implying a hot convecting core of liquid iron; the thin magnetosphere is buried within Jupiter's much larger magnetic field and connected to it through open field lines. Moreover, there are indications of an induced field component suggesting a deep internal ocean of briny water.

The satellite has a thin oxygen atmosphere that includes O, O_2 and possibly O_3 (ozone) with atomic hydrogen as a minor constituent.

According to its dimension, Ganymede stands in a band of transition between geological active planets like Earth, Venus and Mars and the smaller bodies, getting cold too rapidly to permit a geological activity such volcanism and tectonism with a "rejuvenation" of surface, deformation and fracture of external crust.

Images of Ganymede's surface show craters, furrows, dark and bright areas greatly differentiated and structures characteristic only of it. In particular, its surface consists of about 35% ancient dark terrain, remaining of an ancient crust which is relatively heavily cratered, and about 65% bright grooved terrain, which is more recent and heavily tectonized, both signs of a tumultuous past and of a geological activity.

Spectral study have shown that the bright terrain is ice-rich, while dark terrain contains a greater fraction of rocky material. Though its lithosphere is primarily water ice, the geology of bright terrain finds analogy with terrestrial rift zones. Impact features of different forms and ages are present mainly on dark terrain but also on the bright ones and sometimes can overlay or be crosscut by the groove systems. No significant relieves have been found on the surface with a maximum altitude estimated to be less than $1000\ m$.

Ganymede is straddled in distance from Jupiter by its siblings Europa and Callisto, and in some respects is transitional between the two. Indeed, Ganymede dark terrain is reminiscent of Callisto's desolate landscape, while its bright terrain evokes Europa's bizarrely tectonized surface. Anyway, Ganymede is arguably the solar system's "type example" icy satellite, with terrains showing analogy which many other satellites; therefore its understanding can be useful to a best comprehension of the other Galilean moons and in general of the external planets' several moons.

The figure *2.1* shows Ganymede in a true-colour image taken by the *Galileo* probe while table *2.1* summarizes all the interesting physical and orbital parameters of this moon.

FIGURE 2.1 Ganymede photographed by Galileo spacecraft (true colors) [13]

PARAMETER	VALUE	UNIT OF MEASUREMENT	SOURCE
PHYSICAL			
mass *m*	$1.48167 \pm 0.00020 * 10^{23}$	kg	[14]
mean radius *R*	2631.2 ± 1.7	km	[17]
volume *V*	$7.6 * 10^{10}$	km^3	[13]
surface *A*	$87 * 10^{6}$	km^2	[13]
mean density ρ	1.936 ± 0.022	g/cm^3	[14]
pressure on surface	$0.2 – 2.5 * 10^{-5}$	µBar	[13]
minimum-medium-maximum surface temperature	70 – 110 - 152	K	[13]
geometric albedo (global)	0.43 ± 0.02	–	[17]
apparent magnitude	4.61 ± 0.03	–	[17]
MAGNETIC			
Intrinsic equatorial magnetic field	719	nT	[16]
intrinsic polar magnetic field	1438	nT	[16]
Jovian environment magnetic field	120	nT	[16]
magnetic dipole momentum	$1.3 * 10^{13}$	Tm^3	[13]

PARAMETER	VALUE	UNIT OF MEASUREMENT	SOURCE
GRAVITATIONAL			
planetocentric constant μ	9887.834 ± 0.017	km^3/s^2	[17]
gravity on surface	0.145	g_{earth}	[18]
escape velocity v_{esc}	2.741	km/s	[18]
dimensionless polar momentum C/mR^2	0.3105 ± 0.0028	–	[14]
quadripole momentum J_2	$126.9 \pm 6.0 * 10^{-6}$	–	[14]
settorial harmonica C_{22}	$38.184 \pm 0.870 * 10^{-6}$	–	[14]
sphere of influence	24348.5613	km	–
ORBITAL			
semi-major axis a	1070400	km	[15]
perijove	1069200	km	[13]
apojove	1071600	km	[13]
mean distance from the Sun	5.203	AU	[18]
eccentricity e	0.0013	–	[15]
eccentricity range	0.0009 – 0.0022	–	[13]
inclination i	0.177	°	[15]
inclination range	0.05 – 0.32	°	[13]
argument of periapsis ω	192.417	°	[15]
longitude of the ascending node Ω	63.552	°	[15]
mean anomaly M	317.540	°	[15]
inclination of rotational axis respect to orbital plane	0 – 0.33	°	[13]
rotational period P_{rot}	7.154553	day	[18]
revolution period P_{rev}	7.154553	day	[18]
longitude rate n	50.3176072	°/day	[15]
mean orbital velocity	10.880	km/s	[18]
argument of periapsis precession period P_ω	63.549	year	[15]
longitude of the ascending node precession period P_Ω	132.654	year	[15]

TABLE 2.1 Ganymede's physical, magnetic, gravitational and orbital parameters

2.2 Discovery and history of exploration

The discovery of Ganymede is strictly connected to that of the Galilean moons, whose name is due to the Italian scientist *Galileo Galilei,* which for the first time observed them in a night between December *1609* and early January *1610.*

Simon Marius, a German astronomer, in his *Mundus Jovialis,* named them as lovers of the god Zeus (the Greek equivalent of Jupiter): *Io, Europa, Ganymede* and *Callisto* like we know them nowadays in order of increasing distance from Jupiter.

Galileo, refusing to use Marius' names, proposed the numbering scheme that is still used today in parallel with proper moon names. According to that, moons are represented as *Jupiter X*, with the numbers *X* run from the planet outward. Thus *Jupiter I, II, III* and *IV* stands for, respectively, Io, Europa, Ganymede and Callisto. Galileo's numbered names were used until mid-20^{th} century when other inner satellites were discovered and Marius' names became widely used [19].

Even if a great number of observations were performed in the following centuries, a systematic study of this moons began only in the late *1950s*, culminating in the early *1970s*. In this period telescopic spectral data demonstrated the icy character of these bodies and in particular of Ganymede's surface, indicating also for the first time the presence of a dark component on it. But only with the beginning of spatial age, it was possible to reveal the secrets of these worlds until then just observable from Earth.

The first program with Jupiter as objective was the *Pioneer* by *NASA*: the American spacecrafts *Pioneer 10* and *11* were the first to reach, study and photograph the planet and partially its major moons in December of *1973* and of *1974* respectively. Particularly, the *Pioneer 10* Imaging Photopolarimeter revealed Ganymede's darker and brighter surface tracts.

But for having close-up images of the moons and realising the diversity and complexity of their surfaces, scientists had to wait until March and July of *1979* when other two spacecraft called *Voyager 1* and *2* reached Jupiter. Beside all the more detailed investigations of the planet, all the photos taken allowed to reconstruct the first map of the Galilean satellites, revealing also their major characteristics.

For Ganymede, *Voyager 1* imaging covered much of the subjovian hemisphere at resolutions up to about $1\ km/pixel$ while *Voyager 2* imaged the antijovian hemisphere and high southern latitudes and up to about $500\ m/pixel$, revealing for the first time a characteristic grooved terrain [20] [21].

Even if there was a passage near Jupiter in February *1992* by Ulysses for a gravity assist to reach the Sun's polar regions, the great improvement in our knowledge of the major planet of Solar System and its moons has came from *Galileo* program, a mission started in October *1989* that in December *1995* has put a spacecraft into a Jovian orbit [20].

From next years until *2003*, the craft monitored Jupiter's atmosphere and observed its major satellites from repeated elliptical orbits around the planet, allowing for the first time studies so detailed of these bodies. In particular, during 35 orbits were performed different close approaches to the most important moons, resulted in an enormous amount of data collected through several scientific experiments.

Some fly-bys, in which the distance from them was minor than $200\ km$, resulted in photos of selected portions of surface with an unprecedented spatial resolution until $10\ m/pixel$.

Very important were the observations of Europa which have shown that this moon might have an ocean below its surface capable of supporting life. Also fundamental were studies about Ganymede conducted through the Solid State Imaging (*SSI*) camera, Near-Infrared Mapping Spectrometer (*NIMS*), Photopolarimeter-Radiometer (*PPR*), and Ultra-Violet Spectrometer (*UVS*) between *1996* and *2000*, when *Galileo* spacecraft made six close flybys to explore this moon.

During the first of these the ganymedian magnetic field was discovered; afterwards (in particular thanks to the closest approach, when *Galileo* spacecraft passing just $264\ km$ from the surface of the moon) the discoveries of an ocean and of several non-ice compounds of the surface were announced. Even if high resolution coverage of Ganymede is quite limited in area at present day, *Galileo* has allowed to obtain the better resolution images of ever for this satellite ($< 200\ m/pixel$), that reveal much clearly examples of characteristic terrain and feature types [21]. After *Galileo* spacecraft, other two missions have provided new data and images of the Jovian System.

In a first time, the *Cassini-Huygens* directed to Saturn forecasted a months-long flyby phase around Jupiter during which sent to the Earth over 26000 photos making its closest approach to the planet on December *30, 2000* [22].

Secondly, a more recent ambitious spacecraft flying to Pluto called *New Horizon*s began further study of the Jovian System in December *2006*, receiving a gravity assist from the planet on February *28, 2007*.

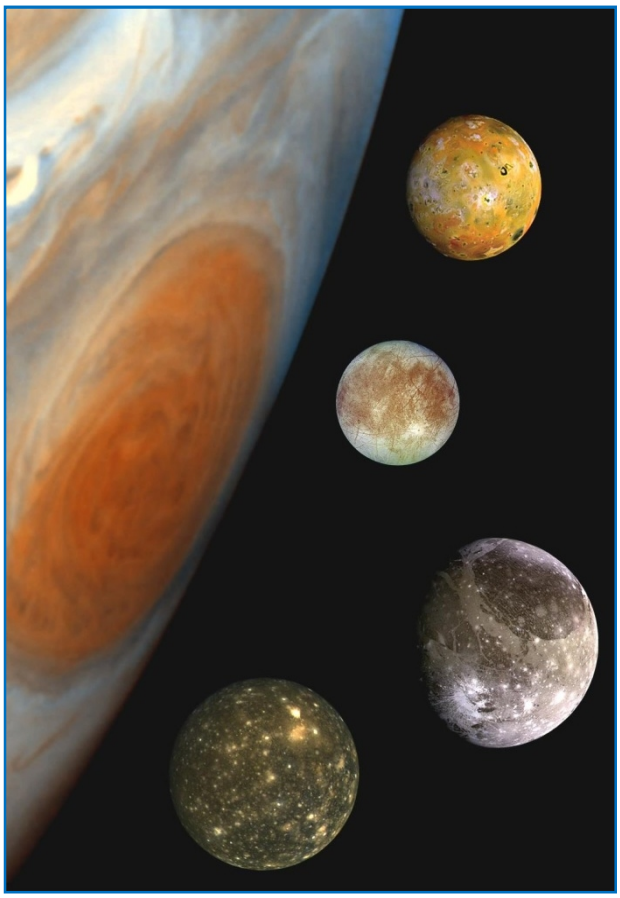

FIGURE 2.2 Composite image of Galilean moons comparing their sizes with the size of Jupiter and its Red Spot (from the top Io, Europa, Ganymede and Callisto) [24]

The on-board instruments made refined measurements of inner moons, studying all four Galilean satellites in detail (in particular it made topography and composition maps of Ganymede) [23]. The picture *2.2* shows how they appear in a dimensional comparison among them and with Jupiter with a particular relief for the Great Red Spot.

Nowadays, a new mission to Jupiter is expected by the whole scientific community to reveal the remaining aspects still unknown particularly about its major moons that are becoming even more interesting also for the putative life that can be sheltered. *EJSM* for the first time in history will foresee an insertion into orbit around the two Galilean satellites Europa e Ganymede allowing a systematic months-longs study.

2.3 Orbit and rotation

According to its orbit around Jupiter, Ganymede, like all the Galilean satellites, is a *regular* and *direct* satellite. This means that it covers a slightly eccentric (near-circular) and less inclined to the Jovian equator orbit in the same rotational sense of the planet at a mean distance of $1070400\ km$, third among the Galilean moons.

Due to solar and planetary gravitational perturbations, eccentricity and inclination change quasi-periodically on a time scale of centuries, variations which cause the axial tilt (the angle between rotational and orbital axis) to vary between 0° and 0,33°. In particular, the ranges of change are $0{,}0009 - 0{,}0022$ for eccentricity and $0{,}05° - 0{,}32°$ for inclination.

Ganymede is also a *synchronous* satellite, meaning that it complete a rotation in the same time in which completes a revolution around Jupiter, about every seven days and three hours, that it its rotational period is equivalent to the revolution one (see orbital parameters in table *2.1*). For this reason, as happens for most known moons and in particular for the system Earth-Moon, Ganymede is tidally locked, showing always the same hemisphere to Jupiter with important consequences about tidal interactions [13] [25].

Beside this tidal interaction with Jupiter, there is also a reciprocal motional influence which ties Ganymede with the two inner Galilean satellites Io and Europa. Indeed, the revolution periods of these three moons are constricted in a phenomena called *Laplace resonance*, in honour of the French mathematician and astronomer who studied it in the *1788*.

A Laplace resonance exist when two or more orbiting bodies exert a regular, periodic gravitational influence on each others. In order to explain it, let take a system formed by a central body C with three objects orbiting around it and let indicate with P_1, P_2 and P_3 their orbital periods; we have a multiple resonance if exist the entire number a, b and c so that:

$$a \cdot P_1 + b \cdot P_2 - c \cdot P_3 = 0$$

Another way to represent this phenomena is using medium angular speeds ω instead of orbital periods because the two quantity differ only for a constant being one the inverse of the other. In fact, considering that $\omega = 2\pi / P$, the three objects are in multiple resonance if:

$$a \cdot \omega_1 + b \cdot \omega_2 - c \cdot \omega_3 = 0$$

A relationship of this kind exists for Io, Europa and Ganymede, for which it values:

$$\omega_{IO} + 2 \cdot \omega_{GANYMEDE} - 3 \cdot \omega_{EUROPA} = 0$$

This means that the couples Io-Europa and Europa-Ganymede are in a $1/2$ resonance, while Io and Ganymede show a $1/4$ one, that is Io's revolution period is half than Europa's and a quarter of Ganymede's and in a same way, Ganymede cover its orbit in a time double respect of Europa's. In other worlds, for one orbit of Ganymede, Europa orbits twice and Io orbits four times [25].

The multiple resonance implies mainly two effects: geometrically, it is impossible that the three bodies align themselves in the same direction respect to Jupiter (see figure

2.3); dynamically, the phenomena forces the eccentricity to be major than zero, forbidding the orbits to be perfectly circular. But it is also the most important reason, together with tidal interactions with Jupiter, why interior of these moons gets hot and melt, giving origin to the volcanic processes and eruptions observable on Io's surface.

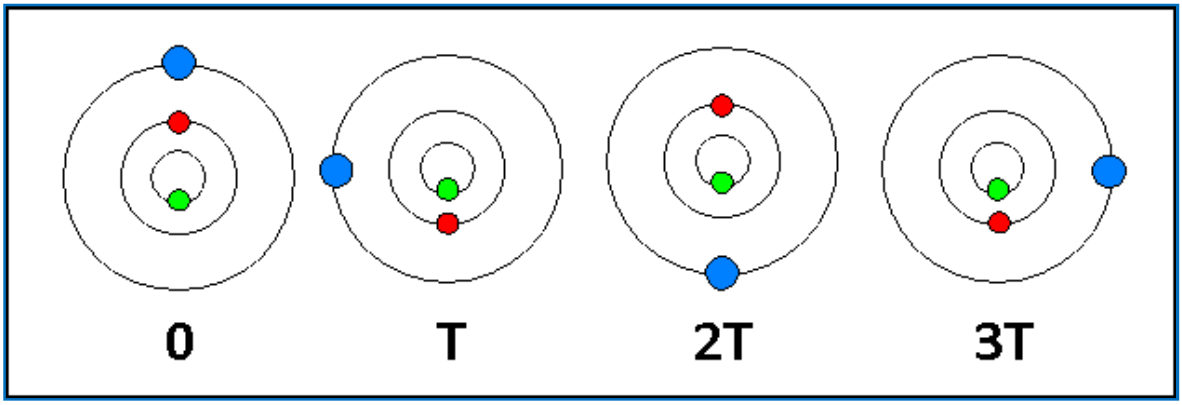

FIGURE 2.3 The impossibility of alignment in the same direction respect to Jupiter for Io (green), Europa (red) and Ganymede (blue). T is the orbital period of Io. Rotation is anticlockwise [26]

In particular, the current Laplace resonance is unable to pump the orbital eccentricity of Ganymede to a higher value than the present one which is about 0,0013, low enough to make the tidal heating of Ganymede negligible now. The present value perhaps is remnant from a previous epoch, when such pumping was possible. Indeed, in the past Ganymede may have passed through one or more Laplace-like resonances which were able to pump the orbital eccentricity to a value as high as $0{,}01 - 0{,}02$. This probably caused a significant tidal heating of the interior of Ganymede; the formation of the grooved terrain may be a result of one or more heating episodes [13].

The origin of the Laplace resonance among Io, Europa and Ganymede is not known. Two hypothesis exists:

1. the phenomena could be primordial and it started from the beginning of the Solar System
2. it developed after the formation of the Solar System.

Moreover, a gradual shift to the extern of the inner satellites' orbits has been noticed, circumstance which, as demonstrated from orbital simulations, will take in a remote future also Callisto to be captured in resonance, with important changes particularly in the geological field [13].

2.4 Geology

Ganymede shows a great deal of geological heterogeneity. The surface is divided into two principle terrain types: relatively old regions of dark terrain and cross-cutting lanes of young bright (typically grooved) terrain, as we can see in figures *2.1*, *2.4* and *2.6*. Dark and bright terrains which take up latitudes between poles and about $\pm 50°$, are covered by the satellite's thin polar caps while the entire surface is marked by several impact craters of a variety of morphologies, including circular bright hardly visible patches known as palimpsests and characteristic of Ganymede.

By analysing surface and its structures from a geological point of view, it is possible to constrain the properties and history of the lithosphere (the external layer of rocks) and of deeper interior and the evolution of the satellite as a whole [21]. A global view of Ganymede's surface with the different structures is provided by figure *2.4*, a mosaic of photos taken by *Galileo* and *Voyager* spacecrafts.

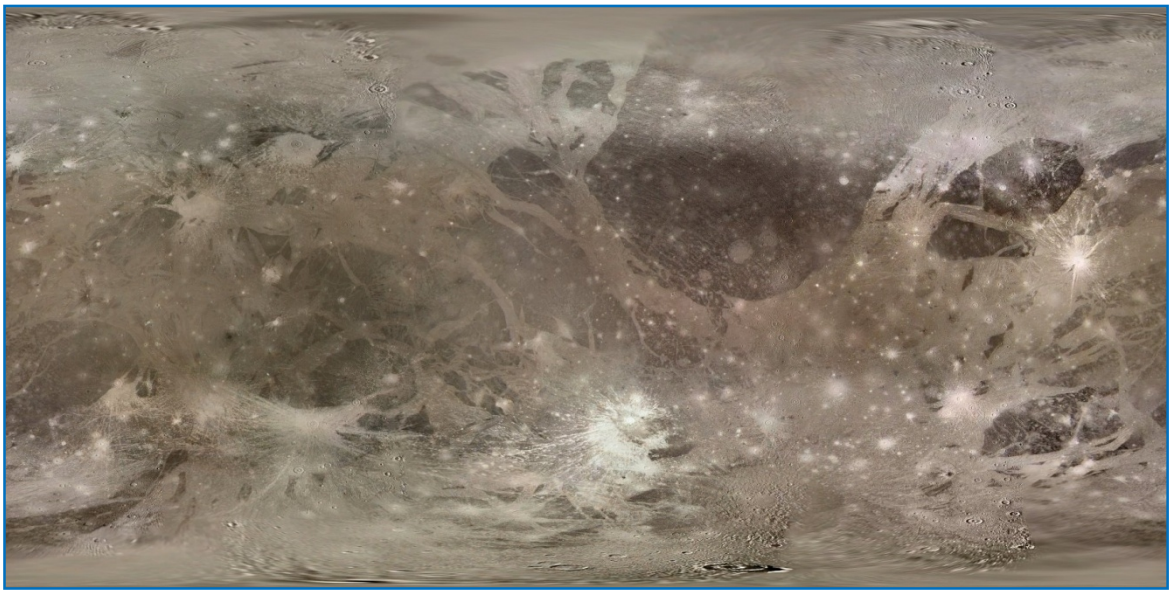

FIGURE 2.4 Global map of Ganymede constructed from Voyager and Galileo images, centered at the antijovian point (0° latitude, 180° longitude) [27]

2.4.1 Dark terrains

About $1/3$ of Ganymede's surface is occupied by areas of heavily cratered dark terrain, each called *regio*. Five *regiones* have been identified and carry the names of the most important scientists which observed the Galilean satellites. The greater dark zone, known as *Galileo Regio* (see figure *2.5*), is a dark plain which occupies about $1/3$ of the antijovian hemisphere with a diameter of about $3200\ km$ [25] [28].

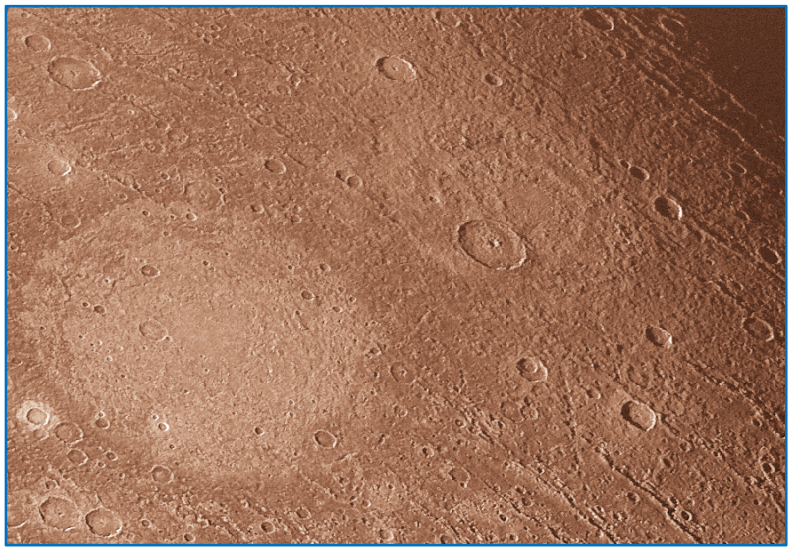

FIGURE 2.5 A portion of Galileo Regio, where it is possible notice its heavily cratered character [29]

At first sight, Ganymede's regiones (see figure *2.1*) can have an apparent analogy with lunar *mari*, that are also them darker than *terrae* regarding the Moon, but in this case the darker character is index of more ancient terrains, also for the great number of impact craters that they present, as we can see in figure *2.5*. Indeed, based on measured crater densities, dark areas are estimated to be over 4 thousand million of years old, therefore this kind of terrain, that has evolved largely through impact events, bears witness to processes affecting Ganymede since the earliest stages of its surface evolution. This is also evidenced by clays, rocks and organic materials that constitute these terrains, elements which indicate the composition of the impactors from which Jovian satellites accreted [21].

Furrow systems. Dark terrain areas are crossed by $\sim 10\ km$ wide troughs termed *furrow systems* which form a complex tangle of folds that seem to fracture at fine-scale the surface (see figure *2.6*).

They are the oldest recognizable structures on the surface of Ganymede, remnants of vast multi-ringed structures probably formed during a period of geologic activity and predate almost all craters larger than $10\ km$ in diameter, providing in part evidence that dark terrain represents a very ancient surface.

The majority of the furrows are arranged in sub-concentric sets, although some cross-cut the others at high angles. Because dark terrain is significantly disrupted by younger swaths of bright terrain, furrow systems are generally incomplete but, if they have preserved intact, would have been hemispherical, like the largest system of this kind known as the *Lakhmu Fossae* in *Galileo Regio*, observable in figure *2.6*. However, furrows are shallower and more subdued than multi-ringed basins on terrestrial planets.

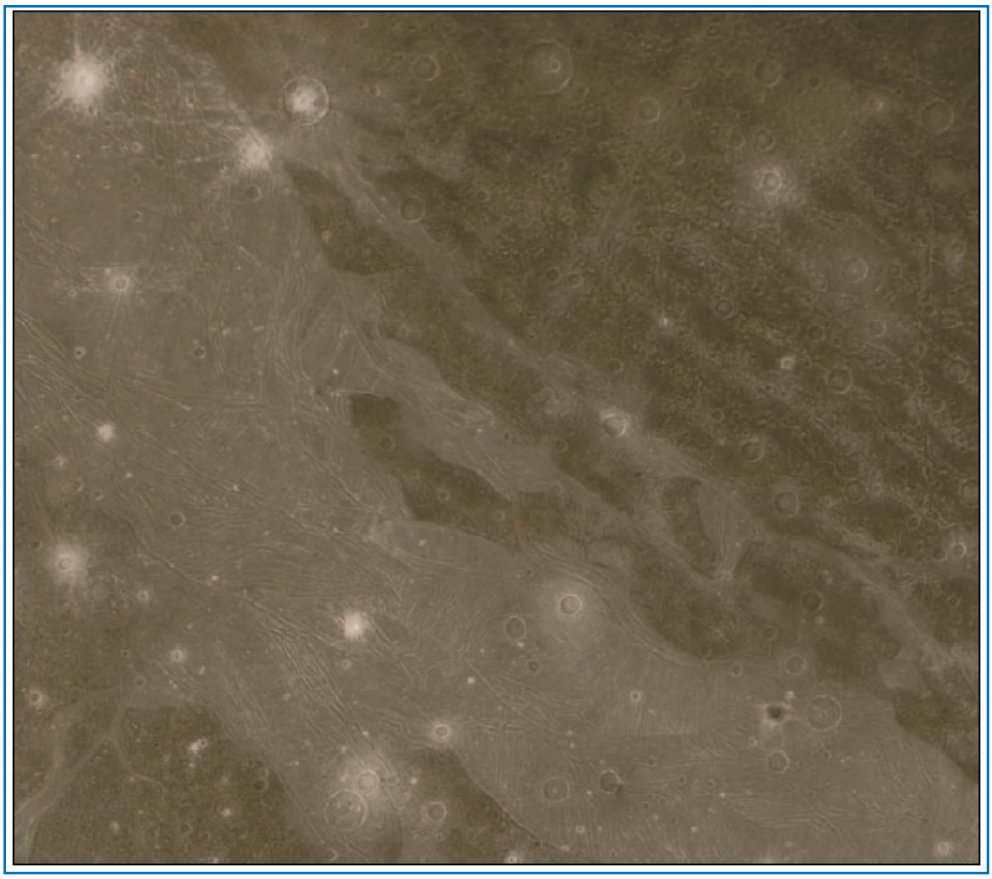

FIGURE 2.6 Boundary between the furrowed dark terrain of Galileo Regio (upper right) and the bright grooved terrain of Uruk Sulcus (lower left), as imaged by Voyager [30]

Individual furrows are linear or curvilinear troughs which extend from tens to hundreds of kilometres in length and are typically about 6 to 20 km wide and few hundreds of metres deep, with generally flat floors and sharp raised rims as boundaries.

Spacing among them is fairly uniform at ~50 km, although furrows are generally closer towards the centre of a concentric system. Topographic models derived from high resolution images of *Galileo Regio* show that a rim rises a full kilometre above its furrow floor and 900 m above the level of the surrounding terrain.

By geological analysis, a variety of models for furrow systems formation has been suggested. Today, it is generally accepted the idea that individual furrows likely formed early in Ganymede's history in response to much violent impacts which fractured a vast area of the crust, very thin at that epoch.

Folds now visible surrounding the major crater basins, traces of ancient system of concentric ringed structures, is the result of radial inward flows accompanying brittle failure of the lithosphere. This hypothesis explain also the morphological similarities of

furrows to the sinks of terrestrial crust between parallel faults and to impact-formed multi-ringed structures on Europa [21].

High resolution albedo heterogeneity. Dark terrain is relatively homogeneous in albedo at a large scale while at high resolution it appears surprisingly heterogeneous, probably because sublimation and thermal segregation of ice and non-ice surface material.

This heterogeneity implies that the ice and non-ice components are distributed irregularly across the surface. In particular, based on relative albedo, morphology and geological occurrence, it is possible to identify a variety of sub-units common to the majority of dark terrain areas, also well-separated among them. This sub-units are indicated in figure *2.7*, a high resolution image of *Galileo Regio*. Intermediate albedo plains (I) are the oldest recognizable units and also the most diffuse, occurring around both higher and lower topographic features. This unit may represent areas of Ganymede's crust that have been heavily modified by later surface processes.

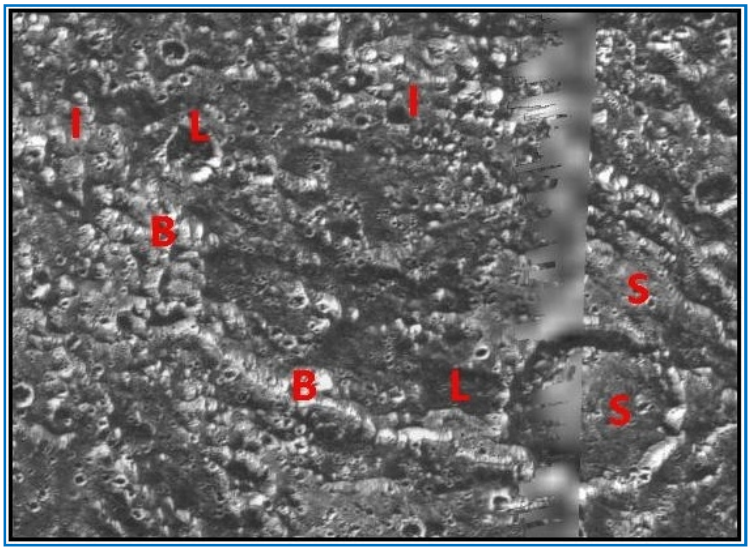

FIGURE 2.7 Significant heterogeneity of dark terrain in Galileo Regio: low-albedo plains (L); intermediate-albedo plains (I); bright units (B); smooth plains (S) [31]

The low albedo unit (L) is recognizable only in topographic lows, particularly on the floors of furrows and other low-lying areas, and is interpreted to be loose dark non-ice material collected there because down-slope movements from adjacent furrow walls. This provides strong evidence that mass wasting has been an important modification process in dark terrain. The presence of low albedo streaks at the base of otherwise bright slopes is another element to support downslope movement of Ganymede's dark material.

Bright units (B), generally associated with topographical highs, form curvilinear units, like furrow and crater rims or isolated massifs, which are actually remnants of furrows or crater rims that have been disgregated through tectonic activity too much that original forms are now unrecognizable. All albedo units are surrounded by quite smooth

higher albedo mantles, relatively young units interpreted to be impact ejecta because they occur in close association with impact features [21].

Tectonism and icy volcanism. Tectonic deformation and icy volcanism, although generally more abundant in bright terrains, have had an important role also in dark terrain evolution. An example of heavily tectonized dark terrain is found in the portion of *Nicholson Regio* imaged by *Galileo* (figure *2.8)*. In this area there is evidence of several sets of closely spaced fractures trending in several orientations, which roughly follow those of near older furrows.

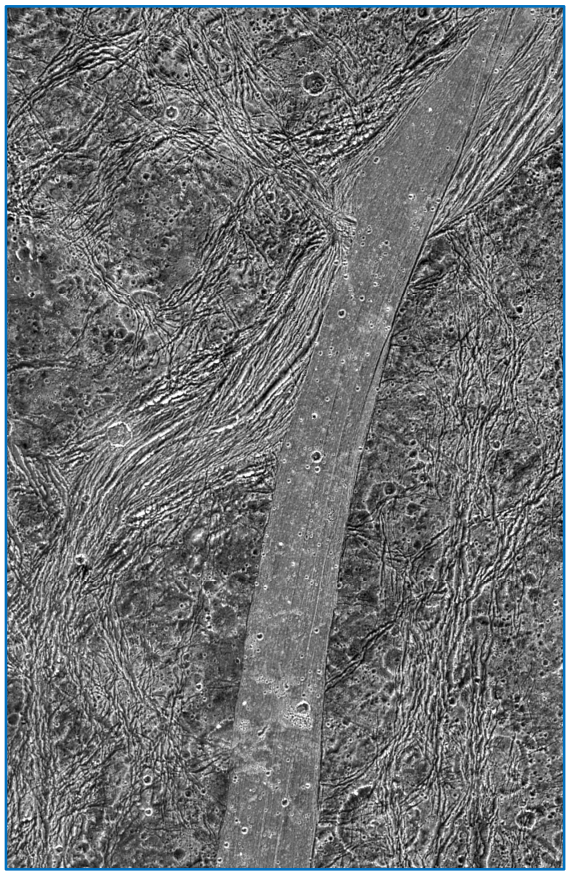

FIGURE 2.8 A portion of Nicholson Regio where the dark terrain is straddled by grooved terrain and show evidence of heavy tectonic disruption. The swath of smooth bright terrain is Arbela Sulcus [31]

This implies that tectonism have operated exploiting pre-existing weaknesses of the terrain, due to the earlier formation of furrows and craters, able to focus tectonic deformation through them. In some cases (see figure *2.8*) two differently oriented fracture sets intersect near or within a crater basin, a phenomenon of tectonic focusing analogous to that observable near terrestrial calderas, where faults follow the directions of weakness. Generally, dark areas far from grooved terrain are characterized mainly by furrows, while regions closer to grooved terrain present an additional fracturing directed along pre-existing structures.

Dark terrains bear also a slight witness of a past effusive icy volcanic activity, recognizable in extrusion of icy materials into crater floors to form domes and in smooth areas associated with furrows. According to this, dark terrain would consist of an old heavily cratered surface buried by overlapping blankets of icy volcanic material [21].

Sublimation. Unlike to what might be expected, dark material seems to concentrate on slopes facing to the direction of solar illumination, while brighter slopes face away from it. This is an important proof that dark terrains are interested by processes like sublimation and deposition of volatiles element, specifically H_2O.

Indeed, in those zones which receive directly solar radiation, like sun-facing slopes, or where topographic configuration tend to concentrate infrared radiation from the surroundings, water vapour is removed, leaving behind a low albedo material deposit, thus forming a surface darken than before. When enough dark material has been accumulated, it begins to slough downslope and consequently a relatively high albedo ice-rich surface is revealed. On slopes these dark deposits probably are few metres to tens of metres deep, but they are deeper in topographic lows such as furrow floors.

Obviously, water vapour can condensate only on relative cold pole-facing slopes and topographic highs, where brighter areas have been found. Sublimation seems to be also the major reason for erosion of scarps that bound impact features in the dark terrain [21].

Model of dark terrains. All the observations and geological investigations suggest a model for dark terrains in which low albedo material forms a relatively thin dark silicate-rich deposit overlying a brighter icier substrate, which presents a small amount of a low albedo component heterogeneously admixed, maybe emplaced by impactors during Ganymede's accretion. Disposition and concentration of different materials are the result of a variety of surface processes including mass wasting, tectonism, icy volcanism and sublimation.

According to this model, high albedo units, such as craters and furrow rims or topographical highs, would be outcrops of icy substrate from which the dark deposit has been removed or zones in which bright sublimated material has been trapped. Instead, non-ice dark material is concentrated in the warmest regions and local topographic lows, notably sun-facing slopes and floors of troughs, where volatiles have been removed.

Large impacts have penetrated the external dark layer of surface to deeper ice-rich substrate, uniformly mixing the impacted material to create relatively bright ejecta [21].

2.4.2 Bright grooved terrains

Differently from dark terrain, the main part of bright terrain does not extend on vast regions but forms across 2/3 of Ganymede's surface a global intricate network of large interconnected lanes tens to hundreds of kilometres wide, which separate the dark areas that appear like isolated patches (see figure *2.1* and *2.4*).

These elongate swaths of bright terrain are known as *sulci*. One of the most interesting among 32 defined sulci, is surely *Uruk Sulcus* (see figure *2.6*), made up of complex series of streaks with mean lengths of $4-5\ km$ that form the southern-western boundary of *Galileo Regio* [28].

Within each swath, bright terrain is arranged in an intricate patchwork formed by systems of interconnected closely-spaced parallel furrows, ridges and troughs termed *grooves* (see figure *2.9*) which are dominated by extensional tectonic features and morphologically have much in common with terrestrial rift zones.

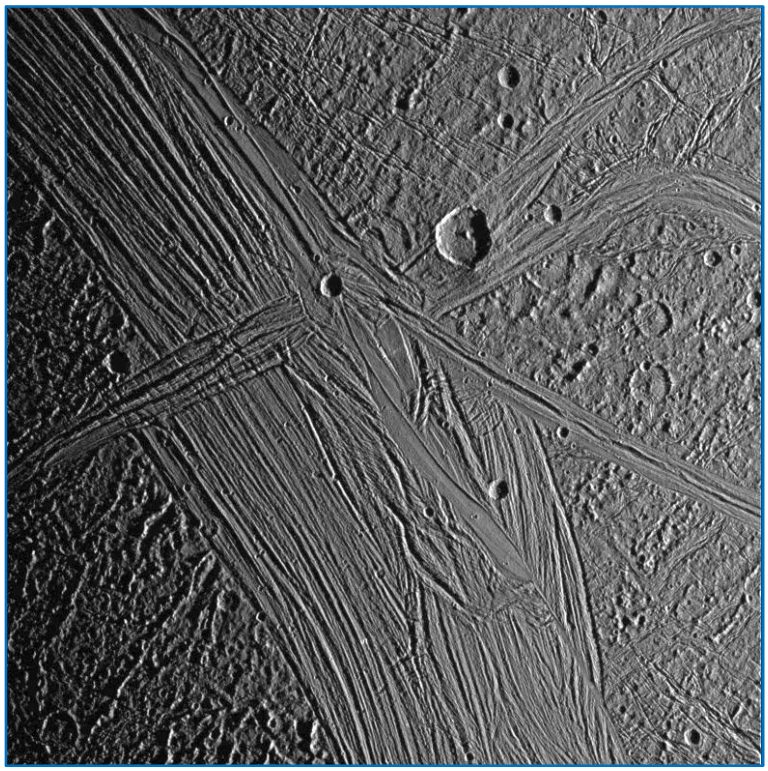

FIGURE 2.9 Closely-spaced roughly parallel ridges and troughs in Tiamat Sulcus [31]

Bright grooved terrain is surely younger than dark terrain having a nominal age of about 2 thousand million of years. This can be derived from crater densities 2 to 10 times less than dark terrain and the absence of structures like palimpsests but also from a major reflectivity, index of the fact that there have been less time for accumulation of dust deposits that darken surface. However, large uncertainties in the impact flux through time imply that grooved terrain may have an age that runs from about 400 millions to more than 4 milliards of years [21].

Grooves and smooth terrain. The most of surface occupied by bright terrain is ruled by sets of curvilinear subparallel alternating ridges and troughs, organized in elongate swaths or truncated polygons, which can continue along their direction for hundreds of kilometres.

In a single set, ridges and troughs, until $700\ m$ deep and distant each other generally $10 - 15\ km$, commonly trend subparallel to the long axis of the elongate cell of bright terrain in which they occur, but they can also trend obliquely to a polygon's long axis in regions of complexly intersecting sulci (see figure *2.6*). It has been noticed that generally grooves within a set are typically less prominent than those situated on the boundary of a single cell. In *Uruk Sulcus* (see figure *2.11*) topographic amplitudes reach $\sim 500\ m$ with ridges and troughs having crest-to-floor height differences typically of $300 - 400\ m$ and as great as $700\ m$ and maximum slopes around 20°.

Even if dimensions are comparable with those of furrow systems, actually there is an important difference between the two structures: in the case of grooves disposition is highly regular and tidy and their wall presents more rounded borders and minor slopes.

Only rarely the order is broken by a groove intersecting another one while it is not such difficult to find a swath of bright terrain that intersect an other bright band also near-orthogonally cancelling the pre-existing formation, as we can see in figure *2.10*.

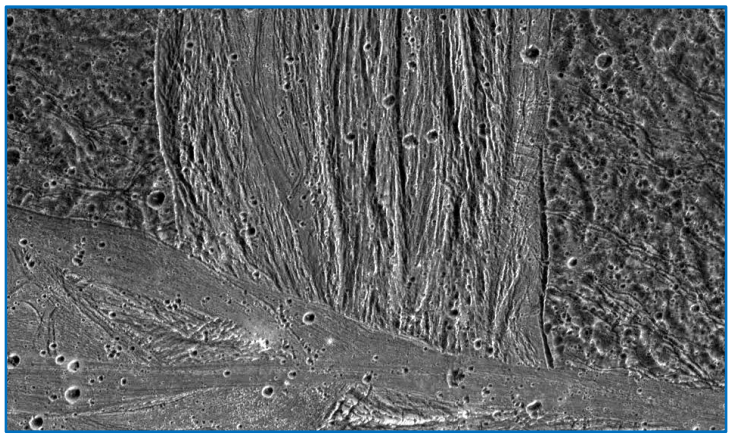

FIGURE 2.10 Swath of bright terrain which intersect near-orthogonally another swath in Erech Sulcus [31]

However, intersections between grooved terrain generally appears much complex. From high resolution images it is possible notice how newer grooved terrain can destroy the groove topography of older ones (in some cases leaving no recognizable trace of older structures) creating the observed complex array of cross-cutting swaths. In other cases, newer grooved terrain structures end against older more prominent grooves in T-terminations, where the cross-bar of the T was inferred to be older. Also regions of reticulate terrain formed by orthogonally intersecting troughs have been found, maybe representing intersecting groove sets in which the pre-existing grooves have been preserved [21].

Albedo heterogeneity. Since the *Galileo* first high resolution images, it has been revealed an important albedo heterogeneity also in grooved terrain, where distinct albedo lineaments aligned with ridges and troughs have been found. As it is possible notice from the image on the left of figure *2.11*, these features characterize mainly the *Uruk Sulcus*, in which albedos between the bright and dark lineaments differ by a factor of 3 [32].

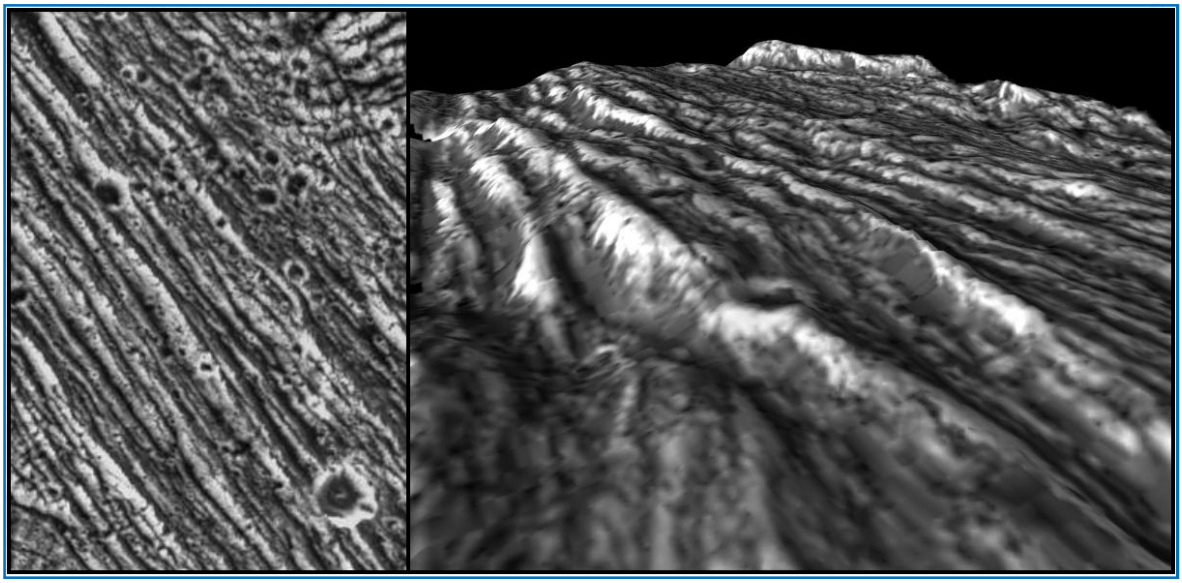

FIGURE 2.11 Fine-scale albedo and topography of grooved terrain in Uruk Sulcus. Correlation brightness-topography (left) and simulated view generated using stereo imaging [31]

Oberst et al. [32] have conducted a study about possible relationships between surface brightness, elevation and slopes, inferring that most of the variations in surface brightness in the images do not represent photometric shading effects but likely are caused by the segregation of at least two distinct bright and dark surface materials with contrasting albedos.

Describing the surface optical properties with the Hapke's photometric parameters determined using measurements of surface brightness, they have confirmed the close correlation of apparent terrain brightness to topography.

Firstly, examining the areal distribution of different type of materials in relation to elevation and plotting brightness data versus altitude, they have found a strong relationship between material locations and elevation: the darker material occurs more commonly in local depressions between ridges (topographic lows), bright material is generally located on ridge crests (topographic highs) while intermediate albedo material is common on ridge slopes with intermediate elevations which cover the full range of brightness (see stereo image on the right of figure *2.11*). Therefore variations in brightness clearly follow elevation data, even if the local maxima and minima in brightness and elevation seem to be

unlinked based their absolute values. Often, the relative abundance of dark material increases toward the bottom of the topographic troughs, with surface becoming increasingly dark in the down-slope direction.

Secondly, analyzing brightness-slopes correlation, Oberst et al. have seen that both bright and dark materials are evenly distributed on moderate slopes $< 10°$. In particular, while in dark terrain a large fraction of bright material is found on slopes near $10° - 20°$, in the grooved terrain data show that on steeper slopes ($> 10°$) the dark material prevails.

Moreover, graphics reporting brightness versus down-slopes azimuth have revealed that the bright material is located mostly on slopes facing the north direction rather than on the top of the ridges.

This effect is very clear in topographic features such as impact craters and suggests an important role for effects associated with solar illumination and topographic shading, as described in paragraph *2.4.1* devoted to *Sublimation*.

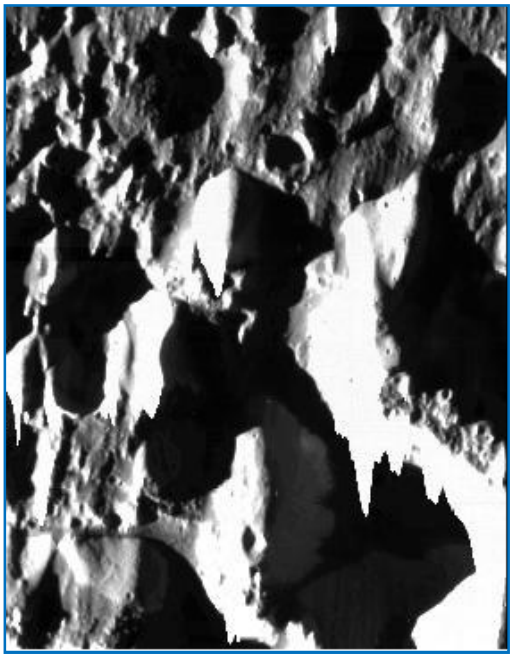

FIGURE 2.12 The highest resolution image obtained for Ganymede reveals massives and undulatory intervening [31]

Several possible examples of mass movement and landform modification are recognizable in the highest resolution image of Ganymede ($11\ m/pixel$), acquired near *Xibalba Sulcus* by *Galileo* (figure *2.12*). At this high resolution almost nowhere on the surface is really smooth; rather are visible some craters partially filled by debris and several perhaps eroded massives and hummocks. The erosional hypothesis agrees with measured slopes, usually less than $\sim 10°$ and rarely approaching $\sim 20°$, and the undulatory roughly textured character of the surface between the hills. Superimposed dark steaks, which occur on steep slopes and are oriented downhill, provide further evidence of mass wasting, being made up by loose material that has moved downslope [21] [32].

Tectonism. From high resolution *Galileo* images, it is evident that bright terrains exhibit the full range of extensional tectonic behaviour, including wide and narrow rifting, a significant role for tilt-block style normal faulting, locally high extensional strains, the potential for tectonism alone to cause the resurfacing of some groove lanes through

destruction of pre-existing topography, possible examples of local crustal spreading and a less prominent role for icy volcanism.

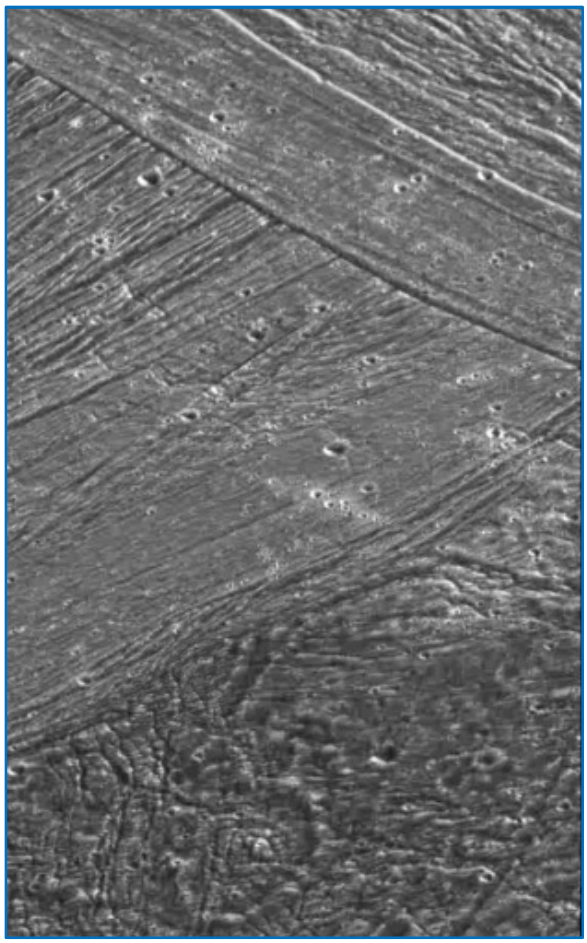

FIGURE 2.13 Boundaries between grooved terrain of Philus Sulcus and Nippur Sulcus. Philus Sulcus displays grooved terrain with a ridge-and-graben-like morphology [31]

The more common morphology of grooved terrains is kilometre-scale blocks resembling flat-floored graben (typically narrow and somewhat V-shaped in cross-section) with intervening flat-topped ridges (triangular to rounded in cross-section). A morphology like this (narrow triangular ridges and similarly shaped troughs with no topographic break in between) is suggestive of tilt-block-style normal faulting, where arrays of normal fault move in the same direction so that this motion induces back tilting of the surface. In particular, rather than developing along distinct bounding faults, deformation has occurred by cumulative displacement along several of the fractures or faults pervading grooved terrains in question. Examples have been found within *Philus Sulcus* (see figure *2.13*) and at higher resolution within *Uruk Sulcus* (see figures *2.11*). This style of normal faulting, also called “bookshelf” or “domino-style” because of the similarity to a set of tilted books or dominoes, creates regularly spaced ridges and troughs, with the faulted layer thickness proportional to the fault spacing.

Boundary relationships give strong support to an extensional tectonic origin for grooved terrain and can explain the topography of groove sets dominated by tilt-block faulting. Indeed, the prominent bounding troughs alongside some lanes of bright terrain can be seen like the deep trough which commonly marks the edge of a terrestrial rift zone, reflecting the presence of a prominent boundary fault and deformation of the hanging wall fault block, generally associated with terrestrial tilt-block domains.

Galileo high resolution images, particularly those of *Uruk Sulcus*, have also provided a reason to believe that a process termed tectonic resurfacing may have attended in grooved terrains formation. Indeed, with the exception of small smooth patches, the surface of the major part of bright terrains is ruled by an often complex network of intersecting lanes, in which some newer grooves have partially erased pre-existing older ones, in some cases altered beyond recognition. Moreover, within strained craters, features such as central peaks or domes are absent, suggesting that these pre-existing structures may have been rendered unrecognizable because of tectonic resurfacing [21].

Icy volcanism. High resolution images don't provide a clear morphological evidence for icy volcanism.

Indeed, features like lava flow fronts or source vents are absent and eruption of liquid water through an ice-rich crust may seem difficult because of the mayor density of the melt compared to the solid (even if these features may have been destroyed by fracturing and erosion and ice may have erupted in the solid state through a colder and denser crust).

Nevertheless, indirect evidence for volcanic resurfacing of grooved terrain has been identified for example in at least 18 (probably more than 30) scalloped depressions called *paterae* which could represent caldera-like source vents for icy volcanism. High resolution *Galileo* image of figure *2.14* shows the largest patera within *Sippar Sulcus*.

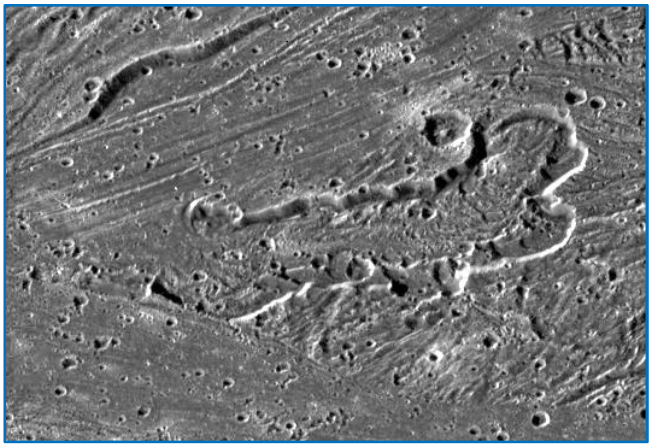

FIGURE 2.14 Most prominent example of scalloped depression known as patera in Sippar Sulcus [31]

Two features in particular suggest an origin by icy volcanic resurfacing. Firstly central floor deposits (interpreted as formed by icy flows) which reach up to $800\,m$ above surrounding grooved terrain, such for patera's rims; secondly the relatively smooth terrain in the central zone of the region which lies at roughly constant elevation over great longitudinal extent and is depressed 250 to 1000 metres below surrounding terrains, maybe the result of flooding of pre-existing troughs to an equipotential level by low-viscosity aqueous lavas. Probably the smoothest area identified at high resolution is within *Harpagia Sulcus* near its boundary with *Nicholson Regio* (see figure *2.15*).

According to images, it appears very smooth at regional resolution but very rough at the scale of hundreds of meters, containing many degraded linear parallel scarps with $\sim 200\ m$ of local topographic relief, presumably tectonic in origin. Also here, a reasonable origin for the relatively smooth material between individual ridges can be volcanic embayment, with low-relief areas examples of plains emplaced by low-viscosity icy volcanic flows.

Anyway, virtually all smooth bright terrains exhibit some degree of tectonic overprinting; therefore, it is clear that icy volcanism on Ganymede, if occurred, is intimately associated with tectonic processes [21].

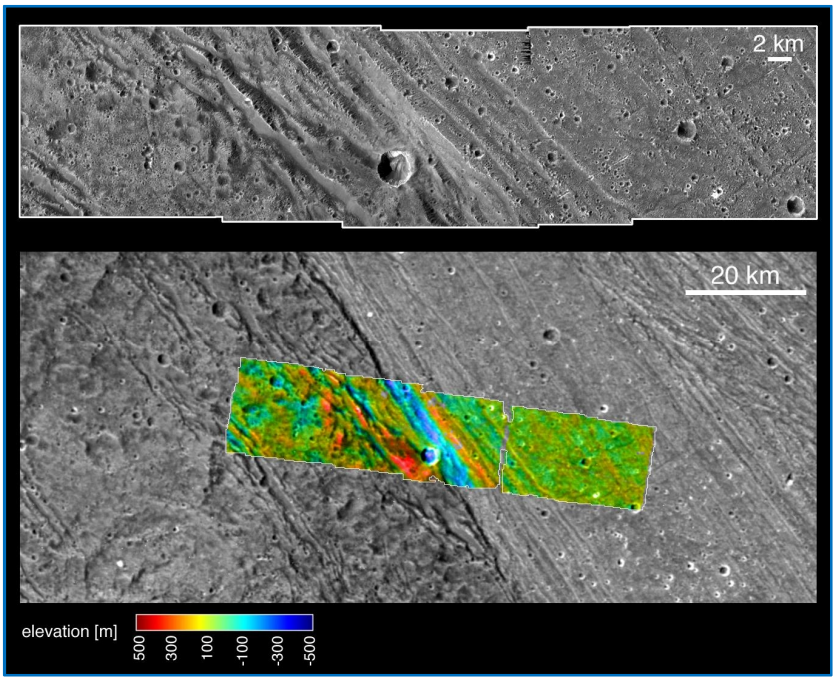

FIGURE 2.15 The smoothest area identified in bright terrain of Harpagia Sulcus near its boundary with Nicholson Regio [31]

Formation models for bright terrains. Overall, two models have been suggested to explain how grooved terrains formed. According to the first, bright cells are broad graben that have been filled by extrusion of relatively clean silicate-poor liquid water or warm ice or icy slush that solidified to ambient temperature.

This model can be described through three steps [21]:

1. formation of fault-bounded graben in dark terrain;
2. volcanic eruption of relatively clean water and ice to resurface the existing terrain, flooding the broad graben and creating bright relatively smooth areas;

3. tectonic extension to produce grooved terrain, either as sets of narrow subparallel ridges and troughs or as fractures, subsequently modified through relaxation, mass wasting and erosion.

The second is a rift-like model which supports, like the first, an extensional tectonic origin of grooved terrains. According this, the evolution of bright terrains has occurred in four key stages [21]:

1. reactivation of dark terrain tectonic structures;
2. extensional tectonic deformation of pre-existing terrain;
3. possible icy volcanic resurfacing;
4. cross-cutting by more recent lanes of grooved terrain (tectonic resurfacing).

2.4.3 Polar caps

Voyager observations before and those of *Galileo* after have shown continuous diffuse bright deposits of water frost without relieves, known as the polar caps, which mantle regions poleward of about $\pm 40°$ latitudes.

The surface at these high latitudes presents an overall brightening, but at high resolution it has a dominantly bright mottled appearance with local thicknesses measured in terms of meters or more. In particular, the caps are very thin at their boundaries and increase in thickness toward the poles while significant variations in albedo, which preferentially occur on slopes facing towards the poles, suggest a strong heterogeneity in the distribution and thickness of the polar frost deposits.

Several hypotheses have been proposed to explain the presence of the polar caps. In particular, the colder environment of the high latitudes may simply favourite water-frost deposits to remain longer; alternatively, frosts may accumulate at these high latitudes by cold-trapping of water ice sublimated (preferentially from the equatorial regions) because of solar radiation or removed by bombardments due the Jovian radiations belts.

Moreover, the polar caps pronounced margins coincide with the boundary between magnetic field lines that are open and those that are closed to plasma, suggesting a possible causal relationship.

In particular, whereas Ganymede's magnetic field deflects most charged particles in the satellite's equatorial regions canalizing this plasma towards the polar regions, it was

suggested that plasma particles trapped within field lines bombard the surface damaging ice grains and thus, exiting them, brightens the polar caps.

In addition, sputtering due to charged particles may redistribute polar ice, with consequential thermal segregation acting to create the albedo heterogeneity and the observed topographic muting of some craters within the caps [21].

2.4.4 Impact structures

A very great number of impact craters have been observed on Ganymede's surface on both types of terrain and more than 100 among them have been classified. But Ganymede displays also the greatest diversity of primary impact morphologies on one planetary surface in the Solar System (see figure *2.16*), with some features unique for it and its sibling Callisto.

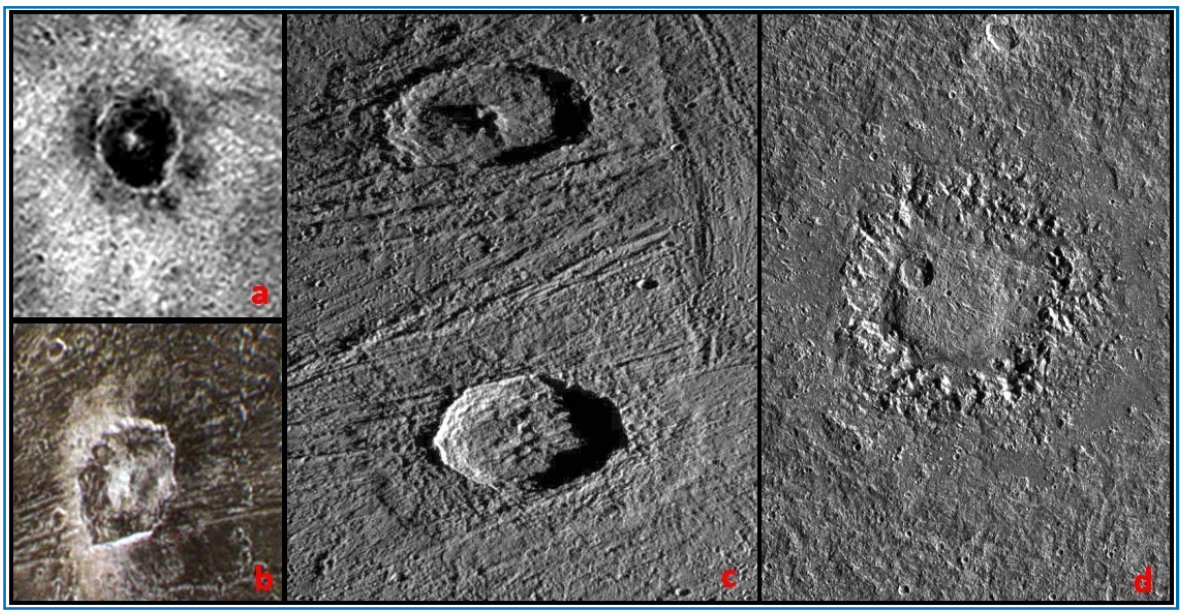

FIGURE 2.16 Examples of crater types on Ganymede: a) dark floor crater Khensu (13 km); b) dark ray crater Kittu (15 km); c) central peak crater Gula (38 km) (top) and pedestal crater Achelous (32 km) (below); d) central dome crater Neith (160 km) [31]

The different types of craters recognized include:

- bright ray craters
- dark ray craters (figure *2.16 b*)
- dark floor craters (figure *2.16 a*)
- pedestal craters (below in figure *2.16 c*)
- central peak craters (top in figure *2.16 c*)
- central dome craters (figure *2.16 d*)

- palimpsests (figure *2.17*)
- vast multi-ring structures (sub-concentric furrows seen in paragraph *2.4.1*)

The oldest known crater type, predating bright terrain, is represented by circular in albedo structures of bright coloration with muted barely visible concentric conformation termed *palimpsests* (see figure *2.17*).

They are recognizable against dark terrain as low-relief bright patches and appear as "ghost" craters because their relief has been erased with time, leaving only an ancient impact scar on the surface. Palimpsests are most abundant in dark terrain, covering about $1/4$ of the regiones' surface with diameters until $200 - 300\ km$.

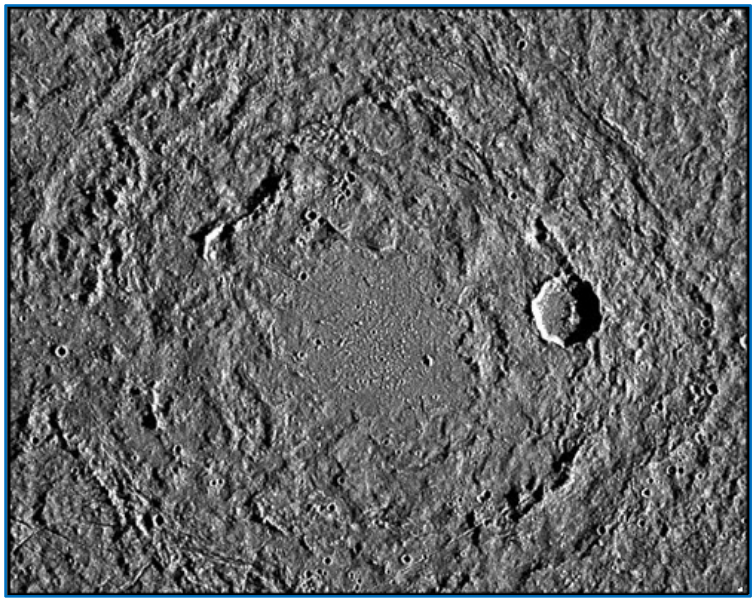

FIGURE 2.17 Buto Facula palimpsest within Marius Regio. The bright margin corresponds to once-fluid ejecta [31]

Subsequent large impacts morphology is often characterized by the formation of bright central domes (see figure *2.16 d*), inferred to be exposures of Ganymede's shallow interior, formed as a result of uplift in the centre of the crater of relatively ductile material from depth.

More recent impact craters on Ganymede, which are the best preserved and until $3 - 5\ km$ deep, can have bright, presumably ice-rich impact ejecta (see figure *2.16 a*), or dark, presumably less icy ejecta (see figure *2.16 b*). The greatest among these are generally surrounded by bright rays of icy material expelled during their formation: impact may have destroyed the external layer of rocks and dust such to expose the ice underlying it. The smallest, instead, with diameters from 10 to 20 km and depths of few kilometres, usually

present low albedo contours. For this reason, they are identified as dark ray craters and seem to represent a phenomenon unique for Ganymede.

Craters of this type are present also in bright terrain, showing a preferential distribution near the equator and mainly on the *trailing* hemisphere (the hemisphere turned in the opposite direction respect to that of motion advancing; hemisphere turned in motion advancing direction, instead, is called *leading*).

According to this observation, the rays may be a deposit enriched in projectile material, concentrated by sublimation and charged particles bombardment on the trailing hemisphere but disrupted by micrometeorite bombardment on the leading hemisphere (even if charged particle bombardment in equatorial regions doesn't seem to be so intense).

A more likely hypothesis, derived from colour analyses, claims that at least some dark rays are due to contamination by impact material. In particular dark rays material visible spectrum of *Kittu* crater (see figure *2.16 b*) is consistent with C-type impactor material, while other dark ray craters spectra are very similar to those of D-type asteroids.

Dark floor craters are widely distributed over dark and bright terrains both as small (kilometre scale) and larger (typically ten or more kilometres in size) fresh-appearing impact craters (see figure *2.16 a*). Dark floor deposits, which have the lowest albedo of any features on Ganymede, are probably sediments of dark impact material, or the remnants of a mixture of impact and icy material from which the volatile constituents were lost by vaporization.

Generally, ganymedian craters have a flatter and more subdued character (specially oldest impact structures like palimpsests) than those on the Moon and Mercury, probably because on Ganymede large craters were unable to retain their topography over geological time in a relatively weak icy crust, which could flow and thereby soften the relief.

Anyway, all the interpretations indicate viscous relaxation as the driving force for evolution of crater morphology and imply a much warmer shallow crust and steeper thermal gradients early in Ganymede's history than at present, with more recent impact structures reflecting a thicker and stiffer elastic lithosphere [21].

2.5 Surface composition

Analysing Ganymede's surface, the general impression is that it is mostly covered by water-ice with a small amount of non-ice material and that it presents spectral characteristics intermediate between those of Europa and Callisto. Recently the *Galileo* spacecraft greatly improved our understanding of Ganymede's surface, providing, in particular, direct spectral evidence of major non-ice constituents and revealing the details of major and minor species, besides some correlations between compositional information and surface geology.

Ice. Ground-based spectroscopic observations, specifically those in infrared, have shown a strong spectral signature of H_2O molecules, providing evidence that water ice is the major constituent of the Ganymede's surface. Water ice, probably the result of thermal processing interesting water and water-bearing materials which originally constituted the satellite, forms an upper layer of white frost laying on a solid ice substrate, with characteristic absorption bands varying in strength depending on abundance, particle size, and degree of crystallinity.

In particular, from the spatially resolved *Galileo* observations, water ice on Ganymede seems to be ubiquitous on the surface with a mass fraction until 90% (more than in Ganymede has a whole) and is more abundant on the bright terrain than on dark one, particularly concentrated at the poles and away from the trailing side. Moreover, both amorphous (predominant at the poles) and crystalline forms are evident with a 0,1 to 1 mm grain size range, greater than Europa's and less than Callisto's.

The band depths of the water-ice absorption features suggest the presence of larger grained ice ($> 300\ \mu m$) in the trailing hemisphere, especially in its equatorial regions, and a little finer grained one in the leading side, with finest grained deposits in the range 20 to $50\ \mu m$. The trend towards larger grain sizes on the low latitudes of trailing side is consistent with increased sputtering removing ice from the trailing side with the water molecules re-depositing as a frost elsewhere, especially at colder sites such as the poles and colder higher-albedo areas.

Ice spectra show also that the surface in at least equatorial and mid-latitudes is arranged in discrete patches of ice and non-ice material, suggesting that there is no or just a little intimate mixing between these two components, probably because of an uneven surface temperature distribution resulting in uneven cold-trapping of H_2O molecules [21].

Dark material. Telescopic spectroscopic observations and dark and light markings on the surface, observed by *Voyager* and *Galileo*, suggest the presence of considerable and widespread non-ice material on and in the surface of Ganymede.

Even some ice-free regions, composed for more than 80% by non-ice dark materials, have been revealed, particularly on the trailing hemisphere. Absorption bands found in many areas of non-ice dark material differ, for wavelength positions and band shapes, from those of pure water ice indicating the presence of hydrated minerals bounded with H_2O, whose spectral signatures vary depending on the particular mineral, the bonding configurations and temperature.

Even if the spectral evidence for such materials is difficult to discern in the infrared, due to strong water-ice absorptions that can hide their spectral signatures, spatially resolved spectra show that hydrated minerals are abundant on Ganymede at an average level of ~40 to 50%, mainly in equatorial and mid-latitudes areas. Moreover, it has been pointed out that the hydrated absorptions for some zones of Ganymede are identical in both shape and wavelength positions to those on Europa, evidence of similar hydrated materials on both satellites, with Ganymede's materials less hydrated.

Based on this analogies, it has been suggested magnesium sulphate $MgSO_4$ hydrate or sodium sulphate Na_2SO_4 hydrate as likely candidates for the majority of the hydrated minerals on Ganymede.

The presence of hydrated minerals on surface may be explained referring of some results from the *Galileo* magnetometer which would imply a conducting water-rich layer deep beneath the surface (maybe a briny ocean) that, according to the thermal evolution model leading to Ganymede's differentiation, would have been at significantly shallower depth in the past.

For this hypothesis, water circulation would have produced hydrated materials leaching ions from the satellite's interior materials and, through water migration toward the surface, these materials would have been left on it.

Hydrated materials can also potentially formed by radiolysis (chemical decomposition of some species due to a ionizing radiation) involving sulphuric acid hydrate present on surface or by depositing of brines coming from Europa, which reached the surface of Ganymede at some time in the past [13] [21].

Other components. In addition to the materials present in major quantities, on Ganymede's surface there are other less abundant molecular species.

Telescopic observations have revealed, in particular, the presence of trapped oxygen in several forms mainly ozone O_3, which seems to be allocated only in the trailing hemisphere both in polar regions and at low latitudes (here near sunrise and sunset), and diatomic oxygen O_2, strongly concentrated always on the trailing side and with a liquid-like spectrum, probably due to the closeness of molecules trapped in the ice surface.

The depth of absorption bands depends on latitude and longitude rather than on surface albedo: those of diatomic oxygen tend to decrease with increasing latitude, while the ozone shows an opposite effect.

The concentration of the oxygen on the trailing side suggests an association with processes like implantation of oxygen ions, radiolysis of ice and fixing noticed in this hemisphere, all correlated with the interactions between the particle radiation trapped in the Jupiter magnetic field and Ganymede's surface, particularly ionic bombardment, which have place preferentially in this portion of the moon. This hypothesis is consistent with the observed oxygen airglow and hydrogen peroxide presence as well as with escape of hydrogen from Ganymede's surface inferred from observations.

Galileo NIMS data indicate also the presence on Ganymede of carbon dioxide CO_2, which appears organized in very small (~ 100 molecules) clusters and widely distributed in very complex patterns. Analyzing in detail its surface distribution that does not show hemispheric asymmetry as oxygen's, it has been found that, in general, bright terrain contains less CO_2 than dark terrain (the detected CO_2 seems to be contained in non-ice materials), there is a little or no CO_2 at the poles (probably masked by polar frost deposits) and dark rays of impact craters are commonly depleted in CO_2 relative to surrounding terrain.

Some terrain inferred to contain larger-grained ice has also higher CO_2 levels while regions with mostly fine-grained ice do not seem to contain it, suggesting that CO_2 distribution is related to endogenous rather than magnetospheric effects. Other molecules species revealed on Ganymede's surface from early analysis of the *Galileo* NIMS IR spectra include sulphur dioxide SO_2 (mainly on trailing hemisphere with a complex spatial distribution), $C \equiv N$ (perhaps as HCN), and CH.

These simple organic molecules may be indigenous or the result of impacts of charged particles from Jupiter magnetosphere on the icy surface of Ganymede or due to

chemical decomposition by solar UV radiation. But the most likely hypothesis is that these elements come from the external layer of asteroids and comets which fell onto Ganymede's surface, that have continued to getting rich in organic materials with time.

The close resemblance of Ganymede's organic materials absorption spectra with those of interstellar ice grains due to CO_2, CN and CH in addition to H_2O, and the wide diffusion of simple organic materials in space, potentially synthesized from carbon-bearing ices by UV irradiation, seem to confirm the provenience of these materials from small rocky bodies like comets and asteroids.

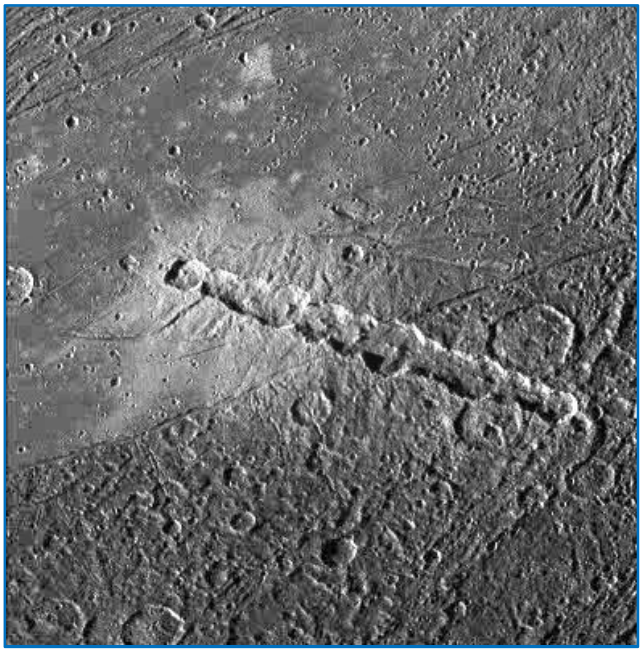

FIGURE 2.18 Succession of the 13 perfectly aligned craters of Enki Catena, on the boundary between Perrine Regio and Sicyon Sulcus [31]

The cometary hypothesis is supported also by the presence on Ganymede's surface of structures as *Enki Catena* (see figure *2.18*), a succession of 13 perfectly aligned and partially superimposed craters probably due to a comet broken in some parts by tidal interaction with Jupiter before hitting Ganymede, an event similar to that interested the *Shoemaker-Levy 9* and Jupiter in *July 1994* [21].

2.6 Surface characteristics

The most interesting properties of Ganymede's surface and regolith to be considered are photometric and thermal ones, which can be estimated respectively with the tools of photometry and radiometry.

2.6.1 Photometric properties

Most photometric studies conducted about Ganymede's surface are based on application of the Hapke's photometric model, a theory for estimating the physical properties of the uppermost regolith of a planetary surface. This approach makes use of a bidirectional reflectance equation, whose terms depend by 6 parameters which relate to the

composition, physical structure and optical properties of the regolith, with the great advantage that they have a sharp physical meaning.
For the aim of this discussion, let considerate only two of them:

- ω_0, the average single-scattering albedo of regolith grains
- θ, a mean slope angle of macroscopic surface relief

The macroscopic roughness parameter θ provides a measure of surface texture at sub-millimetre and larger size scale while single-scattering albedo ω_0 (the probability that a photon survives to the interaction with a single particle) is index of the scattering and absorption efficiency of average regolith grains and is related to their optical constants (such as average particles transparency and albedo), size, size distribution and mechanical structure.

In particular, the directional scattering behaviour is described by a phase function $P(\alpha)$, with phase angle α (the angle between observer, target surface and the sun) for an average regolith grain. Because in various works have been adopted different mathematical forms for $P(\alpha)$, it is most useful to express and compare their phase function results by calculating an effective asymmetry factor g_{eff} (the weighted mean cosine of the scattering angle) whose value can vary from -1 to 1, such that:

- $g_{eff} = 0$ if particles scatter equally well in the forward and backward directions;
- $g_{eff} < 0$ for dominantly backward scattering (relatively opaque) grains;
- $g_{eff} > 0$ for forward scattering (relatively transparent) grains.

For Ganymede have been carried out two types of photometric investigations:

- whole-disk photometric studies, combining spacecraft and Earth-based telescopic observations, to investigate the average global behaviour of the moon;
- disk-resolved photometric studies, from high resolution *Voyager* and *Galileo* observations, that explore the photometric properties of different terrain units, providing information about the scale-dependent spatial heterogeneity of materials deposited on Ganymede's surface and allowing regolith photometric properties to be interpreted in a geological context.

It is important to remind that Hapke's model has an inherent flaw in disk-resolved analysis of Ganymede's regolith materials. Indeed, different types of terrain are assumed to

be photometrically and compositionally homogeneous over size scales from sub-millimetre to tens or hundreds of kilometres [21].

Whole-disk photometry. Ganymede, like all the Galilean satellites, exhibits a global brightness asymmetry correlated to important photometric differences between the leading hemisphere and the trailing one. These differences are mainly in terms of albedo and colour, with the trailing side more reddened and darker (from 10% to 30%) than the leading one, even if the change is much gradual.

The hemispheric asymmetry and particularly the local darkening of Ganymede's surface is generally attributed to the areal distribution of different terrain albedo features on different sides, indicating less non-ice contaminant in the brighter leading side. But more probably it seem to be a consequence of the interactions between charged particles trapped in Jupiter's magnetic field and Ganymede's surface which have place preferentially on the trailing hemisphere.

In particular, the continuous bombardment of surface by magnetospheric ions with an elevate speed leads to exogenic processes like material fixing, radiolysis and sputtering with a global effect of chromatic and photometric changes.

Both *Buratti* in *1995* and *Domingue* and *Verbiscer* in *1997*, sought to identify what surface physical properties might be responsible of leading/trailing hemispheric asymmetry. In both works have been used telescopic observations and broadband *Voyager* data to assign Hapke's model parameters separately to leading-side and trailing-side (values of interest are reported in table *2.2*), but the results have been in contrast.

Indeed, according to *Buratti*, Ganymede's global hemispheric photometric asymmetry was due almost only to albedo variations while, according to *Domingue* and *Verbiscer*, it was the result not only of variations in average particles albedo, but also of significant differences in surface macroscopic roughness, particles compactness and regolith grain transparency.

	Buratti (1995)		Domingue and Verbiscer (1997)	
	leading	*trailing*	*leading*	*trailing*
ω_0	0.82 ± 0.03	0.78 ± 0.03	0.83 ± 0.01	0.87 ± 0.01
θ	–	29° ± 2°	28° ± 3°	35°± 3°
g_{eff}	-0.20 ± 0.04	-0.21 ± 0.04	0.26 ± 0.02	0.04 ± 0.01

TABLE 2.2 Hapke's photometric parameters for Ganymede's leading and trailing hemispheres (0.47 μm) according to Buratti and Domingue and Verbiscer studies [21]

More recently *Helfenstein* and *Shkuratov*, rather than looking for leading-side/trailing-side photometric asymmetries, more interestingly have combined telescopic, *Voyager* and *Galileo* whole-disk data to establish the Hapke's model parameters for Ganymede as a whole and to compare them to those of other planetary objects, particularly Europa and the Moon.

	Ganymede	*Europa*	*Moon*
ω_0	0.76 ± 0.01	0.97	0.28
θ	28° ± 1°	23°	26°
g_{eff}	-0.15 ± 0.01	-0.24	0.16

TABLE 2.3 Hapke parameters assigned for Ganymede, Europa and the Moon (0.47 μm) according to Helfenstein and Shkuratov study [21]

The comparative results reported in table *2.3* indicate that the regolith average particles on Ganymede's surface have:

- an intermediate albedo and transparency between lunar darker regolith and Europa's high albedo grains (according to their geometric albedo);
- a lunar-like macroscopic roughness θ;
- a compactness greater than the Moon's and minor than Europa's, therefore icy grains size are greater than Europa's and minor then Moon's (generally larger on the trailing hemisphere of each body);
- a size distribution broader than the lunar regolith and narrower than Europa's.

In addition to this, the effective asymmetry factor g_{eff} suggests also that particles of Ganymede's regolith are slightly backscattering. These results can be geologically explained with the presence of ice in the regolith of Ganymede and even more in that of Europa, which leads to a concentration and aggregation of soil particles progressively greater than on the dry lunar surface [21].

Disk-resolved photometry. The firsts to perform a disk-resolved photometric study of Ganymede were *Squyres* and *Veverka*, who in *1981* investigated the photometric behaviour of individual geological features on Ganymede using empirical photometric models.

They found that on average, bright terrain is about 20% higher in albedo than the dark one but that the two terrains cannot be uniquely distinguished on the basis of albedo

alone. Indeed, the brightest examples of dark terrain are comparable in albedo to the darkest examples of bright terrain.

Subsequently in *1986 Helfenstein* examined over 90 individual regions of Ganymede's surface and, mainly on the basis of their similarities in albedo, he grouped his observations into six photometric classes of dark terrain, whose single-scattering albedo varied from 0,42 and 0,72, and eight classes of bright terrain, for which ω_0 varied from 0,58 and 0,90, finding, in both cases, the largest values of ω_0 within polar caps.

For both type of terrains, the derived mean values of macroscopic roughness θ varied from less than 1° to about 20° (although for individual regions values as large as 39° were found) with regolith materials dominantly backward scattering, except for polar examples of bright and dark terrains that exhibited significant forward scattering.

About ten years later, *Hillier* used a complete disk-resolved *Voyager* data set to find Hapke's parameters for the different types of Ganymede terrain. He found $\omega_0 = 0.72 \pm 0.02$, $\theta = 28°$ and $g_{eff} = -0.24 \pm 0.02$ for dark terrain and $\omega_0 = 0.80 \pm 0.02$, $\theta = 29°$ and $g_{eff} = -0.19 \pm 0.02$ for bright terrain, confirming that the macroscopic roughness of average dark terrain and average bright terrain is statistically the same and that the average dark terrain regolith is slightly lower in albedo and more opaque than average bright terrain regolith.

Only recently, examining *Galileo* highest resolution data, it has been found that surface materials on Ganymede are highly segregated at size scales of a few kilometres or less with extreme contrast variations which cannot be attributed only to topographic shading but largely to differences in albedo.

In particular, the albedo analysis of dark deposits, easier to carried out because they accumulate on topographically flat areas, has revealed that the darkest materials visible on Ganymede's surface have estimated normal albedo (relative to incidence and emission angles normal to the surface) ranging from 0,12 to 0,34 with a mean of $0,25 \pm 0,04$. This value is comparable to that of dark materials on Callisto's surface and of dark deposits found in valley floors and dark spots on Europa, while it is about five times higher than that of D-type asteroid materials, supposed to be in great amount among surface contaminants.

On the contrary, the photometric properties of high albedo materials are difficult to study and then are more poorly understood than Ganymede's dark materials because relatively pure-appearing exposures of high albedo materials generally occur on surfaces

for which accurate local photometric angles are difficult to measure, like the walls and summits of ridges, troughs and crater walls.

Due to the segregation of dark and bright materials at kilometre and smaller scales, the variations in photometric properties of Ganymede terrains may best be explained by differences in the exposed areal fraction of dark deposits relative to bright ice. If we consider the global albedo map of Ganymede, derived from *Voyager* and *Galileo* data, we can notice that the distribution of normal albedo correspond to an areal abundance of exposed dark deposits ranging from 0 to 94% with a mean of about 60% [21].

2.6.2 Thermal characteristics

According to data from *Voyager* Infrared Interferometer Spectrometer (IRIS) and Galileo Photopolarimeter-Radiometer, Ganymede's surface temperatures run from a maximum peak near $152\ K$ in daylight to a minimum around $70\ \div\ 75\ K$ at night, a range which implies a thermal inertia of about $70\ J/m^2K\sqrt{s}$, very similar to the values for Callisto and Europa.

In particular, surface temperature depends on terrain type: the bright grooved terrain is about $5\ K$ colder during the day than the dark terrain, while during the night the dark/bright terrain temperature contrast reverses, with the bright grooved terrain being about $3\ K$ warmer than the dark terrain.

The mean daytime temperature of the icy component on the leading side has been estimated as $126\ \pm\ 12\ K$ [21].

2.7 Atmosphere and ionosphere

Even if in *1972* a team of astronomers, using Earth-based observations in the visible, claimed that they had detected a thin atmosphere around Ganymede, the first spacecraft investigation for an atmosphere around the moon, conducted in *1979* by *Voyager 1* during a flyby, didn't reveal any evidence of it.

The occultation measurements, effected in the far-ultraviolet and so more sensitive to the presence of gases than those in the visible, yielded a surface pressure of less than $2{,}5 \cdot 10^{-5}\ \mu Bar$ with a particle number density on the surface around $1{,}5 \cdot 10^{9}\ cm^{-3}$.

Despite the *Voyager* data, evidence for a tenuous molecular oxygen atmosphere around Ganymede (very similar to Europa's) was found by the Hubble Space Telescope

(*HST*) in *1995*, observing for the first time airglow of atomic oxygen in the far-ultraviolet, a direct proof of a significant neutral atmosphere composed predominantly of O_2 molecules, because airglow is a consequence of molecular oxygen dissociation by electron impacts.

In particular, the airglow observed over Ganymede is not spatially homogeneous but concentrated in two bright spots located in the northern and southern hemispheres, near $\pm 50°$ latitude, which is exactly the boundary between the open and closed field lines of the ganymedian magnetosphere.

For this reason, spots are probably polar auroras, caused by plasma precipitation along the open field lines. According to telescopic measurements, surface number density probably lies in the $1{,}2 \div 7 \cdot 10^{8}\ cm^{-3}$ range, corresponding to a surface pressure of $0{,}2 \div 1{,}2 \cdot 10^{-5}\ \mu bar$ [13].

2.8 Magnetosphere

During its first encounter with Ganymede, *Galileo* spacecraft discovered that this moon has a permanent intrinsic magnetic moment independent of the Jovian magnetic field, whose value is about $1{,}3 \cdot 10^{13}\ Tm^3$, three times greater than the magnetic moment of Mercury.

The permanent magnetic moment creates a tiny magnetosphere embedded inside that of Jupiter which pervades the part of space around Ganymede within a diameter $4 - 5$ times the radius of the moon ($2631{,}2\ km$).

This magnetic field and has a strength of $719 \pm 2\ nT$ at the equator of the moon (six times the $\sim 120\ nT$ Jovian magnetic field at the distance of Ganymede's orbit) while the intrinsic field strength at the poles is two times that at the equator, about $1438\ nT$. It is modeled with a fixed Ganymede-centered dipole superposed on the ambient Jovian field, tilted with respect to the rotational axis of Ganymede by $176°$ with north pole lying below the orbital plane, therefore it is directed against the Jovian magnetic moment.

According to this model, the magnetic field has a region of closed field lines located below $\pm 50°$ latitude, where charged particles (electrons and ions, particularly atmospheric single ionized oxygen O^+) are trapped, creating a kind of radiation belt, and a region at latitudes higher than $\pm 50°$ corresponding to the polar caps in which magnetic field lines are open connecting Ganymede with Jupiter's ionosphere.

In these areas, have been detected particles with energy until tens or hundreds of keV, responsible for the auroras observed around the ganymedian poles and for the continuous bombardment of the surface which sputters and brightens the ice.

In addition to the intrinsic magnetic moment, variations of the Jovian magnetic field near the moon have confirmed the existence of a Ganymede's induced dipole magnetic field, whose moment is an order of magnitude weaker than the intrinsic one.

The induced component has a strength at the magnetic equator of about $60\ nT$ (half of that of the ambient Jovian field) and is directed radially to or from Jupiter following the direction of the part of the Jovian magnetic field in which Ganymede occurs, that varies with the planet rotation. Moreover, this induced magnetic field is similar to Europa's, indicating that also Ganymede may have a subsurface highly electrical conducting water ocean.

The interaction between the ganymedian magnetosphere and Jovian plasma is for many aspects similar to that of the solar wind and Earth's magnetosphere.

The plasma co-rotating with Jupiter hit the trailing side of Ganymede much like the solar wind impinges on the Earth's magnetosphere, even if for Ganymede the speed of plasma flow is subsonic then there is no shock wave off the trailing hemisphere. Moreover, this magnetic field, like the Earth's, deflects much of the magnetospheric particle flux away from the equatorial surface and low-altitude orbital environment, providing partial protection of this zones from magnetospheric irradiation.

Given that Ganymede is completely differentiated and probably has a metallic iron core, the most reasonable model of generation of the intrinsic magnetic field detected around it is probably similar to the Earth's: it is based on dynamo action or magneto-convection, that is the compositional convection of the high electrical conducting material in a liquid-iron core moving in the interior.

Because of Ganymede's relatively small size, probably the core cannot reach a sufficient temperature to sustain the motion of the fluid iron, then the energy to maintain the observed magnetic field may come from the tidal interactions due to the presence of Jupiter and the Laplace resonance with Europa and Io [13] [16].

2.9 Conclusions and open issues

The diversity and complexity of Ganymede's surface and inferred geological processes make it one of the most intriguing solar system bodies, a moon of planetary stature.

With its mix of dark old and bright young terrain which tell respectively of ancient solar system and terrestrial rifting-like processes, its ancient impact basins and fresh craters, its various landscapes dominated by tectonics, volcanism or slow degradation by space weathering, its intricate internal layering and internal magnetic field, Ganymede serves as the largest and most typical example of icy satellite for understanding the other icy satellites and particularly the Galilean ones.

Moreover, the existence of an internal ocean within Ganymede begs the question of the satellite's potential to harbour life. Ganymede's hypothetic ocean is sandwiched between layers of less and more dense ice phases and is about an order of magnitude deeper than Europa's. Therefore, unlike Europa's ocean, Ganymede's is cut off from any direct supply of nutrients and thermo-chemical energy that might support life and this makes the potential for life in Ganymede's ocean seem small, but the possibility is not ruled out.

Galileo observations have greatly advanced understanding of Ganymede, but many important questions remain mainly in geological field, including [16] [21]:

- *What is the age of dark and grooved terrain, and how extended was their formation period?*
- *Did entrance into the Laplace resonance affect internal evolution, and how is grooved terrain formation linked to it?*
- *Is any part of the surface still geologically active today?*
- *What is the chemistry and biological potential of Ganymede's ocean?*

Imminent future exploration of Ganymede by ***EJSM*** mission will include close flybys but mainly a spacecraft orbiting it, which will permit a long-term, dedicated study of this moon as an integrated system to better understand its surface, interior, magnetosphere and atmosphere. Some goals for future investigations are [16] [21]:

1. *characterize the global and regional distribution and topography of the different geological features;*

2. *determine the composition, distribution and state of ice and non-ice surface components, notably organic materials;*
3. *measure and monitor the magnetic field and plasma over time;*
4. *measure the gravity field to high accuracy to constrain internal structure;*
5. *characterize the neutral atmosphere and ionosphere, particularly in composition.*

CHAPTER 3

Laser Altimetry

In this chapter the principle of operation and main characteristics of a laser altimeter will be analysed and its past and future applications will be described with a special emphasis on its use on *JGO* spacecraft within *EJSM* mission.

3.1 The laser

The word *laser* is the acronym for *Light Amplification* by *Stimulated Emission* of *Radiation*. The distinctive aspects of laser light are [33]:

- *high directionality* that allows to obtain a very narrow low-divergence beam with an high collimation;
- *spatial coherence* meaning that all the photons in a section normal to the beam have the same phase and maintain it in time and space;
- *monochromaticity* because light is emitted with a narrow wavelength spectrum, which depends on the energy released when photons are generated;
- *elevated luminance* represented by the extremely high emitted energy per unit of solid angle or the number of photons per unit of frequency (in other words a great power concentrated in a very little area);
- *ultra-short pulses* derived by the possibility for this light to be gathered in packages of electromagnetic waves very narrow in the domain of time.

According with these characteristics, laser radiation can be thought as a spatial, spectral and eventually temporal concentrated beam of light. Its properties are in strong contrast with those of a traditional light source based on spontaneous emission, which in general emits in all the directions, in an incoherent manner (with a phase that varies randomly with time and position), in a broad spectrum of wavelengths and with a luminance not so high as the laser one. Moreover, non-laser light cannot be collimated by optics as well as that of a laser.

These peculiarities are at the basis of enormous diffusion of laser. Indeed, today it is used in several fields including science, medicine, industry, military defence,

entertainment, information technology and consumer electronics in applications such as optical storage (CD or DVD players), fiber-optic communication, industrial treatments of materials, surgical operations, spectroscopy or illumination.

In particular the possibility to have a rectilinear extremely collimated ray of monochromatic coherent light, with high concentrated power that decreases very slowly with distance, makes laser very interesting and suitable for range-finding devices like altimeters which have to measure infinitesimal variations of speed or shifting projecting light very far from the source [33].

3.1.1 Stimulated emission and population inversion

The physical principle for laser operation can be explained by means the quantum interactions between light and matter.

From atomic physic, we know that in an atom the electrons are forced on quantized orbitals (regions in which there is a high probability to find them) of specific energy level.

When a photon hits the atom, it can be absorbed only if its energy $h\nu$ (where h is the Planck's constant and ν the frequency) is equal to the difference ΔE between two energetic levels: if this happens, electron leaves the so-called *ground level* which has an energy equal to E_1 and reaches another level with higher energy E_2 located farther from the nucleus and known as *excited level*.

The atom is now in an *excited state* but doesn't remain in this state of higher energy for ever because it tends to return to the ground state. Indeed, after a certain time, the excited electron decays into the lower less energetic state: this phenomenon is accompanied by the emission of a photon with frequency ν, energy $h\nu = \Delta E$ and random phase (depending on the atom's internal state) and is known as *spontaneous emission* (refer to figure *3.1*).

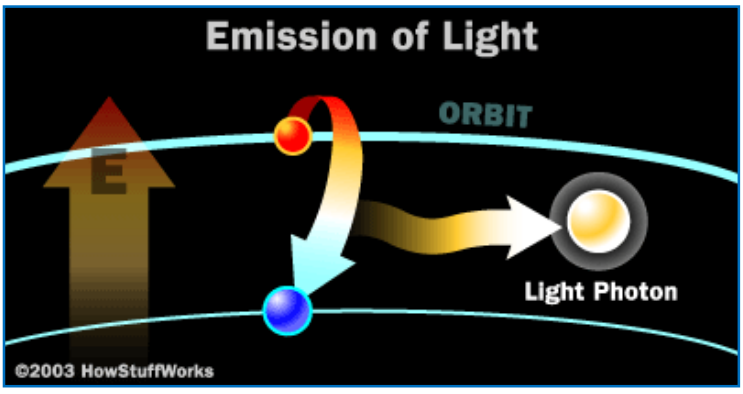

FIGURE 3.1 Representation of spontaneous emission of light [34]

A certain number of atoms in an excited state tend to decay towards the ground state, generating radiation spectrally limited (monochromatic) but with photons not in phase each other (incoherent light) according to the process of *fluorescence*.

If the atom affected by the photon with energy ΔE is already in an excited state, it is carried to the ground state leaving energy that results in the creation of a new photon with the same phase, frequency, polarization and direction of propagation as the perturbing one.

Because the original photon is not absorbed, at the end we have two equal photons. This process (see figure *3.2*), that allows to obtain the amplification of coherent light, is known as *stimulated emission.* It occurs with a rate proportional to the number of atoms in the excited state, the density of photons with frequency ν and a coefficient depending on the particular electronic transition and the particular atom.

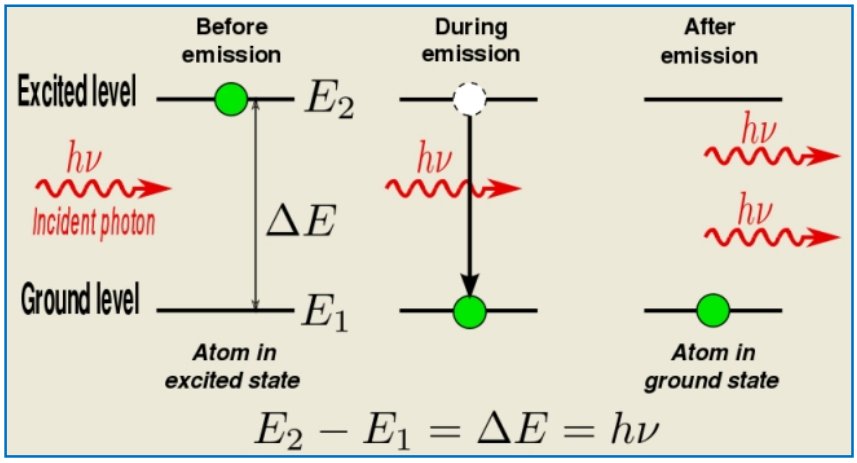

FIGURE 3.2 Representation of stimulated emission [33]

When a photon with an energy equal to the gap between two energetic levels hits an atom, absorption or stimulated emission can occur according to the state in which electrons are. For a given number of incident photons, the probability for one of the two processes happening and its rate, vary with the number of atoms in the ground state N_1 and in the excited state N_2, respectively.

In a condition of equilibrium, we have more non-excited than excited electrons ($N_1 > N_2$) as described by the Boltzmann's distribution [33]:

$$\frac{N_2}{N_1} = exp - \frac{(E_2 - E_1)}{kT}$$

where k is the Boltzmann's constant and T the absolute temperature.

Therefore, in normal conditions, absorption dominates and there is a net attenuation of photons. To produce a laser effect, it is fundamental to increase the probability that a stimulated emission takes place and becomes greater than that of absorption.

In order to realize this condition, firstly it is necessary having an higher number of excited atoms than in the ground state ($N_2 > N_1$); secondly electrons have to remain in the excited state longer than normally (meta-stable state), so that transitions to the lower state occur through stimulated emission and not spontaneously. This condition, that can be achieved only altering the thermodynamic equilibrium of the system with an external source of energy, by means a process known as *population inversion*.

Thanks to it, because the number of new photons generated per unit time by stimulated emission is greater than that of absorbed photons, the light which crosses the material is not dissipated, rather it gains power leading to a *light amplification*, at the basis of laser working [33] [35] [36].

3.1.2 Components and principle of working

Fundamentally, a laser is made up by five components (figure *3.3*) [33]:

1. gain medium (active optic medium);
2. pumping energy;
3. high reflector mirror;
4. output coupler (semi-reflecting mirror);
5. output light beam;

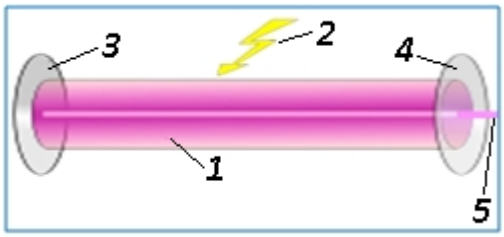

FIGURE 3.3 Laser components [33]

The gain medium is a material in the form of gas, liquid, solid or plasma of controlled purity, size and concentration which has to favourite stimulated emission. It absorbs external pump energy, so that its electrons raise into higher-energy excited state.

Some of these decay soon via spontaneous emission, releasing incoherent light as photons of frequency ν which can excite atoms in ground state or cause stimulated emission colliding with already excited atoms.

When the number of particles in this state exceeds that of particles in the ground state, population inversion is achieved and the amount of stimulated emission due to light that passes through is greater than the amount of absorption. But this is not sufficient to have an optical amplification: the gain medium must to be contained in an optical resonator.

In the simplest form, it is a narrow and long highly reflective cavity (like a tube) with two mirrors at the extremities: one completely reflective and the other only few percent reflective. When a photon from the extern hits an already excited atom of the gain medium, from this interaction a new photon births that has the same frequency and phase and moves in the same direction of the light passes through the medium.

This new photon, which has also the same energy of the original, can interact with an excited atom producing a stimulated emission in it so that, interaction after interaction, photons are multiplied and they move all in the same direction of the perturbing light.

When this light flux bumps into the high reflector mirror, photons are almost totally reflected, so they come back and travel along the cavity in the opposite sense generating other equal photons by stimulating gain medium electrons to make the downward energy jump. With a correctly designed cavity reflecting opportunely resultant photons so that they traverse gain medium atoms more than once, a cascade effect of amplification is produced.

During this backward and forward passage of light in the cavity, a very small percent of it passes through the output semi-reflective mirror and is focalized to make up the external narrow and coherent laser beam.

In this way, light energy, rather than dispersing in space, is concentrated in a very narrow and highly energized beam, whose light is very similar to the input signal in terms of wavelength, phase and polarization (condition necessary for coherence and monochromaticity) [33] [35] [36].

Pumping. The process of supplying the energy required for the stimulated emission to the gain medium is known as ***pumping*** and can occur in different ways: electrical, optical, chemical, nuclear reactions. Obviously, pump power must be higher than a certain threshold representing the minimum energy required to begin laser action [33].

Modes of operation. A laser can operate in two different ways: in a *continuous wave* (*CW*) mode or in a pulsed mode.

In the first case the output is continuous and relatively constant in amplitude with respect to time and population inversion required is continually maintained (the atom returned to the ground state are continuously excited); in the second case, on the contrary, the laser output varies with time, typically taking the form of alternating ‘on’ and ‘off’

periods. Among the techniques for obtaining a pulsed mode of operation, particularly interesting is *Q-switching.*

In a Q-switched laser, the population inversion is allowed to build up by making the cavity conditions (the '*Q*' factor, or *Quality factor*) unfavorable for lasing. Then, when the pump energy stored in the laser medium is at the desired level, the '*Q*' is adjusted (electro- or acousto-optically) to favourable conditions, releasing the pulse. This results in high peak powers as the average power of the laser is packed into a shorter time frame.

The result output from the laser is a short light pulse (tens of nanoseconds in duration) having a very high peak power (the pulse energy divided by its duration) even of many kilowatts [33] [36]. This possibility of operation (to concentrate as much energy as possible at a given place in as short time as possible) it is necessary in rangefinder applications such as altimetry.

3.1.3 Classification

A laser classification is done according to power and then to potential for causing biological damage, defining several classes (*I*, *IA*, *II*, *IIIA*, *IIIB* and *IV*) where *I* is for lower risk, *IV* is for higher risk.

Another important classification is based on the nature of lasing material: gas lasers, chemical lasers organic colorant lasers, metallic vapour lasers, solid state lasers, semiconductor or diode lasers, dye lasers, free-electron lasers. [33] [36].

3.1.4 Nd:YAG laser

Nd:YAG (neodymium-doped yttrium aluminium garnet) laser is a solid-state laser having as active medium a crystal of yttrium and aluminium (yttrium aluminium garnet $Y_3Al_5O_{12}$ or YAG), doped by a triply ionized neodymium (generally present at about 1% in weight), which typically replaces yttrium in the crystal structure of YAG, since their atoms are of similar size.

This kind of laser is optically pumped using flash lamps or laser diodes and, because Nd:YAG absorbs mostly in the bands between $730-760\,nm$ and $790-820\,nm$, krypton flash lamps are usually used. The system has more than two exploitable energetic levels: the most probable transition for stimulated emission corresponds to an emitted light with a wavelength of $1064\,nm$, in the infrared spectrum; however, there are also transitions at 940, 1120, 1320, and $1440\,nm$, but they are less probable.

Additionally, for some applications, infrared light can be frequency doubled or tripled using non linear optical materials to obtain visible green ($532\ nm$) or ultraviolet light. Nd:YAG lasers may operate in both pulsed and continuous mode, but the better performances are reached in the first way particularly with Q-switching.

With this technique output powers of $20\ MW$ and pulse durations of less than $10\ ns$ are achieved with a beam divergence less then $0{,}1\ mrad$. Nd:YAG laser is much important, being one of the most common highly powered laser used in military rangefinder applications and for building laser altimeters [33] [36].

3.2 Laser altimeter

3.2.1 Principle of operation

An altimeter is a rangefinder instrument which enables to measure the distance of a surface from the point of observation (the platform bearing the instrument), thanks to the time of propagation of an electromagnetic wave reflected by the target and captured by the instrument, according to the simple equation:

$$R = \frac{c \cdot \Delta t}{2}$$

where

R is the distance;

c is the velocity of light;

Δt is the propagation time of flight;

2 considers the there and back path.

If the signal is in microwave spectrum, the device is called *radio altimeter*; if wave is emitted in visible-infrared, we speak of *laser altimeter*.

With a laser source, calculation of distance can be performed through two techniques, by measuring or the flight time or interference fringes of the beam.

The first category, surely the most diffuse due to the simplicity of the measurement (speed of propagation of an electromagnetic wave is known with precision), comprises lasers operating both in a continuous mode both in a pulsed way.

In continuous wave devices, gas lasers are typically used and the beam is modulated in amplitude: range measurement is made determining the phase displacement between transmitted and backscattered signal.

Pulsed laser altimeters, instead, are based on the computing of the time of short light pulses for round-trip propagation at the speed-of-light between the spacecraft/aircraft and the surface to be measured. They offer better performances with respect to *CW* lasers, mostly because of typical very high mean powers which can be concentrated in very short pulses [35] [37].

Therefore, pulsed laser altimeters placed on a spacecraft platform are very indicated for high resolution altimetry measurements, like for mapping the topography of planetary surfaces. For this application, they have the great advantage to provide information on the physical structure (slope, roughness, height distribution) and albedo of the target surface in addition to range measures.

This is possible because the interaction of laser footprint with a generic rough or sloping surface, can spread in time and distort the transmitter pulse (see figure *3.4*), so that the backscattered pulse will have a larger width and a different more irregular shape. If a detector observes both transmitted and backscattered laser pulse, several information can be obtained by comparing amplitude and width of the two pulses.

For example, the total area under the received pulse represents the amount of reflected energy, then provides a measure of the surface albedo at laser wavelength. Shape data are taken through an high-speed digital analysis (gigahertz bandwidth digitization) applied to the received pulse waveform (the series of regularly-spaced marks along the base of the received pulse in figure *3.4* indicates the location of waveform digitization samples).

For each pulse, the time interval data, waveform digitizer data and pulse energy data form the basic laser altimeter dataset, from which rms pulse spreading of backscattered pulse is derived, and these data permits to obtain information surface structure.

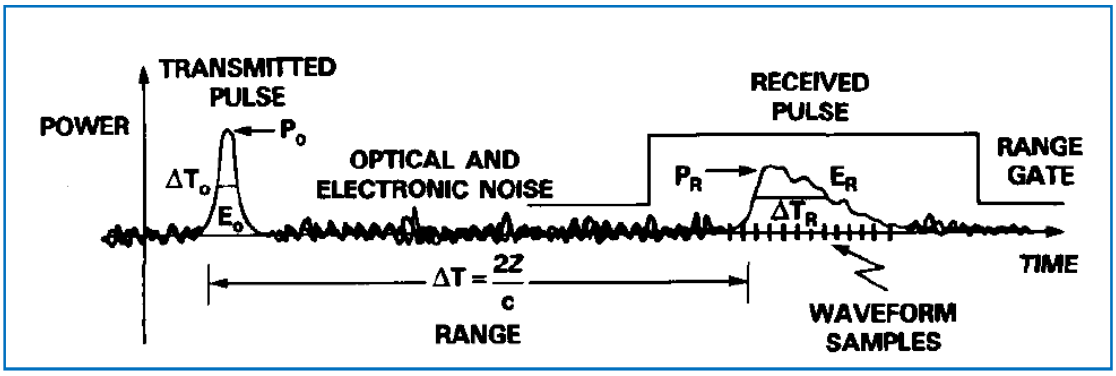

FIGURE 3.4 Waveform and width of laser transmitted and received pulse [37]

Data quality is directly affected by the pulse spreading which, re-distributing the available pulse energy into a broadened waveform (or a larger time interval), acts to reduce the peak-power thus increasing the probability of error for the range measurement and adds timing uncertainty by slowing the rise time of the return signal.

The use of laser as source for transmitting pulses brings many advantages to altimetry with respect to devices using microwaves (radar altimeters). Figure *3.5* illustrates the main differences between laser and radar altimeters (λ is the wavelength of emitted radiation, D is receiver telescope diameter and θ is the beam angular aperture).

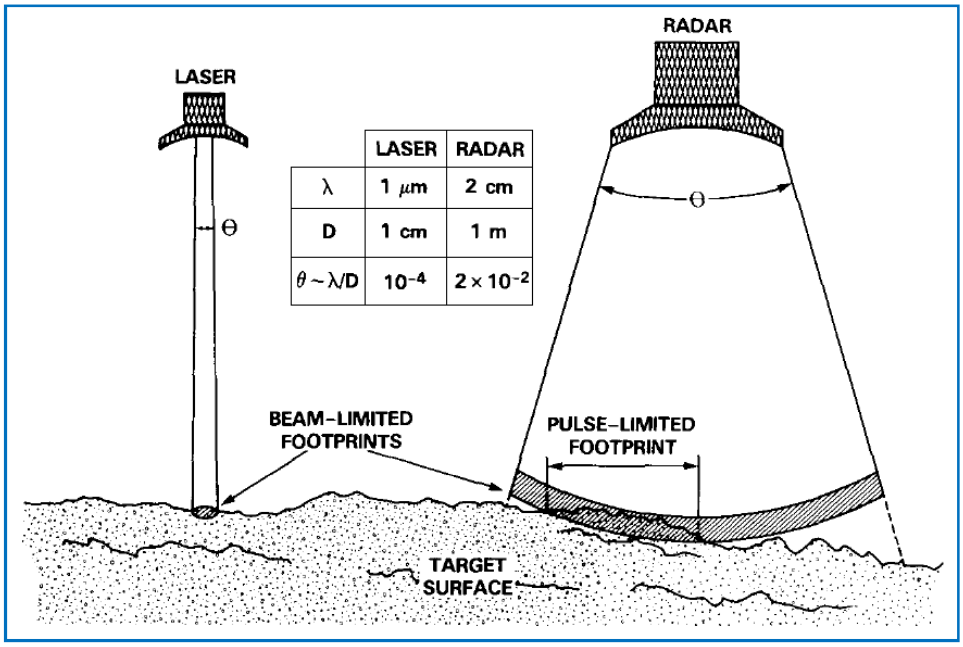

	LASER	RADAR
λ	1 μm	2 cm
D	1 cm	1 m
$\theta \sim \lambda/D$	10^{-4}	2×10^{-2}

FIGURE 3.5 Comparison between laser and radar altimetry [37]

In a first place, the high degree of collimation (sub-milliradian divergence) of a laser beam results, even from orbital altitudes, in a footprint at the surface as small as tens-of-meters in size, orders-of-magnitude smaller than that of a radar altimeter.

Secondly, while in radar altimeters footprint is pulse-limited, due to wavefront curvature and the length of the pulse, in laser altimeters, where milliradian beamwidths are typical and pulse-limited and beam-limited footprints are essentially identical, it is beam-limited. Moreover, for radar nadir is always included in pulse beam-limited footprint, but it is not necessary the leading edge of the backscattered pulse if surface presents a non-zero slope; with laser, instead, emitted pulse can be directed in any directions (eventually along nadir) with extreme precision. Then laser altimeter measurements can provide an high-resolution nadir ground track as complement to the wide survey feature of imaging radar data.

Laser is very suitable for altimetry applications also for being a very bright source of energy. This characteristic results in a stronger backscattered signal easier to detect which leads to a very high-quality measurement for individual pulses. Indeed, contrarily to radar altimetry, no pulse averaging is required for obtaining high-quality data, due to the high signal-to-noise ratio (*SNR*) possible with individual laser pulse reflections. With laser, each pulse produces a unique measurement that defines the vertical and horizontal resolution of the instrument while radar needs more receptions.

To have a significant data set, it is necessary making vertical and horizontal resolution as great as possible.

Laser pulse width and the sampling frequency of altimeter detector electronics (precision with timing is known) determine measurement accuracy in altitude, while laser beam footprint size at the surface (which depends in turn by laser divergence angle and altimeter platform height above the surface) and the spacing between successive laser pulses (function of pulse repetition-rate and platform velocity) influence horizontal resolution.

With present technology (solid-state lasers and nanosecond-resolution timing electronics) it is possible to reach sub-meter vertical range resolutions even from orbital altitudes of hundreds of kilometres. But, for surfaces' topographical measurements it is essential also having an independent knowledge of altimeter platform pointing angle, position and motion. Indeed, variations in laser pointing angle can lead to range biases, while platform vertical motion can be interpreted as topographical variability.

Spacecraft-based altimetry measurements are generally more influenced by uncertainties, even very small, in pointing angle knowledge which, because the enormous

classical orbital distances of $100s$ kilometres, have an obvious effect on the measured altimeter range resulting in very large errors.

Finally, knowledge of horizontal position and of laser footprint size is important for locating the altimeter ground track and relating data between successive tracks over specific target areas [37].

3.2.2 Sub-systems and components

As shown in figure *3.6*, schematically a laser altimeter is made up by [37]:

- a transmitter module (laser oscillator and transmitter optical system);
- a receiver telescope;
- a detector package;
- ranging and waveform electronics;
- a pointing attitude subsystem;
- a computer.

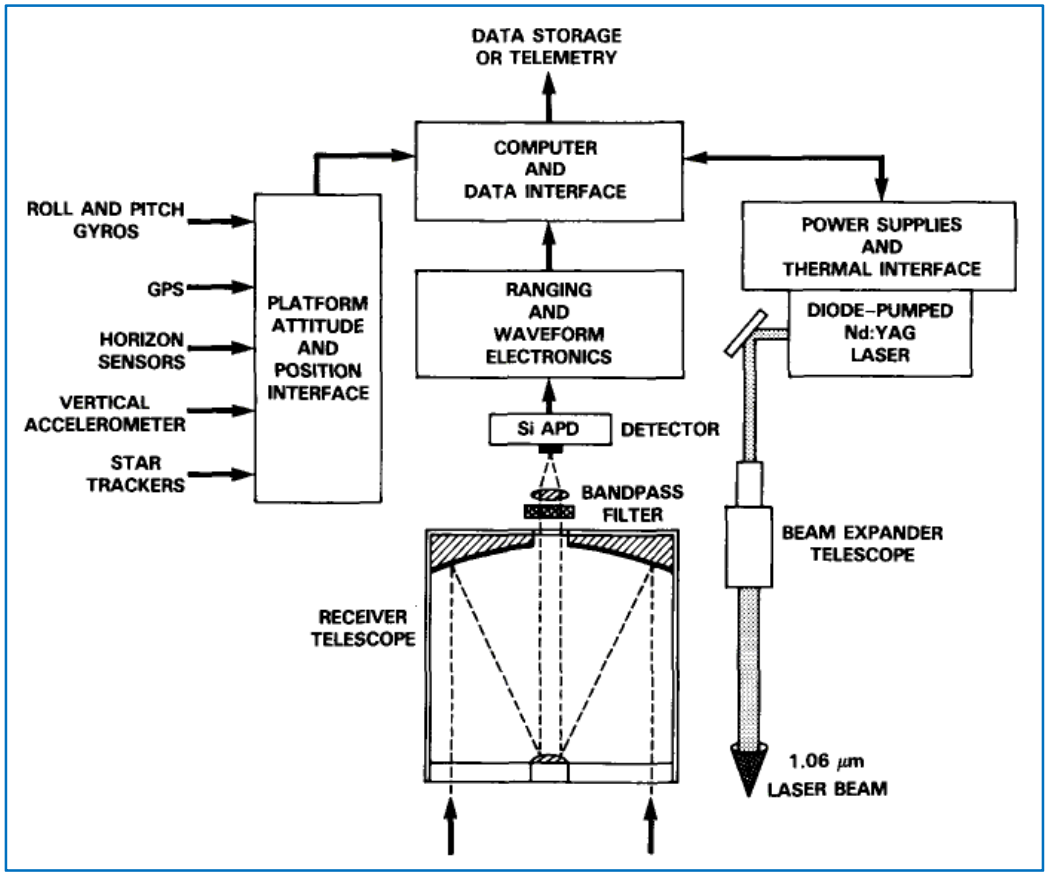

FIGURE 3.6 Laser altimeter subsystems [37]

All these subsystems are packaged into a common structure that provides a rigid platform for the laser transmitter and receiver optical components. Size and weight of the whole system are mostly determined by telescope dimensions, which in turn depend on the particular propagation pathlength to the target surface.

The pulse transmitter is based, at present days, on the relatively new technology of diode-pumped high-power neodymium yttrium aluminum garnet (Nd:YAG) solid-state laser, which can operate both at its fundamental wavelength of $1064\,nm$, that matches with silicon avalanche photodiode (Si APD) detectors, both at the frequency-doubled wavelength of $532\,nm$.

This is the leading laser for airborne-based laser ranging applications, because it offers such efficiency, lifetime, reliability and compactness that are absolutely essential for a spacecraft instrument.

The receiver telescope has the task of collecting photons backscattered from the portion of surface within laser beam footprint, then it is sized to achieve a desired signal collection area for laser radiation. Often its mirrors are designed as on-axis parabolas for having a beam-condenser result. Before reaching detector, condensed beam has to pass through an optical bandpass $2\,nm$ wide filter, centered on the transmitted laser wavelength, in order to reject solar backscatter and other external sources of noise.

Altimeter detector for operations at $1\,\mu m$ is composed by a ***silicon avalanche photodiode*** (***Si APD***) connected to a low-noise pre-amplifier. ***Si APD*** has a sufficient bandwidth ($50 - 100\,MHz$) for short pulse detection. If $532\,nm$ radiation is used, a photon-noise-limited photomultiplier tube (***PMT***) is a more efficient solution. Generally, the field-of-view for the receiver system is set to about $1{,}5 - 2$ times the angular size of the laser beam footprint.

Ranging and waveform electronics is responsible of processing the pulse waveform from the detector to provide measurements of range-to-the-surface, surface reflectance and surface vertical structure of the portion within the footprint.

The analog backscattered pulse in output to the detector passes through a threshold discriminator which enables to minimize the possibility for a false alarm due to the photons which form background noise. Then, it is given in input to a waveform digitizer, which performs an high speed waveform sampling separating pulse amplitude into $50 - 100$ waveform slices, each $1\,ns$ in duration.

This accurate pulse splitting is used to start and stop a time interval counter and to measure pulse energy, power and width for sub-meter-level resolution measurements.

A data interface connects electronic subsystem to the laser altimeter payload computer, whose microprocessor is generally optimized for processing and data transfer with low-powers. Thanks to a master software program, it controls laser emission, reads pulse measurement electronics to acquire altimetrical data and verify its quality, maintains an updated pointing attitude and position and coordinates the sequence of operations of instrument components through various loops.

Finally, a pointing-attitude subsystem provides an absolute attitude estimate for a precise knowledge of the angular offset from nadir. For space-based laser altimeters, which have the most stringent requirements on pointing attitude knowledge due to the high altitudes above the target surface, a full-performance system is necessary. With modern technologies, even a $5\ arcsec\ rms$ attitude determination is possible [37].

3.3 Past, present and future applications for laser altimeter

3.3.1 Laser altimeters used in past missions

In contrast to other remote-sensing devices, the first application of a laser altimeter was for spacecraft observations. In *1971-72* the missions *APOLLO 15*, *16* and *17* in lunar orbit by *NASA* demonstrated the feasibility for laser altimetry, thanks to successful operations of the first space-based laser remote-sensing instrument.

Particularly with *APOLLO 17*, laser ranging data were acquired at a very successful rate of 99% for the 4000 foreseen laser pulses, resulting in altimetrical profiles and high resolution regional contour maps of lunar surface. Even if only a limited region of terrain was sampled and laser transmitters were short-lived, *APOLLO* altimeters matched their primary purpose of giving ranges for photographs with a precision of about $4\ m$. They used solid-state flash-lamp-pumped Q-switched ruby lasers, in which pulse width was controlled mechanically and flashlamp exciters required $16 - 32\ s$ to recharge.

From then, very important progresses in laser altimetry have been done. Indeed, the solid-state diode-pumped laser technology has allowed to reduce notably size, weight and power of space-based laser altimeters with respect to *APOLLO* missions, improving, at the same time, performances and lifetime even of several orders of magnitude.

In *1994*, the first diode-pumped Nd:YAG laser altimeter flew on board of *Clementine* (a joint mission of *NASA* and the *Ballistic Missile Defence Organization*) within the *Laser Image Detection And Ranging* (*LIDAR*) experiment, with the task of measuring the distance from the spacecraft to a point on the surface of the Moon.

During two and a half months, *Clementine* obtained useful *LIDAR* data demonstrating the feasibility for space-based altimetry of this new efficient technology for the transmitter (see table *3.1* for details) and of silicon avalanche photodiode as detector and providing altimetric maps that allowed to identify the morphology of large basins and other lunar features.

The instrument had a total mass of about $2{,}37\ kg$ with an average power of $6{,}8\ W$. An opportunely set threshold enabled the best compromise between missed detections and false alarms. Each measurement took a second; vertical resolution was $40\ m$ while the horizontal one about $100\ m$. Two problems affected *Clementine* performances: the orientation of the laser transmitter was uncertain (pointing was nominally at spacecraft nadir but the amount of offset was not known at the time of analysis) and the signal-to-noise ratio very low.

Just a year later, *Shuttle Laser Altimeters SLA-01* and *SLA-02*, demonstrated the effectiveness of orbital laser altimeters for terrestrial geodesy, representing at the same time an important in-space test for future space laser altimeter sensors.

In particular, *SLA-01* was the first of four planned flights to precisely measure the distance to the Earth's surface from the Space Shuttle, while *SLA-02* had the task of determine the shape of land surfaces and vegetation canopies. Eighty hours of data were acquired along the nadir track of the Space Shuttle, with $100\ m$ diameter footprints. *SLA-02* was the first laser altimeter to globally sample virtually all terrain and landcover classes on planet Earth.

The successive spacecraft with a laser altimeter among its scientific instruments was *NASA Mars Global Surveyor* (*MGS*) that in *September 1997* reached the red planet. Its laser altimeter *MOLA* (*Mars Orbiter Laser Altimeter*), developed following *Clementine* experience but optimized for planetary mapping, mapped the topography of Mars to unprecedented accuracy and studied the $1064\ nm$ surface reflectivity of the planet.

For these purposes, in addition to the laser-pulse time-of-flight measurement, the instrument also measured the transmitted and the backscattered laser pulse energies and the echo pulse width at the threshold crossings. The threshold was fixed and the use of four

parallel low-pass filters (globally 2 nm bandwidth) maximised the probability of detection under all conditions. *MOLA* was fully calibrated, then it was possible an unbiased comparison of measurements from different altitudes, laser output and atmospheric conditions. Thanks to a timing resolution of 2,5 ns and a clock frequency of about 100 MHz, the system could measure changes in the height of the Martian surface with decimetre precision.

In *February 2000*, the *NEAR Laser Rangefinder* (*NLR*) was used on board of the *Near Earth Asteroid Rendezvous* (*NEAR*) spacecraft for making highly accurate measurements of the shape and surface structure of the asteroid *433 Eros*, one of the most interesting near-Earth asteroids, in order to provide information about the origin and nature of these bodies.

NLR was the first spaceborne laser altimeter to have a continuous in-flight range self-calibration performed by a single-mode fused silica optical fiber, which allowed to have high quality data permitting an evaluation of the instrument functionality throughout the mission [38].

MOLA, *NLR* and the laser altimeter of *Clementine* have represented the birth of a new class of active remote-sensing instruments for conducting scientific investigations in the solar system. They were all based on Nd:YAG laser operating at 1064 nm and a silicon avalanche photodiode. Table *3.1* gives some parameters of the three laser altimeters.

parameters	Clementine	MOLA	NLR
Pulse energy (*mJ*)	171	42	15,6
Pulse width (*ns*)	10	8	15
Laser beam divergence (*μrad*)	500	370	235
Pulse repetition frequency (*Hz*)	1	10	1/8 – 1 – 2 – 8
Receiver telescope diameter (*cm*)	13,1	50	7,62
Receiver telescope FOV (*μrad*)	4	0,85	3
Orbit height nominal range (*km*)	500 (max 640)	400	160 (max 327)
Range resolution (*m*)	40	0,3	0,32
Instrument mass (*kg*)	2,37	26,2	4,9
Instrument power consumption (*W*)	6,8	28	15,1

TABLE 3.1 Main parameters of laser altimeters used in past missions [39]

3.3.2 Laser altimeters for present and future missions

The next laser altimeter to visit a planet will be the *Mercury Laser Altimeter* (*MLA*) on board of *MESSENGER* (*MErcury Surface, Space, ENvironment, GEochemistry and Ranging*), a spacecraft of *NASA Discovery Program* launched in *August 2004* with the objective of analysing the planet Mercury for a better understanding of how terrestrial planets formed and evolved.

MLA will start its observations in *2011* measuring the topography of the Mercury's northern hemisphere with a range resolution of $15\,cm$ to provide an high-precision topographic map of the polar region and main characteristics of the long-wavelength topographic features of the mid-to-low latitudes.

The instrument has been designed on the heritage of *MOLA* technology incorporating peculiar thermal features because of the particular conditions of an orbit around Mercury. On the whole, it is a quarter the size and mass ($7{,}3\,kg$) of *MOLA* and has a power consumption of just $23\,W$ [40].

Afterwards in *September 2007*, the *Japanese Space Agency* (*JAXA*) have successfully launched lunar orbiter *SELENE* (*SELenological and ENgineering Explorer*), a mission with the primary objective of global surveying of the Moon and for developing critical technologies for future lunar exploration.

Spacecraft instrumentation comprises also the laser altimeter *LALT* with the task of mapping the Moon's topography with a vertical resolution of better than $5\,m$ and a $1{,}6\,km$ spatial resolution. Round trip time is measured by a $150\,MHz$ clock, giving timed one-way distance within $1\,m$. This mission foresees to collect about 30 million of data points from a ranging distance of 50 to $150\,km$ [41].

The *Lunar Laser Ranging Instrument* (*LLRI*) is the laser altimeter designed by the *Indian Space Research Organization* (*ISRO*) for *Chandrayaan-1* mission, started in *October 2008* for orbiting the Moon over a two year period with the goal of returning scientific information of the lunar surface. *LLRI* has been designed to obtain a Moon's global topographical map with a resolution of $10\,m$ from polar orbit [42].

For *April 2009* it is foreseen the launch of the first spacecraft of *NASA Robotic Lunar Exploration Program* called *Lunar Reconnaissance Orbiter* (*LRO*), whose objective is to map the Moon's surface, in particular to characterize landing sites in order to facilitate the return of humans on the Moon and for in-situ resource utilization.

The *Lunar Orbiter Laser Altimeter* (*LOLA*) will enable to produce an high-resolution ($1\,m$ vertical and $50\,m$ horizontal accuracy) global topographical map and a geodetic framework, used for precise targeting but also to detect surface ice inside permanently shadowed craters near the poles. *LOLA* would perform over 4 billion measurements over the course of the mission with a time-of-flight accuracy of $0{,}6\,ns$ corresponding to a $10\ cm$ precision [43].

The first European laser altimeter, developed by *ESA* as payload for topographic missions, will fly on board *Mercury Planetary Orbiter* (*MPO*) within *BepiColombo* mission, whose launch is planned for *2014*. The *BEpiColombo Laser Altimeter* (*BELA*) has been designed to provide a global topographic grid of Mercury with an height accuracy of $1\,m$ but it will be used also for ranging experiments for determining, together with gravity measurements, Mercury's obliquity, librations and tidal deformation. The whole instrument has a mass of $8{,}5\ kg$ and absorbs about $37\ W$ [44].

3.3.3 Laser Altimeter for *JGO*: science goals, performance requirements and data sheet

Within the ambit of *EJSM* (see *chapter I*), laser altimeter on board of *JGO* spacecraft will contribute to the geodetic and geophysical characterization of Ganymede and particularly of its surface, but the accurate range data, combined with additional information, will be essential also for studies of the spacecraft orbit in the gravity field of the moon. It will be possible to reconstruct topographic profiles along the ground track of the spacecraft and also to characterize tidal forces effect by measuring the temporal changes in the global shape of Ganymede due to them.

In particular, scientific objectives that make so important the use of this instrument are [45] [46]:

- derive geo-referenced topographic profiles and 3D models of geological features and different terrain types (regionally and locally);
- derive an accurate Ganymede's global shape model and reference figure;
- derive a geodetic network based on accurately measured positions of prominent topographic features;
- determine tidal deformation (tidal amplitudes as a function of Ganymede's orbital longitude);
- measure topography to interpret the gravity signal (possible mass anomalies);

- assist in studies of geodetic parameters (coordinate system, rotation, librations);
- assist in orbit determination and gravity data modeling;
- measure surface roughness, local slopes and albedo variations.

For this purposes, there are some performance requirements that have to be satisfied with reference to the $200\ km$ circular orbit foreseen for the *Ganymede Science Phase* [45]:

- high signal-to-noise ratio for reliable pulse detections during night and day from a typical range of $200\ km$ (single shot pulse detection > 95%);
- range accuracy of $1\ m$;
- laser footprint of $20\ m$ from an altitude of $200\ km$;
- lifetime of 1 year;
- allow for surface roughness modeling (pulse shape modeling).

For instrument design, *EJSM* science team will refer to the laser altimeter planned for *BepiColombo* mission (*BELA*) in the environment of Jovian system.

In addition to this traditional system Laser Altimeter *LA* (*BELA* like), it is being studied the development of a next generation of laser altimeter (Micro Laser Altimeter, *MLA*), which is based on a compact microchip laser firing at kHz and a silicon *APD* as detector operating in a single photon-counting mode or "Geiger mode" (it detects even the arrival of just one returned photon requiring at least five photons for high detection probability).

This new system, already operational for terrestrial airborne applications, would have size, mass and power requirements dramatically reduced over a traditional laser ranging system. As of this writing the single photon detection technology for space applications is at a very preliminary study at *DLR* (*German Aerospace Center*) and at our best knowledge no scientific results about performance of this innovative space photon detector are available in literature.

Laser emitter of Laser Altimeter for *JGO* would have, preferably, an adjustable pulse output energy for allowing operations at Callisto, which has an albedo (0,19) much less than Ganymede's, and for giving much options for power efficient laser operations at Ganymede.

The pointing shall be accurate to within the size of the laser footprint and both nighttime and daytime observations are equally possible (in the second case it is fundamental to overcome the solar background noise).

The instrument should also be capable for two-way offline range measurements to terrestrial laser stations for alignment calibration, performance tests and also for clock calibration and distance measurements which will support the tracking of the spacecraft and gravity field modeling.

In scenario in which *JGO* will operate, laser altimeter will not find limitations due to the presence of an atmosphere (like in terrestrial applications), which attenuates backscattered power for absorption. Moreover, because of the highly radiative environment which *JGO* will encounter, a critical issue for the instrument is surely its limit to radiation tolerance and in particular the knowledge of least tolerant components.

Elements like receiver diode, laser pump diodes, laser rod, Q-switch, optical coatings for example are rad-hard only up to $60 - 100\ krad$ (according to the value of radiation dose foreseen for the mission).

Table *3.2* reports the most important parameters of laser altimeter designed for *EJSM* mission comparing *MLA*/*LA* solutions while table *3.3* makes a comparison in terms of mass and power budget between *MLA* and *BELA* [45] [46].

PARAMETER	UNIT	MICRO LASER ALTIMETER (*MLA*)	LASER ALTIMETER (*LA* classic case)
TRANSMITTER			
laser wavelength	nm	532 or 1064	532 or 1064
laser pulse energy	mJ	1,2	50
pulse duration	ns	3,4	3,4
pulse-repetition rate	Hz	175	10
beam divergence angle	mrad	0,02	0,2
RECEIVER			
field-of-view (twice the laser spot size)	deg (mrad)	0,0115 (0,2)	0,0115 (0,2)
aperture	mm	20	250
focal length	mm	1250	1250
number of filters	#		5
filter centered wavelength	nm	532 or 1064	532 or 1064
filter bandwidth	nm	1	1
types of optics		cassegrain or galilean telescope (receiver and transmitter)	cassegrain (receiver) and beam expander (transmitter)

DETECTOR			
type of detector		Si APD as single photon counting detector in Geiger mode	Si APD
pixel lines in array	#	1	1
pixels per array line	#	1	1
pixel size	μm	100	100
repeat time	msec	< 1	100
operating temperature	°C	from -10 to +10	from -10 to +10
A/D convertion	bit/pix	1	10
readout time	msec	< 1	1
SWATH AND RESOLUTION			
swath width (laser footprint from 200 km)	km	0,002	0,02
range accuracy	m	1	1
spatial pixel resolution	m	2	20
GENERAL			
mass	kg	~3	~10
size	cm	23 x 16 x 14	emitter box 10 x 10 x 30; receiver optics
power (incl. efficiency loss)	W	~25	50
TRL	#	3	6
heritage		terrestrial airborne applications, LAPE study for ESA	Bepi Colombo Laser Altimeter (BELA)
useful range	km	200 (up to 400)	
preferred location		nadir-pointing	nadir-pointing
operating temperature	°C	from -30 to + 50	from -30 to + 50
detection probability	%	95	
probability of false alarm	%		
lifetime	year	1	
data volume (total)	Gbyte	> 2,5	> 2,5
data rate (instantaneous)	kbyte/s	60	30

TABLE 3.2 Main parameters for JGO laser altimeter (comparison between MLA and LA) [45] [46]

Power Budget (W)	MLA	BELA
laser	8	8
rangefinder incl. detector	6	9
data processing	4	4
secondary power	18	21
primary power from spacecraft	25	30
Mass Budget (kg)	MLA	BELA
laser head	1	1,5
laser electronics	0,9	2
receiver telescope, electronics	0,5	1,1
electronic box (Power, DPU)	1,2	1,4
sum	3,6	6

TABLE 3.3 Comparison for mass and power budget between MLA and BELA [46]

CHAPTER 4

Orbital propagator and laser altimeter performance model

In this chapter it will be introduced the orbital propagator and the laser altimeter performance model developed in *MatLab* environment.

We will refer to the scenario of *EJSM* mission and in particular to the laser altimeter designed to fly on *JGO* in orbit around Ganymede.

Schematically the software is organized in the following conceptual macro-blocks:

- *Orbital data input, check and time conversion* in which the user inserts the orbital parameters, initial and final dates and the step of temporal variation. This block verifies the correct introduction of inputs and provides the conversion from Gregorian to Julian date (see paragraph *4.1.1* and *4.2* for details);
- *Orbital propagation* which allows to know the position and the velocity of the spacecraft in a particular reference system in a given instant of time;
- *Search in Ganymede's virtual map* which returns the topographical features of the portion of Ganymede's surface visited by the spacecraft;
- *Performance model* which computes all the quantities describing laser altimeter performances;
- *Plot* which enables to graphic all the desired results.

Although the program primary purpose is to study the instrument performance, the orbital propagator and the virtual map assume a fundamental role.

The performance model analyzes the laser altimeter performance taking in account parameters like spacecraft altitude, slope, roughness and albedo of terrain but not depending of mission time.

In this way, the performance simulation could foresee also conditions very far from those which the instrument actually will encounter during the mission and the results could provide just an idea of the effective performance which can be obtained; moreover, it is impossible to create temporal profiles of performance with the effort of the orbital propagator.

With the addition of an orbital propagator and a map of the surface characteristics, these limits can be overcome getting to a great improvement in the reliability of the results. Given an orbit, the orbital propagator allows to know the position of the spacecraft in every instant of time during all the mission and, consequently, the point on the surface lit up by the laser thanks to a geographic map linked to the propagator. The virtual map of Ganymede contains physical and topographical properties of all the different zones of the surface as albedo, roughness and slope.

These information of the map are inputs for the performance model, which derives the instrument performances in every instant of time for area of the surface flown over by the spacecraft.

Collecting these data in a set interval of time, we can obtain temporal profiles of instrument performance with the indication of latitude and longitude of the surface visited.

4.1 Orbital propagator introductive concepts

4.1.1 Definition of time

The concept of time for astronomical observations and astrodynamics measurements is essential, mostly when it is necessary to know the precise position of a celestial body or a spacecraft in a particular instant of time. For these applications, instead to assume the *second* as unit of measurement, for counting time it is preferred to refer to the *day*, being this quantity strictly linked to the repetitive phenomenon of Earth's rotation about its axis.

In particular, it is defined a *sidereal day* and a *solar day*. In the first case the *day* is the interval between two successive passages of the Vernal equinox across the meridian of an observer on Earth's surface; in the second case it is the interval between two successive passages of the Sun's direction across the observer's meridian and represents day and night alternation.

The solar day is at the basis of the nowadays most diffuse calendar in the world known as *Gregorian Calendar* based on the specification of a date through year, month and day. Time is completely specified with the addition of hour, minute and second of the local time with respect to the Greenwich meridian [47].

For astronomical or orbital applications, it is more convenient to use the so-called *Julian Date*, that is a progressive counting of days from a reference date fixed to the $12{:}00{:}00$ of $1\,January\,4713\,BC$ (the year of the first documented astronomical

observation). In this way, the time is expressed by a single number representing days, therefore years and months are incorporated as multiples and hours, minutes and second makes the fractional part. According to the convention, integer numbers correspond to the noon of Greenwich meridian, while Julian dates ending with .5 indicate the midnight [48].

In order to avoid the use of very large numbers due to the several millenniums past from zero Julian date, each fifty years the number of past days is updated and the counting is referred to a date closer to the present time known as *reference epoch*. In these years, the reference epoch called $J2000$ is the $12:00:00$ of $1\ January\ 2000$ which corresponds to $2451545{,}0$ days expressed with Julian date.

Then the counting of time will be referred to this epoch and successively transformed in Julian date [47] [48].

4.1.2 Reference coordinate systems

In order to individuate the position of the satellite in a precise instant of time, it is necessary to define opportune reference coordinate systems. For our purposes, we have to introduce three reference frames, all with origins in the centre of Ganymede: a *perifocal frame*, an *inertial frame* and a *planetocentric frame*.

Perifocal coordinate system. For this Cartesian system the fundamental plane is the plane of the spacecraft's orbit. The x_ω-axis, which points towards the periapsis and the y_ω-axis, rotated of *90°* in orbital motion direction, lie in the fundamental plane, while z_ω-axis, normal to the orbital plane, is oriented to complete a right-handed system. The versors associated with these axis are respectively *p*, *q* and *w*. This frame is particularly useful for describing and computing the motion of the satellite along the orbit [49].

Inertial coordinate system. In this case the axis are indicated with *x*, *y* and *z* with *x* and *y* lying on Ganymede's equator (reference plane) and *z* coinciding with the rotational axis of the moon. The *x*-axis direction is given by the ascending node of the Ganymede's equatorial plane on the Earth equatorial plane (coinciding with Celestial equator), while the *y*-axis is defined to complete the right-handed Cartesian tern.

The unit vectors associated with *x*, *y* and *z* are indicated respectively with *I*, *J* and *K*. This frame is important for an absolute knowledge of satellite's position and to link it with latitude and longitude of the corresponding point on Ganymede's surface [47] [50].

With the help of *SPICE kernel files* by *NASA* [51], it is possible to relate the position of these axis with those of the *Earth Mean Equator* and *Equinox* of *Epoch J2000* inertial reference system ($EME2000$) [50], a right-handed Cartesian set of three orthogonal axis with origin in the centre of the Earth, z_E-axis normal to the Earth mean equator at $J2000$, x_E-axis parallel to the Vernal Equinox of the Earth mean orbit at $J2000$ and y_E-axis to complete the right-handed system. This definition, using mean quantities at $J2000$, allows to exclude the effects of equinox precession interesting the Earth. From *SPICE kernel file* relative to *Galileo* mission, we deduce the right ascension α and the declination δ in $EME2000$ of the north pole of Ganymede at a generic instant of time [51]:

$$\alpha = 268{,}20° - 0{,}009 \cdot T$$
$$\delta = 64{,}57° + 0{,}003 \cdot T$$

where T is the centuries past from $J2000$. The multiplied coefficients of T take in account the effects due to the equinox precession of Ganymede. With α and δ the position of rotational axis is individuated and then the reference plane is normal to this axis.
In this way the inertial Ganymede-centred inertial system is fully defined.

Planetocentric coordinate system. This spherical frame is used to locate a point on the surface of Ganymede through the specification of two angles: the *longitude* φ (the angle between the prime meridian and the projection in the equatorial plane of the vector individuating the point) measured towards East in the sense of rotation and comprised between $0°$ and $360°$, and the *latitude* λ (the angle between the vector individuating the point and the equator) ranging from $0°$ at the equator and $90°$ at the poles and considered positive for the northern hemisphere and negative for the southern one [47]. The third coordinate is fixed and equal to the main radius of Ganymede, which we suppose spherical, being the difference between equatorial and polar radius very small [51].

Obviously we need a reference point from which starting the counting of longitude, that is the intersection between the prime meridian and the equator. In particular, because this reference system rotates together with Ganymede, in order to locate this point at a certain time it is necessary to know the prime meridian position at a reference time and its angular velocity. From *SPICE kernel file*, we find that the position of Ganymede's prime meridian at a particular time is [51]:

$$PM = PM_{J2000} + PM_{rate} \cdot d = 44{,}04° + 50{,}3176081 \cdot d$$

where PM_{J2000} is the position at $J2000$ (the angle on the equator between the *x*-axis of inertial frame and the prime meridian in the verse of rotation), PM_{rate} is the angular displacement in a terrestrial day, d represents the days past from $J2000$ and PM is the position at the time indicated with d (geometrical interpretation in analogous to that of PM_{J2000}) [50].

The knowledge of the satellite position and of prime meridian location, both in the inertial frame, allows to locate the point on the surface which is pointed by the satellite.

4.1.3 Description of an orbit through orbital parameters

An orbit is unequivocally determined through the specification of five independent parameters called *orbital elements*, which define trajectory's size, shape and orientation in space. A further quantity is used to specify the position of the satellite along the orbit at a particular time. Then, the classical set of six orbital parameters is composed by (see figure *4.1*) [49]:

- *semi-major axis* $\boldsymbol{a}$ defining the size of the orbit (for elliptical orbits is the semi-distance between periapsis and apoapsis);
- *eccentricity* $\boldsymbol{e}$ defining the shape of the orbit (0 for circular orbits, from 0 to 1 for elliptical ones);
- *inclination* $\boldsymbol{i}$ defining the orientation of the orbit with respect to the central body's equator. In particular, it is the angle between the *z*-axis of inertial frame and the z_ω-axis of perifocal frame (it is defined from 0° to 180°);
- *right ascension of the ascending node* $\boldsymbol{\Omega}$ defining the location of nodes (the points where the satellite crosses through the central body's equator) with respect to inertial frame. In particular, it is the angle between the ascending node (the node crossed in a northerly direction) and the *x*-axis of inertial frame measured on central body's equator in the direction of *y*-axis (it can varies between 0° and 360°);
- *argument of periapsis* $\boldsymbol{\omega}$ defining the location of periapsis with respect to the central body's equator. In particular, it is the angle between the direction of periapsis and the ascending node measured in the orbital plane in the direction of satellite's motion (it is defined between 0° and 360°);
- *true anomaly* $\boldsymbol{\nu}$ defining where the satellite is within the orbit with respect to periapsis. In particular, it is the angle between the periapsis direction and the vector

identifying the satellite's current position measured in the orbital plane in the direction of orbital motion (it varies between 0° and 360° during an orbit).

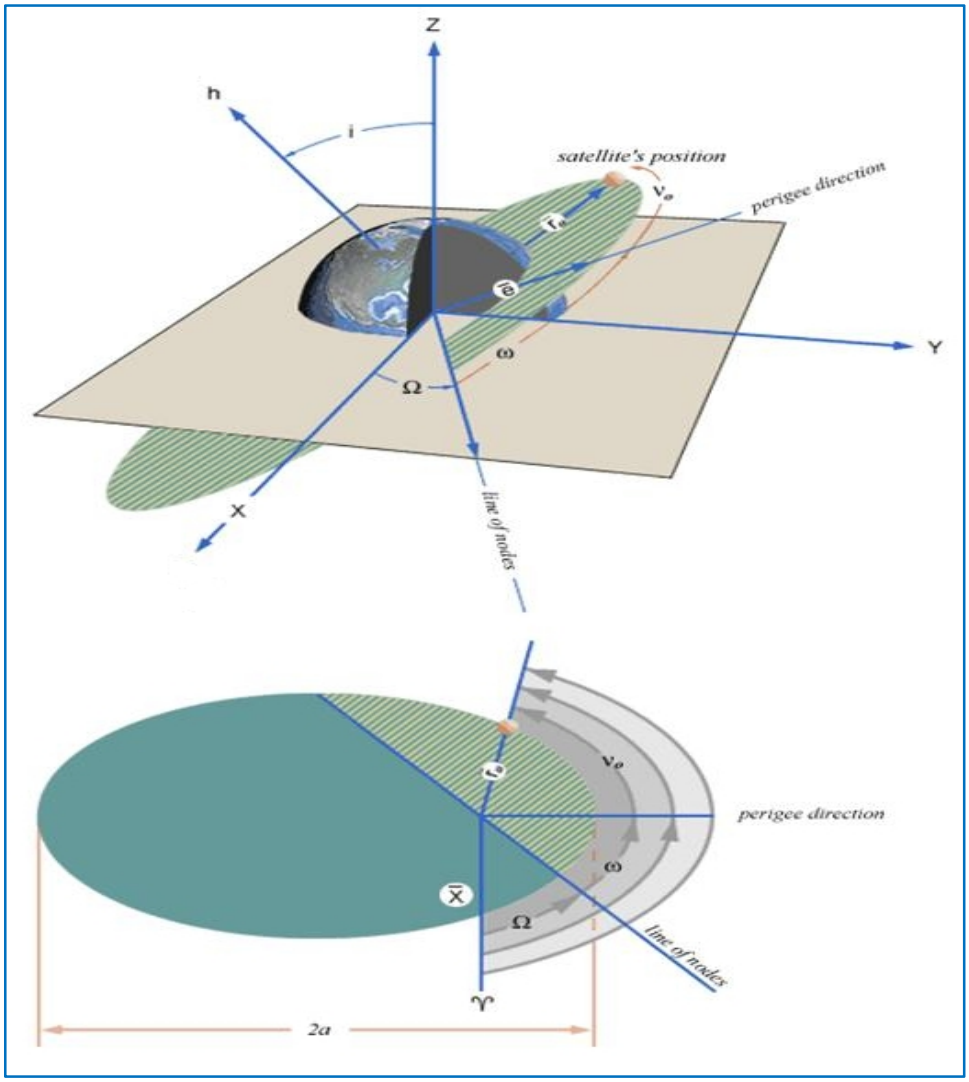

FIGURE 4.1 Definition of an orbit through orbital parameters and coordinate systems representation [52]

4.2 Data input, check and time conversion

The parameters in input to the software are the orbital elements, the indication of the initial and final instant of propagation, the position of the spacecraft on the orbit at the initial time and the variation in time between two successive computation.
In details, input data are the following:

- *maximum altitude* $\boldsymbol{H_{MAX}}$ [*km*], the greatest height of the orbit or, analogously, of the spacecraft above the surface;
- *minimum altitude* $\boldsymbol{H_{MIN}}$ [*km*], the lowest height of the orbit, or, analogously, of the spacecraft above the surface;
- *inclination* $\boldsymbol{i}$ [°] of the orbit with respect to Ganymede's equatorial plane;
- *right ascension of the ascending node* $\boldsymbol{\Omega}$ [°] of the orbit with respect to the *x*-axis of Ganymede-centred inertial frame;
- *argument of periapsis* $\boldsymbol{\omega}$ [°] of the orbit with respect to the ascending node;
- *initial true anomaly* $\boldsymbol{\nu_0}$ [°], the location of the spacecraft along the orbit with respect to periapsis at the initial date;
- *initial date* $\boldsymbol{T_{in}}$, the time for starting propagation in terms of year, month, day, hour, minute and second;
- *final date* $\boldsymbol{T_{fin}}$, the time for ending propagation in terms of year, month, day, hour, minute and second;
- *step of propagation* $\boldsymbol{\Delta t}$ [*s*], the increment of time in the range time of interval $T_{fin} - T_{in}$.

In addition to that, the user can also choose if consider an ideal Keplerian orbit or a perturbed one, taking into account the J_2 effects due to the non-sphericity of Ganymede (see paragraph *4.3* for details).

As preliminary step, the software controls the correct insertion of inputs and, eventually, will inform the user if some data has been wrongly inserted, situation which can lead to a bad-working and, consequently, to non-acceptable results.

In particular, checks are done on the sign and on the absolute values of the orbital parameters, the extreme of the altitudes and on the initial and final dates. In the last case it is verified that the values for year, month, day, hour, minute and second are integer and comprised in the respective interval of validity considering also the different number of

days for the different months and the addition of a day at the end of February for leap years.

If date is expressed in Gregorian, the temporal increment cannot be applied, being the time representation cyclic and not progressive. For this reason, before starting propagation computing, it is necessary to convert initial and final dates into Julian dates.

This is performed by a software code which, for both dates, counts the number of years, months and days (excluded the present date, which is not concluded) from the reference epoch $J2000$ taking in account the fraction of day constituted by hours, minutes and seconds.

Successively these numbers are transformed in Julian dates referred to the zero date (t_{in} and t_{fin}) adding $2451544{,}5$ which corresponds to the midnight and not to the noon of $1\ January\ 2000$ (this is more practical for conversion because today the beginning of a day is fixed at midnight).

At this point, all the quantities necessary to computing are available and propagation can start.

4.3 Orbital propagation

4.3.1 Overview

An orbital propagator, as previously said, is an algorithm that allows to calculate the position and the velocity of a spacecraft, moving along a known orbit, after a certain time t starting from given initial conditions (figure *4.2*).

From the knowledge of the orbit (H_{MIN}, H_{MAX}, i, Ω and ω) and the spacecraft's position on it (ν_0) at the initial time t_{in}, the propagation algorithm returns the position and velocity vectors ($\bar{r}$ and $\bar{v}$), the true anomaly ν and the altitude H at the instant t together with the longitude φ and latitude λ of the point of surface the spacecraft is pointing (along nadir-direction).

Since the scope is to analyze temporal profiles of laser altimeter performance during all the mission, the outputs of the orbital propagator will be provided for a series of successive times, obtained discretizing the interval of time between initial and final dates T_{in} and T_{fin} with a step equal to Δt.

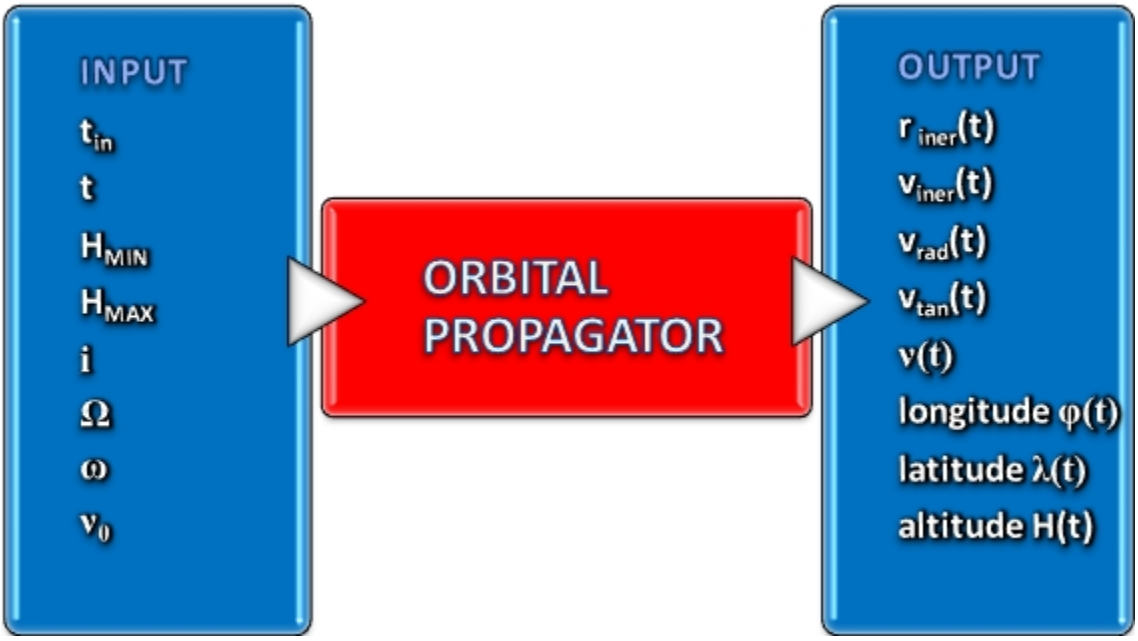

FIGURE 4.2 Input-output block diagram of the orbital propagator

The number of temporal samples to be taken (how many times the algorithm has to be implemented) is equal to:

$$N_{samples} = \frac{t_{fin} - t_{in}}{\Delta t} + 1$$

where t_{in} and t_{fin} represent initial and final Julian dates, respectively, reported in seconds.

Then, for each iteration, in input to the propagator the initial instant of time remains constant and equal to t_{in} while the final instant t is updated increasing time of Δt. In particular, the current final time t_i of i-iteration can be calculated according to the following relation:

$$t_i = t_{in} + (i - 1)\Delta t$$

It has to be noted that for the first iteration t_i coincides with t_{in}.

4.3.2 Algorithm of propagation

As shown in figure *4.3*, the algorithm at the basis of the orbital propagator can be split in several conceptual units. Inputs and outputs of each of them are reported respectively on the left and on the right; their algorithms will be explained separately in the following sections.

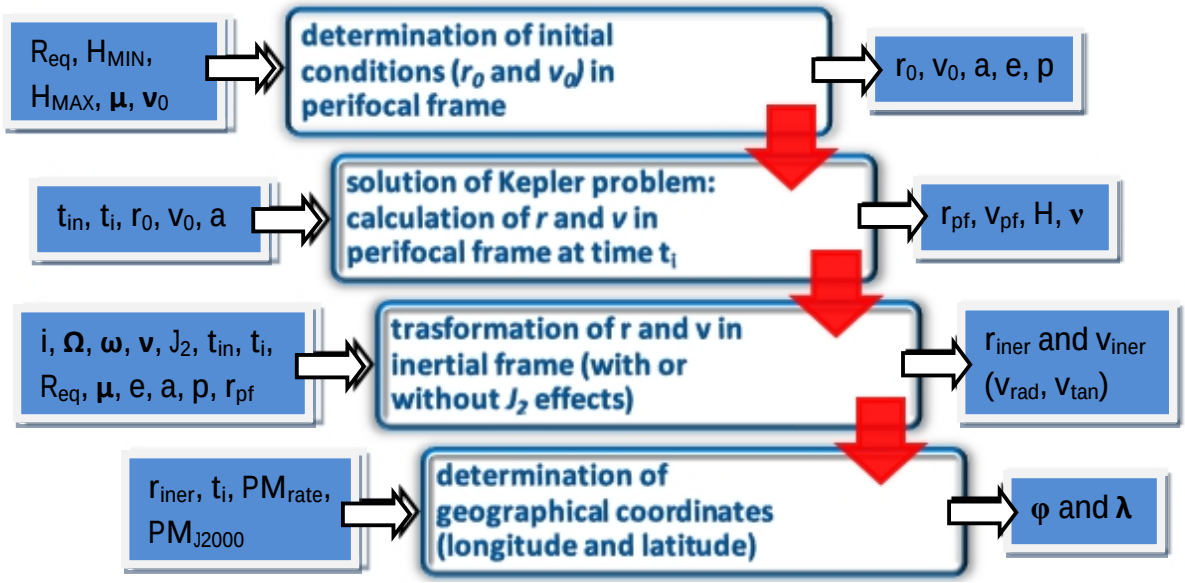

FIGURE 4.3 Block diagram of orbital propagator algorithm parts with respective inputs (on the left) and outputs (on the right)

Determination of initial conditions ($\bar{r}_0$ and $\bar{v}_0$). As first step the physical characteristics of the central body (Ganymede) have to be introduced. For our aims, it is sufficient to define the mean radius R_{eq} of the sphere (coinciding to the equatorial one), the planetocentric constant μ (equal to GM, where G is the universal gravitational constant and M the Ganymede's mass) and the quadrupole term of gravitational momentum J_2 (we consider only this disturbing term). According to table *2.1*, we have:

$$R_{eq} = 2631{,}2\ km$$

$$\mu = 9887{,}834\ \frac{km^3}{s^2}$$

$$J_2 = 126{,}9 \cdot 10^{-6}$$

The first two parameters are used, together with H_{MIN}, H_{MAX} and ν_0, to obtain some features of the orbit necessary to deduce the initial position vector $\bar{r}_0$ and the initial velocity vector $\bar{v}_0$; J_2, instead, together with i, Ω and ω, is fundamental to report spacecraft's position and velocity from perifocal to inertial frame.

The remaining two orbital elements a and e and the parameter p called semi-latus rectum (the half of the chord to the conic orthogonal to the major axis and passing through the focus) can be calculated as follows [49]:

$$a = R_{eq} + \frac{H_{MIN} + H_{MAX}}{2}$$

$$e = \frac{H_{MAX} - H_{MIN}}{H_{MIN} + H_{MAX} + 2R_{eq}}$$

$$p = a(1 - e^2)$$

Then, considering the equation describing the orbit in a polar plane [49]

$$r = \frac{p}{1 + e \cdot \cos \nu}$$

it is possible to compute the module of the position vector in perifocal system at initial time r_0 setting $\nu = \nu_0$ and, finally, in the same frame the initial position vector and initial velocity vector as follows [49]:

$$\bar{r}_0 = r_0 \cdot \cos \nu_0 + r_0 \cdot \sin \nu_0$$

$$\bar{v}_0 = -\sqrt{\frac{\mu}{p}} \sin \nu_0 + \sqrt{\frac{\mu}{p}} (e + \cos \nu_0)$$

In addition, we can derive also the orbital period OP and the radius of periapsis r_{per} and apoapsis r_{apo} [49]:

$$OP = 2\pi \sqrt{\frac{a^3}{\mu}}$$

$$r_{per} = a(1 - e) \qquad r_{apo} = a(1 + e)$$

Calculation of r and v in perifocal frame ($\bar{r}_{pf}$ and $\bar{v}_{pf}$). The core of the orbital propagator is the solution of the so-called *Kepler problem* of orbit determination as function of time for two bodies under the action of gravitational forces. In other words, to predict the future position and velocity ($\bar{r}(t)$ and $\bar{v}(t)$) of the orbiting object as a function of some known initial position and velocity ($\bar{r}_0$ and $\bar{v}_0$) and the time-of-flight.

The approach by Kepler to the problem (today known as *classical formulation*) foresaw to derive time-of-flight equations analytically, using only the dynamical equation of motion and integral calculus. This method was based on geometrical argumentations which led to the concept of eccentric anomaly and nowadays it has only an historical value not only because it is valid just for elliptical orbits but also because it doesn't work very well when the eccentricity in nearly 1 (high losses for numerical accuracy and a too slow or missed convergence for the trial-and-error solution).

For overcoming these defects, it is better to refer to one of the most recent advances in the field of orbital mechanics: a ***universal formulation*** based on a different variable, whose introduction allows to develop a single time-of-flight equation valid for all conic orbits. This approach is strongly recommended as the best method for general use and is at the basis of our orbital propagator [49].

Before describing its implementation in the software, it is necessary to frame the problem and deduce some fundamental relations.

From the orbital mechanics it is note that the energy associated with an orbit can be written as [49]:

$$\varepsilon = \frac{1}{2}v^2 - \frac{\mu}{r} = -\frac{\mu}{2a}$$

If we resolve v into its radial component $\dot{r}$ and its transverse component $r\dot{v}$ and consider the equation for the angular momentum

$$h = r^2\dot{v} = \sqrt{\mu p} \quad \Rightarrow \quad (r\dot{v})^2 = \frac{\mu p}{r^2}$$

we can solve the equation of the energy for $\dot{r}^2$ obtaining:

$$\dot{r}^2 = \frac{2\mu}{r} - \frac{\mu}{a} - \frac{\mu p}{r^2} \tag{4.3.1}$$

This is the differential equation for knowing the position as function of time. Because it is not obvious, a new independent variable X is introduced, defined as follows [49]:

$$\dot{X} = \frac{\sqrt{\mu}}{r} \tag{4.3.2}$$

Now, combining *equation* (*4.3.1)* and (*4.3.2)*, introducing the eccentricity e and integrating through variable separation, we obtain the following relationship between r and X:

$$r = a\left(1 + e\sin\frac{X + C_0}{\sqrt{a}}\right) \tag{4.3.3}$$

Moreover, substituting it into *equation* (*4.3.2)*, we deduce also a relation between t and X:

$$\sqrt{\mu}t = aX - ae\sqrt{a}\left(\cos\frac{X + C_0}{\sqrt{a}} - \cos\frac{C_0}{\sqrt{a}}\right) \tag{4.3.4}$$

where C_0 is the constant of integration and it has been assumed $X = 0$ at $t = 0$.

So far, equations for both r and t in terms of X have been developed. Differentiating *equation* (*4.3.3)*, applying the initial conditions and using trigonometric relations, we get [49]:

$$\sqrt{\mu}t = a\left(X - \sqrt{a}\sin\frac{X}{\sqrt{a}}\right) + \frac{\bar{r}_0 \cdot \bar{v}_0}{\sqrt{\mu}}a\left(1 - \cos\frac{X}{\sqrt{a}}\right) + r_0\sqrt{a}\sin\frac{X}{\sqrt{a}} \tag{4.3.5}$$

$$r = a + a\left[\frac{\bar{r}_0 \cdot \bar{v}_0}{\sqrt{\mu a}}\sin\frac{X}{\sqrt{a}} + \left(\frac{r_0}{a} - 1\right)\cos\frac{X}{\sqrt{a}}\right] \tag{4.3.6}$$

To simplify, let us introduce an auxiliary variable Z [49]

$$Z = \frac{X^2}{a} \quad \Rightarrow \quad a = \frac{X^2}{Z} \tag{4.3.7}$$

and let replace this positions in *equation* (*4.3.5)* and (*4.3.6)*. In particular, defining the coefficient C and S functions of Z as [49]

$$C(Z) = \frac{1 - \cos\sqrt{Z}}{Z} = \frac{1 - \cosh\sqrt{-Z}}{Z} = \frac{1}{2!} - \frac{Z}{4!} + \frac{Z^2}{6!} - \frac{Z^3}{8!} + \cdots \tag{4.3.8}$$

$$S(Z) = \frac{\sqrt{Z} - \sin\sqrt{Z}}{\sqrt{Z^3}} = \frac{\sinh\sqrt{-Z} - \sqrt{-Z}}{\sqrt{(-Z)^3}} = \frac{1}{3!} - \frac{Z}{5!} + \frac{Z^2}{7!} - \frac{Z^3}{9!} + \cdots \tag{4.3.9}$$

we obtain [49]:

$$\sqrt{\mu}t = SX^3 + \frac{\bar{r}_0 \cdot \bar{v}_0}{\sqrt{\mu}}CX^2 + r_0X(1 - CZ) \tag{4.3.10}$$

$$r = CX^2 + \frac{\bar{r}_0 \cdot \bar{v}_0}{\sqrt{\mu}}X(1 - SZ) + r_0(1 - CZ) \tag{4.3.11}$$

Given the generic instant t_i, from *equation (4.3.10)* X is estimated and replaced in *equation (4.3.11)*. This process allows to calculate r module.

But, since *equation (4.3.10)* is transcendental in X, a trial-and-error solution is indicated: starting from an initial value of first tentative for X, its value will be

continuously updated until the convergence is reached, that is when the time corresponding to X is equal (within a certain tolerance) to t_i. The algorithm for doing that used in the software is based on the *Newton-Raphson* method applied to *equation (4.3.10)*.

The first step is to initialize the variable X, fixing for it an initial value according to the type of orbit. Based on the semi-major axis, we have [49]:

$$a \geq 0 \qquad X = \frac{(t_i - t_{in})}{a}\sqrt{\mu}$$

$$a < 0 \qquad X = sign(t_i - t_{in})\sqrt{-a} \cdot ln\left(\frac{-2\mu(t_i - t_{in})}{a\left[\bar{r}_0 \cdot \bar{v}_0 + sign(t_i - t_{in})\sqrt{-\mu a}\left(1 - \frac{r_0}{a}\right)\right]}\right)$$

In the case of parabolic orbit, for which conventionally $a = 0$, the first relation presents a singularity which can be eliminated simply replacing a with $1/\alpha$ where α is equal to [49]:

$$\alpha = \frac{1}{a} = \frac{\frac{2\mu}{r_0} - v_0^2}{\mu}$$

Got X, we can estimate Z and then the coefficients C and S according to *equation (4.3.8)* and *(4.3.9)*. In the case $Z = 0$ it is used the series development for C and S for removing the singularities in the formulas.

At this point, from the knowledge of $\bar{r}_0$ and $\bar{v}_0$, it is deduced the value of time t corresponding to that of X according to *equation (4.3.10)*:

$$t = t_{in} + \frac{r_0}{\sqrt{\mu}}X + \frac{\bar{r}_0 \cdot \bar{v}_0}{\mu}CX^2 + \left(1 - \frac{r_0}{a}\right)\frac{S}{\sqrt{\mu}}X^3$$

where *equation (4.3.7)* has been used to eliminate Z and t has been replaced with $t - t_{in}$ being the initial instant different from 0. The value obtained is then compared to t_i and, if their difference is greater than the chosen tolerance (set on 10^{-4}), the value of X is re-calculated according to the *Newton-Raphson* method as:

$$X_{new} = X_{old} + \frac{(t_i - t)}{\left.\frac{dt}{dX}\right|_{X=X_{old}}}$$

where the term at denominator is equal to [49]

$$\frac{dt}{dX} = \left[\frac{r_0}{\sqrt{\mu}}(1 - CZ) + \frac{\bar{r}_0 \cdot \bar{v}_0}{\mu}(1 - SZ)X + \frac{C}{\sqrt{\mu}}X^2\right]$$

relation obtained combining ***equation (4.3.11)*** with the definition of X (***equation (4.3.2)***).

With this new value for universal variable X the values of Z, C, S and consequently t are updated. The new obtained value of time is then compared with t_i and, if the difference is always greater than the tolerance, the loop restarts leading to another value of t. When the convergence is reached ($t_i - t$ falls within the tolerance) iterations stop and we have the definitive values for X, Z, C and S. Knowing them, $\bar{r}_{pf}$ and $\bar{v}_{pf}$ can be evaluated in terms of $\bar{r}_0$, $\bar{v}_0$ and some other quantities depending on X. Indeed, considering that Keplerian motion is confined to a plane, the four vectors are coplanar then we can express both $\bar{r}_{pf}$ and $\bar{v}_{pf}$ as a linear combination of $\bar{r}_0$ and $\bar{v}_0$ [49]:

$$\bar{r}_{pf} = f\bar{r}_0 + g\bar{v}_0$$
$$\bar{v}_{pf} = \dot{f}\bar{r}_0 + \dot{g}\bar{v}_0$$

where the second relation has been obtained differentiating the first. The four scalar quantities f, g, $\dot{f}$ and $\dot{g}$ are function of time and are not independent being [49]:

$$f\dot{g} - \dot{f}g = 1$$

Developing expressions for f and g in terms of perifocal coordinates and relating these coordinates with X, we obtain [49]:

$$f = 1 - \frac{CX^2}{r_0} \quad ; \quad g = t - t_{in} - \frac{SX^3}{\sqrt{\mu}}$$

Moreover, differentiating, in a similar manner we have [49]

$$\dot{f} = \frac{\sqrt{\mu}X}{r_{pf}r_0}(SZ - 1) \quad ; \quad \dot{g} = 1 - \frac{CX^2}{r_{pf}}$$

By means the described method, we have obtained two relations in which the position and the velocity of the spacecraft are expressed as functions of time and of the initial conditions. In particular the temporal dependence is given by the coefficients f, g, $\dot{f}$ and $\dot{g}$, which depend also by X. Varying these four scalars with respect of the time, the position and velocity are different.

The advantage of this method over others are that only one set of equations works for all conic orbits (circular, elliptical, parabolic and hyperbolic ones) and accuracy and convergence for nearly parabolic orbits is improved.

It has to be noted that, because the oblateness effects don't change form and size of the orbit but just its orientation in space, this treatment is independent from this perturbation, which influences only the resulting vectors in the fixed inertial frame.

Got $\bar{r}_{pf}$, the true anomaly can be computed simply as the angle between the position vector and its component along the periapsis direction (coinciding with versor p) [49]:

$$\nu = \cos^{-1}\left(\frac{r_{pf\_p}}{r_{pf}}\right)$$

Obviously, if the position vector has a negative component along the direction of versor q, the true anomaly is major than $180°$, then the value of ν from the formulas has to be replaced with $360° - \nu$.

Finally, the altitude of the spacecraft with respect to the surface is simply the difference between the modulus of the position vector and the mean radius of Ganymede.

Transformation of r and v in inertial frame ($\bar{r}_{iner}$ and $\bar{v}_{iner}$). To transform the position and velocity vectors from the perifocal frame to the inertial one, it is sufficient pre-multiplying $\bar{r}_{pf}$ and $\bar{v}_{pf}$ for a rotation matrix T, whose terms are functions of the three Euler's angles of the orbit indicating how the perifocal frame is oriented in space with respect to the inertial one. Indeed, this matrix elements depend on the orbital parameters i, Ω and ω, which, as mentioned above, represent the orientation of the orbit in the inertial coordinate system. The matrix T is equal to [49]:

$$T = \begin{bmatrix} \cos\Omega\cos\omega - \sin\Omega\sin\omega\cos i & -\cos\Omega\sin\omega - \sin\Omega\cos\omega\cos i & \sin\Omega\sin i \\ \sin\Omega\cos\omega + \cos\Omega\sin\omega\cos i & -\sin\Omega\sin\omega + \cos\Omega\cos\omega\cos i & -\cos\Omega\sin i \\ \sin\omega\sin i & \cos\omega\sin i & \cos i \end{bmatrix}$$

while the position and velocity vectors in the inertial frame are [49]

$$\bar{r}_{iner} = T \cdot \bar{r}_{pf}$$
$$\bar{v}_{iner} = T \cdot \bar{v}_{pf}$$

In the evaluation of T, the oblateness effects play a fundamental role because they produce a variation with time in the angles Ω and ω, that is they change the orbit's

orientation in space incrementing the time of propagation. In particular the angular rates of variation (expressed as degrees per second) for these two parameters are [49]:

$$\dot{M} = \sqrt{\frac{\mu}{a^3}}\left[1 + \frac{3}{2}J_2 R_{eq}^2 \frac{\sqrt{1-e^2}}{p^2}\left(1 - \frac{3}{2}\sin^2 i\right)\right]$$

$$\dot{\Omega} = -\frac{3}{2}J_2 \frac{R_{eq}^2}{p^2}\dot{M}\cos i \quad ; \quad \dot{\omega} = \frac{3}{2}J_2 \frac{R_{eq}^2}{p^2}\dot{M}\left(2 - \frac{5}{2}\sin^2 i\right)$$

where the quantity $\dot{M}$ represents the rate of variation of the mean anomaly (the fraction of orbital period past from the last passage of the satellite at the periapsis expressed as an angle).

If J_2 effects are considered, at the time t_i we will have a right ascension of the ascending node and an argument of periapsis different from those at t_{in}: this phenomena are known, respectively, as *precession of the line of nodes* and *precession of the periapsis*. In this way, changing Ω and ω, change also the terms of the matrix T. In particular, the new values for these angles at time t_i are:

$$\Omega_{new} = \Omega_{old} + \dot{\Omega}(t_i - t_{in}) \quad ; \quad \omega_{new} = \omega_{old} + \dot{\omega}(t_i - t_{in})$$

with the term within the round brackets representing the seconds past from the initial instant of propagation.

From the knowledge of $\bar{v}_{iner}$ we can also calculate the radial and tangential velocities [49]:

$$v_{rad} = e\sin\nu\sqrt{\frac{\mu}{a(1-e^2)}} \quad ; \quad v_{tan} = \sqrt{v_{iner}^2 - v_{rad}^2}$$

while the velocities at the periapsis and the apoapsis are [49]

$$v_{per} = \sqrt{\frac{\mu}{a}}\sqrt{\frac{1+e}{1-e}} \quad ; \quad v_{apo} = \sqrt{\frac{\mu}{a}}\sqrt{\frac{1-e}{1+e}}$$

Determination of geographical coordinates (φ and λ). Obtained the position vector in the inertial frame, we need to relate this reference system with the rotating planetocentric one in order to find the geographical coordinates of the point on the surface individuated by $\bar{r}_{iner}$.

To do that, let's calculate the angle θ between the projection of $\bar{r}_{iner}$ in the equatorial plane and its component along the *x*-axis, and the angle ψ formed by the vector itself and its equatorial projection. They represent, respectively, the angular distance of the point on the surface projected in the equatorial plane from the *x*-axis of the inertial frame (reference direction) and the angular distance of the same point from the equator, and they can be evaluated as follows:

$$\theta = \cos^{-1}\left(\frac{r_{iner\_x}}{\sqrt{r_{iner\_x}^2 + r_{iner\_y}^2}}\right)$$

$$\psi = \cos^{-1}\left(\frac{\sqrt{r_{iner\_x}^2 + r_{iner\_y}^2}}{r_{iner}}\right)$$

To remove singularities, if the component along the *y*-axis of the position vector is negative, the value of θ from the formula is replaced with $360° - \theta$. Moreover, if the component along *z*-axis of $\bar{r}_{iner}$ is negative, following the usual convention, the value of ψ is considered negative.

As we can notice, these angles have a strong relation with the concepts of longitude and latitude, according to their meaning. Indeed, while the latitude is simply equal to ψ, for the longitude it is necessary just to refer the position of the *Prime Meridian* at the current time to the *x*-axis and consider the angular difference between this reference and the position individuated by θ. In particular, the angular position of the *Prime Meridian* with respect to the *x*-axis, measured in the sense of rotation of Ganymede (from West to East), at the time t_i is given by [see *paragraph 4.1.2* within *"Planetocentric coordinate system"*]:

$$PM = PM_{J2000} + PM_{rate} \cdot d = 44{,}04° + 50{,}3176081 \cdot d$$

where d, the days past to the reference epoch $J2000$, is equal to:

$$d = \frac{t_i}{86400} - 2451544{,}5$$

being t_i expressed in seconds.

Then, longitude φ and latitude λ are simply [49]:

$$\varphi = \theta - PM$$
$$\lambda = \psi$$

where φ, always positive and measured toward East, runs from $0°$ to $360°$, while λ, comprised between $0°$ and $90°$, is positive for the northern hemisphere and negative for the southern one.

All the data in output to the orbital propagator for different times are collected, for simplicity, in a $N_{samples}\ x\ 8$ matrix called *"data"* in which the different quantities are organized in columns. In particular the first column contains the times samples considered (expressed in days past to the initial instant); the second and the third, respectively the corresponding longitude and latitude; the fourth the altitude; the fifth, the sixth and the seventh the values of the velocities in the inertial frame (respectively total, radial and tangential); the eighth, finally, the true anomaly. In symbols:

$$data = [d_{from\ t_{in}} \quad \varphi \quad \lambda \quad H \quad v_{tot} \quad v_{rad} \quad v_{tan} \quad \nu]$$

4.4 Search in Ganymede's virtual map

The knowledge of the current values of longitude and latitude allows to individuate, in each instant of time, the precise point of Ganymede's surface pointed by the laser altimeter along the nadir-direction. The software provides a map of the surface and it is possible to obtain a characterization of the lit-up area in terms of albedo, slope and roughness, fundamental quantities for a performance analysis of the instrument.

Schematically, the software reads the geographical coordinates from the orbital propagator and returns the corresponding values of albedo, slope and roughness from a virtual map. The map has been created referring to the information reported in *chapter 2*.

Slope and roughness. As mentioned before, as of this writing, data about the slope and roughness distribution on the Ganymede surface are not available in literature. For slope, it is just available the range of variation assumed ($0° \div 20°$); therefore data will be parameterized in this range.

Regard the roughness, we refer to the works of *Gardner* [53] and *Harding* [54] which report tables with the rms values of roughness corresponding to several types of

terrestrial terrains: we consider the terrestrial values of the structures which have geomorphic characteristics similar to those expected on Ganymede surface. In particular roughness is:

- for *polar caps* 0,3 m for an occurrence frequency of 50% and 1,0 m for a frequency of 90%;
- for *normal-faulted rift graben* structures 1,2 m for an occurrence frequency of 50% and 4,7 m for a frequency of 90%.

For a better characterization of Ganymede surface, we set a mean value of roughness for low-to-mid latitudes zones (prevalently tectonized with rift, graben and faults) and one for high latitudes polar zones (covered by polar caps):

- for polar regions, which extends over latitudes major than $\pm 60°$, we choose a value of 1,0 m considering that these areas are quite totally covered by ice caps;
- for low-to-mid latitudes areas, where tectonics structures are more common in bright grooved terrains and they cover about $2/3$ of Ganymede surface (see *chapter 2*), we decide to use the mean value in the range 1,2 m – 4,7 m, that is 3 m.

Albedo. As described in *chapter 2*, Ganymede is characterized by strong variations in albedo for different types of terrain: dark and bright terrains can be distinguished. According to data available in literature, for dark terrains the albedo range is from 0,12 (the darkest area of surface) to 0,34 with a medium value of 0,25. For bright terrains, at our best knowledge no data are available in literature. We extrapolate the need information considering that:

- the Ganymede's mean albedo is 0,43;
- the surface presents about 35% of dark terrains and 65% of bright terrains.

In particular, making a medium for albedo of terrains weighted with their occurrence on the surface, we can calculate the mean value of albedo for bright terrains a_{bm} as:

$$0{,}25 \cdot 0{,}35 + a_{bm} \cdot 0{,}65 = 0{,}43 \Rightarrow a_{bm} = 0{,}53$$

Now, considering that the albedo of the darkest bright terrain is similar to the albedo of the brightest dark terrain, we can assume $0{,}34$ as the inferior extreme of the albedo range for bright terrains. Then, the superior extreme of the interval a_{bs} will be:

$$\frac{0{,}34 + a_{bs}}{2} = 0{,}53 \Rightarrow a_{bs} = 0{,}72$$

In this way, we have a range for albedo of $0{,}12 \div 0{,}34$ (with a mean of $0{,}25$) for dark terrains and of $0{,}34 \div 0{,}72$ (with a mean of $0{,}53$) for bright terrains.

To discriminate a region of the surface from another one according to albedo, we have use a picture representing the map of Ganymede surface containing the indication of longitude and latitude [55]. Preliminary, with the help of a photo-treatment software, the luminosity of the picture has been set so that it assume a value proportional to $0{,}12$ for the darkest point and to $0{,}72$ for the brightest point.

Subsequently, according to the subdivision already present, we have split the surface into $10° \; x \; 10°$ areas covering all the range of longitude from $0°$ to $360°$ and all the range of latitude from $-90°$ to $90°$ and we have analysed the luminosity of each obtained portion. In particular, for each square, we have extracted the histogram of luminosity for the pixels of that section and from it the value of the mean luminosity of the portion, which has been opportunely scaled in a range $0 \div 1$ in order to have an indication of the albedo of the zone.

Obtained data have been then collected into a matrix, where each row contains (ordered in columns) the initial and final longitude and latitude of the area and the corresponding extrapolated albedo.

Because the values of albedo calculated in this way are just an indication, for the assignment of the albedo ρ to the different areas we have conceptually divided Ganymede's surface into three kinds of terrain, each of them individuating a band of albedo associated with a mean value:

- low-albedo terrains $[0{,}12 \leq \rho < 0{,}34]$ with a medium of $0{,}25$;
- intermediate-albedo terrains $[0{,}34 \leq \rho \leq 0{,}53]$ with a medium of $0{,}43$;
- high-albedo terrains $[0{,}53 < \rho \leq 0{,}72]$ with a medium of $0{,}62$ (the mean value between $0{,}53$ and $0{,}72$);

Therefore, the operating steps for the block *search in Ganymede's virtual map* are:

- reading of the current values of geographical coordinates;
- individuation of the portion of surface in which longitude and latitude are comprised;
- eventual assignment of roughness value according to the latitude;
- extraction of the stored value of albedo deduced with luminosity analysis corresponding to the individuated portion of surface;
- identification of the type of terrain corresponding to albedo among the up-defined bands;
- assignment of the value of albedo according to the medium one of the individuated band.

All the albedo values corresponding to the different instant of time (eventually also data for roughness) are collected in a vector, that is added, as further column, to the matrix *data* seen in paragraph *4.3.2*.

4.5 Performance model

The evaluation of laser altimeter performance is based on the concept that a portion of the reflected optical pulse is collected by the receiver telescope, focused into a detector, constituted, by an APD with an interferential filter centred on laser wavelength, and then analysed in width by an Electronic Unit (see *chapter 3*).

We assume that the ground target is a lambertian surface and no specular reflections have been considered [56].

The main parameters useful to characterize the performances of a laser altimeter for topographical analysis of a planetary surface are:

- ***received pulse width*** $\boldsymbol{\sigma_p}$ [ns] representing how much the pulse has been spread in time due to the reflection by the surface;
- ***Signal-to-Noise Ratio*** $\boldsymbol{SNR}$ representing the ratio between the signal and noise power;
- ***range accuracy*** $\boldsymbol{\Delta R}$ [m] representing the range error in the measurement.

Received pulse width. As explained in *paragraph 3.2.1*, the transmitted laser pulse, with a width σ_l, power P_t and total energy E_t, when reflected is distorted by the surface topographical variations within the laser footprint (see figure *3.4*).

For this reason, backscattered pulse has a minor peak power since the pulse transmitted energy, unless small absorption losses, is spread along a major interval of time and has a more irregular shape which cannot be predicted a priori because it depends on surface profile and, as consequence of that, contains information about roughness, slope and albedo [56].

An analytic expression for the mean square detected pulse width σ_p^2 adapted for nadir viewing is provided by *Gardner* [53] [56]:

$$\sigma_p^2 = (\sigma_l^2 + \sigma_h^2) + \frac{4 \cdot Var(\Delta\xi)}{c^2} + \frac{4 \cdot R^2 \cdot \tan^2\theta}{c^2}(\tan^2\theta + \tan^2 S) \qquad (4.5.1)$$

where

- σ_l is the laser pulse width (s);
- σ_h is the rms width of receiver impulse response (s);
- $var(\Delta\xi)$ is the variance (m^2) of surface roughness, that is the square of the rms value of $\Delta\xi$ (m) (see paragraph *4.4)*;
- c is the velocity of light in vacuum (m/s);
- R is the range to surface (m);
- θ is the laser beam divergence angle (rad);
- S is the surface slope (rad).

Detected pulse with σ_p^2 is essentially functions of three terms [56]:

- effects due to the system;
- roughness effects;
- effects due to the beam curvature and slope.

Signal-to-Noise Ratio. An adequate Signal-to-Noise Ratio (SNR) is fundamental in order to obtain high-quality ranging data, then altimeter performances analysis has to verify its values and how they influence the ranging resolution.

In particular, laser altimeter signal strength depends on laser pulse power backscattered from the target surface and collected by the receiver telescope. Processes like optical shot noise, background noise, detector noise and pre-amplifier noise reduces

the capacity to discriminate the received pulse from background and electronic noise. Evaluating these components of noise, it is possible to compute SNR [56].

As seen in *chapter 3*, the laser altimeter receiver subsystem is formed by a telescope, an APD detector and an interference filter centred on laser wavelength. Assuming that the fluctuation of background noise intensity is not at frequencies falling within the filter bandwidth, the signal-to-noise ratio at the output of the filter (for a nadir-pointing altimeter) can be written as follows [56]:

$$SNR = \frac{I_S^2}{I_N^2} = \frac{G^2 \cdot I_{SD}^2}{I_{NS}^2 + I_{NB}^2 + I_{ND}^2 + BI_A^2} \tag{4.5.2}$$

where

- I_S is the signal current from APD (*A*);
- I_N is the noise current (*A*);
- I_{SD} is the signal current impinging on detector (*A*);
- I_{NS} is the noise signal current (*A*);
- I_{NB} is the noise background current (*A*);
- I_{ND} is the contribute to noise depending on APD dark current I_D (*A*);
- I_A is the APD noise current (*A/Hz*$^{1/2}$);
- G is the APD gain;
- $B = 1/3\tau$ is the detection bandwidth (*Hz*) with τ low-pass filter response width (*ns*) set to $\sqrt{\sigma_p^2 - \sigma_h^2}$. By means of this position, we suppose an ideal bandwidth, adaptable for every backscattered signal.

The signal current impinging on detector I_{SD} is equal to [56]:

$$I_{SD} = \frac{e \cdot n_s}{\sigma_P}$$

with e the electron charge, σ_P the echo pulse width given by ***equation (4.5.1)*** and n_s the number of signal photoelectrons generated per pulse calculated as [56]

$$n_S = \frac{E_t}{h\nu}\frac{\rho}{\pi}\frac{A_R}{R^2}\eta_{RX}\eta_{APD}\eta_{TX}\eta_f$$

where

- E_t is the transmitted laser pulse energy (J);
- $h\nu$ is the photon energy (J) with h the Planck's constant ($J{\cdot}s$) and ν the photon frequency (Hz) equal to the velocity of light-wavelength ratio (c/λ);
- ρ is the surface albedo;
- A_R is the receiving area (m^2) equal to $\pi(d/2)^2$ with d the diameter of the receiver telescope (m);
- R is the range to surface (m);
- η_{RX} is the receiver transmission;
- η_{APD} is the APD quantum efficiency;
- η_{TX} is the optics transmittance;
- η_f is the interference filter transmittance.

The noise signal current I_{NS}, instead, is [56]:

$$I_{NS} = \sqrt{2eBI_{SD}FG^2}$$

where F is called excess noise factor and values

$$F = k_{eff}G + \left(2 - \frac{1}{G}\right)\left(1 - k_{eff}\right)$$

with k_{eff} the ionization coefficient ratio.

For the noise background current I_{NB} we have [56]:

$$I_{NB} = \sqrt{2eBI_BFG^2}$$

with I_B the background current (A) given by [56]

$$I_B = e\left(\lambda_{SUN} + \lambda_{GAN} + \lambda_{JUP}\right)$$

where

- λ_{SUN} is the number of solar background photoelectrons per second (s^{-1});
- λ_{GAN} is the Ganymede's radiation photons rate (s^{-1});
- λ_{JUP} is the number of background photoelectrons per second due to Jupiter's emission (s^{-1}).

In particular [56]:

$$\lambda_{SUN} = \frac{I_{SUN}}{h\nu}\rho A_R\left(\frac{\theta_{FOV}}{2}\right)^2 \eta_{RX}\eta_{APD}\eta_f \Delta\lambda_f$$

$$\lambda_{GAN} = \frac{I_{GAN}}{h\nu} A_R\left(\frac{\theta_{FOV}}{2}\right)^2 \eta_{RX}\eta_{APD}\eta_f \Delta\lambda_f$$

$$\lambda_{JUP} = \frac{I_{JUP}}{h\nu}\rho A_R\left(\frac{\theta_{FOV}}{2}\right)^2 \eta_{RX}\eta_{APD}\eta_f \Delta\lambda_f$$

where

- θ_{FOV} is the receiver field of view (*rad*);
- $\Delta\lambda_f$ is the interference filter bandpass (*nm*);
- I_{SUN} is the solar spectral power density at laser wavelength at the distance of Ganymede (*W/m^{2}nm*);
- I_{GAN} is the Ganymede's spectral power density at laser wavelength at the distance of spacecraft (*W/m^{2}nm*);
- I_{JUP} is the Jovian spectral power density at the laser wavelength at the distance of Ganymede (*W/m^{2}nm*);

Spectral power density (the power emitted per unit of area and time at a certain wavelength) at a certain distance from the emitting body can be computed as the product of this body's spectral radiant emittance W and a viewing factor Ω_{e-r} which considers the size of the emitting body and the distance from it:

$$I = W\Omega_{e-r}$$

with the emittance function of temperature and wavelength, according to the Planck's law

$$W = \frac{2\pi hc^2}{\lambda^5}\frac{1}{e^{\frac{ch}{\lambda kT}} - 1}$$

where

- λ is the laser wavelength (m);
- k is the Boltzmann's constant (*J/K*);
- T is the absolute temperature of the emitting body (*K*) supposed in approximation a black body

and the viewing factor Ω_{e-r} equal to

$$\Omega_{e-r} = \frac{4\pi r_{emit}^2}{4\pi D_{emit\_receiv}^2} = \left(\frac{r_{emit}}{D_{emit\_receiv}}\right)^2$$

that is, the ratio between the superficial area of the spherical emitting body end the area of the imaginary sphere individuated by the distance from the source of emission of the body affected by radiation. Then for the three cases under consideration, we have:

$$I_{SUN} = W(T = T_{SUN}, \lambda)\frac{r_{SUN}^2}{D_{GAN\_SUN}^2}$$

$$I_{GAN} = W(T = T_{GAN}, \lambda)\frac{r_{GAN}^2}{D_{SAT\_GAN}^2}$$

$$I_{JUP} = W\big(T = T_{JUP}, \lambda\big)\frac{r_{JUP}^2}{D_{GAN\_JUP}^2}$$

For temperature values we distinguish two cases:

- *night conditions*
- *daylight conditions*

In night condition $I_{SUN} = 0$ and hence $\lambda_{SUN} = 0$, while I_{GAN} is evaluated with the night temperature of surface $T_{GAN\_NIGHT} = 70\,K$. In daylight conditions I_{SUN} is computed with reference to the Sun medium surface temperature $T_{SUN} = 5778\,K$ and I_{GAN} according to the day temperature of Ganymede $T_{GAN\_DAY} = 152\,K$. For I_{JUP}, instead, we don't separate any case, supposing that the Jovian radiation is always present.
Finally, I_{ND} can be computed with the following relation [56]:

$$I_{ND} = \sqrt{2eI_D B}$$

where I_D represents the APD dark current.

Taking into account the formulas for all the different sources of noise, the Signal-to-Noise Ratio can be written as:

$$SNR = \frac{G^2\left(\frac{e \cdot n_S}{\sigma_p}\right)^2}{2eBFG^2\left[e\big(\lambda_{SUN} + \lambda_{GAN} + \lambda_{JUP}\big) + \frac{e \cdot n_S}{\sigma_p}\right] + 2eBI_D + BI_A^2} \qquad (4.5.3)$$

Ranging resolution. The ranging measurement resolution ΔR for a laser altimeter operating with the *TOF* single shot technique results inversely proportional to SNR and directly proportional to the pulse spreading, according to the following relation [56]:

$$\Delta R = \frac{c \cdot \sigma_p}{2 \cdot SNR} \tag{4.5.4}$$

where

- σ_p is the received pulse width given by *equation* (*4.5.1)*;
- SNR is the Signal-to-Noise Ratio given by *equation* (*4.5.3)*.

For evaluating performance, according to *equation (4.5.1)*, *(4.5.3)* and *(4.5.4)*, the values of all the general constants and all the parameters characterizing the instrument and the scenario of the mission are reported in table *4.1*. As mentioned in previous paragraphs, the values for R and ρ are provided respectively by the orbital propagator and the virtual map of Ganymede surface, while the values for $var(\Delta\xi)$ and S have been indicated above.

PARAMETER	SYMBOL	UNIT	VALUE
GENERAL CONSTANTS			
elementary charge	e	C	$1{,}602176 \cdot 10^{-19}$
Planck's constant	h	Js	$6{,}62606896 \cdot 10^{-34}$
velocity of light in vacuum	c	m/s	299792458
Boltzmann's constant	k	J/K	$1{,}3806505 \cdot 10^{-23}$
TRANSMITTER PARAMETERS			
laser transmitter's energy per pulse	E_t	mJ	50 [57]
laser pulse width	σ_l	ns	3,4 [57]
laser wavelength	λ	nm	1064 or 532 [table 3.2]
laser beam divergence (referred to 200 km of altitude)	θ	mrad	0,2
optics transmittance	η_{TX}		0,8 [57]
RECEIVER PARAMETERS			
receiver transmission	η_{RX}		0,7 [57]
receiver field of view	θ_{FOV}	mrad	0,2 [table 3.2]
receiver telescope diameter	d_R	cm	25 [table 3.2]
receiver area	A_R	m^2	0,0491
rms width of receiver impulse response	σ_h	ns	0
interference filter receiver bandpass	$\Delta\lambda_f$	nm	1 [table 3.2]
interference filter transmittance	η_f		0,8 [57]

DETECTOR PARAMETERS			
APD quantum efficiency	η_{APD}		0,38 [57]
dark current	I_D	A	$50 \cdot 10^{-12}$ [57]
noise current	I_A	$A/Hz^{0.5}$	10^{-12} (LAPE heritage [56])
APD gain	G		150 [57]
ionization coefficient ratio	k_{eff}		0,008 (LAPE heritage [56])
excess noise factor	F		3,177386
MISSION PARAMETERS			
night absolute temperature of Ganymede surface	T_{GAN_NIGHT}	K	70 [table 2.1]
day absolute temperature of Ganymede surface	T_{GAN_DAY}	K	152 [table 2.1]
mean absolute temperature of Sun surface	T_{SUN}	K	5778 [58]
mean absolute temperature of Jupiter external clouds	T_{JUP}	K	165 [59]
Sun mean radius	R_{SUN}	km	696000 [58]
Ganymede mean radius	R_{GAN}	km	2631,2 [table 2.1]
Jupiter mean radius	R_{JUP}	km	69173 [59]
mean Sun-Ganymede distance	D_{SUN_GAN}	km	$778{,}36 \cdot 10^6$ [table 2.1]
mean Jupiter-Ganymede distance	D_{JUP_GAN}	km	1070400 [table 2.1]
Ganymede-spacecraft distance (orbital altitude)	D_{GAN_SAT}	km	200 (paragraph 1.4.1)

TABLE 4.1 Values of main parameters used in the performance model

Figure *4.4* illustrates the input-output data of the performance model.

FIGURE 4.4 Input-output block diagram of the performance model

Given the physical features (albedo, roughness and slope) of the portions of surface flown over during the chosen interval of time and through the instrument and mission parameters, performance are evaluated for each instant of time (for each taken sample) thanks to the current values related to it collected in the matrix *data*. In particular, for each time, the roughness is fixed while the slope is variable with a step set by the user (ΔS), so

that, for the same point, we have the values of performance for different values of slope within the interval of interest ($0° \div 20°$).

All performance data are then collected in a matrix reporting, per columns, the values of the echo pulse width, the Signal-to-Noise-Ratio and the ranging resolution for each taken slope S_j. The rows represent the different instants of time. Then this matrix is added to the previously defined matrix *"data"* (see *paragraph 4.3.2* and *4.4*), which at the end will have this form:

$$\left[d_{from\ t_{in}} \quad \varphi \quad \lambda \quad H \quad v_{tot} \quad v_{rad} \quad v_{tan} \quad \nu \quad \rho \quad \Delta\xi \quad (S \quad \sigma_p \quad SNR \quad \Delta R)_{S_j}\right]$$

4.6 Plot

The last block of the program has been developed in order to plot all the obtained data in a significant form. The software, which uses an orbital propagator for sampling time, has been though to plot temporal profiles of the quantities of interest, in order to evaluate how they vary with respect to time (expressed as days past to the initial date), eventually throughout the whole mission.

4.7 Final considerations

Figure *4.5* shows a general scheme of the software as a whole, with its inputs and outputs. Starting from the orbital parameters describing the orbit around Ganymede, the initial and final dates of propagation with a temporal step and eventually the values for roughness and slope of the surface, the software returns the ground track of the spacecraft through longitude and latitude, temporal profiles of velocities, altitude, satellite's position and physical characteristics of the surface and, about laser altimeter performances, the echo pulse width, the signal to noise ratio and the range accuracy as functions of time, slope and roughness. Moreover, to improve the software's flexibility and potentialities, some controls directly editable by the user have been inserted. In particular the choice opportunities include the possibility of:

- considering or not oblateness perturbing effects;
- setting laser wavelength between 532 and 1064 nm;
- considering day or night conditions;
- setting a single value for slope or using this quantity in a parametric form;
- setting a single value for roughness of using two values for it according to latitude;
- choosing what type of data to plot (orbital ones, performances ones or both).

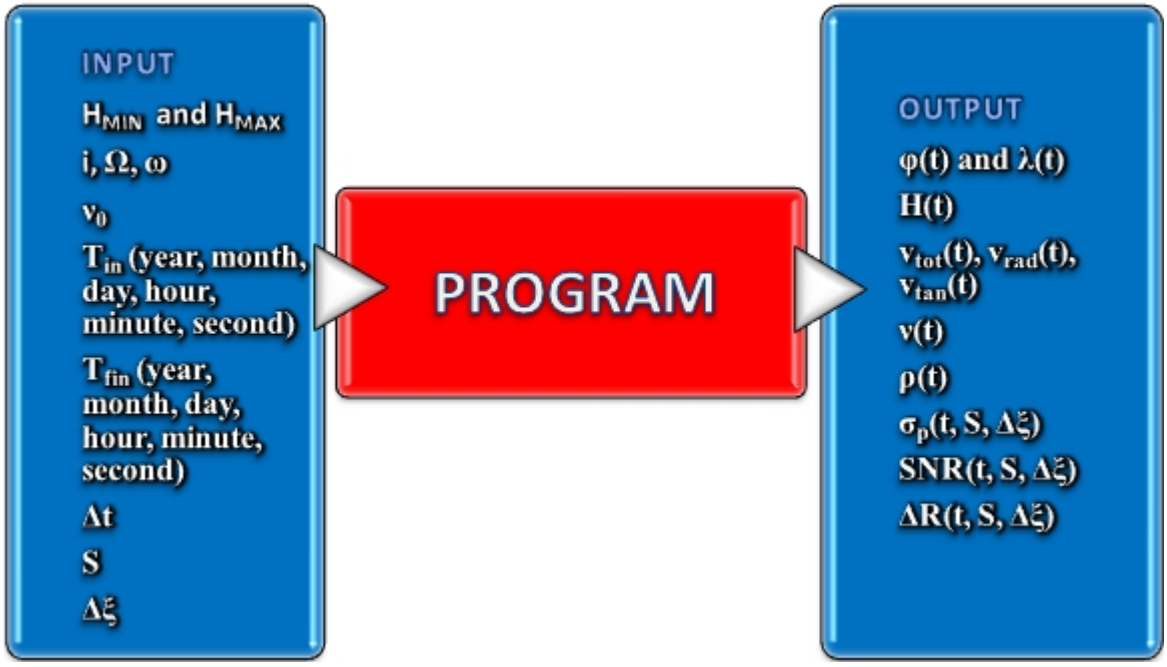

FIGURE 4.5 Input-output block diagram of the whole program

CHAPTER 5

Results

In this final chapter we report the most significant results obtained implementing the software described in *chapter 4* according to the *EJSM* mission scenario and we report the performance analysis of laser altimeter. As already mentioned in *chapter 3*, since the technology of Micro Laser Altimeter is just in a very preliminary phase of study, we decide to analyse the performance only for the classic Laser Altimeter developed on *BELA* heritage.

As described in *chapter 1*, the laser altimeter for *JGO* will operate during the *Ganymede Science Phase* and particularly during the circular sub-phase, more suitable than the elliptic one for topographic studies of the surface. Indeed, the low altitude and very high inclination of the circular orbit guarantees a good coverage in a relatively short time and the possibility to investigate the surface from a very reduced distance then with a major accuracy.

The main parameters of the circular orbit around Ganymede are:

- ***altitude*** $H = 200\ km$;
- ***inclination*** $i = 87{,}5°$;
- ***right ascension of the ascending node*** $\Omega = 0°$;
- ***argument of periapsis*** $\omega = 0°$;
- ***initial true anomaly*** $\nu_0 = 0°$.

Information about the right ascension of the ascending node (Ω) is not provided, and we have supposed that the ascending node is positioned on the *x*-axis of the inertial reference system. It has to be noted that for the purpose of our analysis, this angle is not fundamental, because it just influences just the initially flown over portion of surface. This means that for a global coverage, the results remain the same but they are simply shifted in time.

For the other two parameters ω and ν_0, considering that the periapsis is not definite for a circular orbit but can be useful just as reference point to count the true anomaly, we

make the assumption that it coincides with the ascending node (ω = 0°) and that the spacecraft is situated in this point in the initial instant of time (ν_0 = 0°).

As seen in *paragraph 1.4.1*, the circular orbital phase will be limited to 105 days for limit of radiation dose requirements. According to the foreseen mission dates, for initial and final times we consider the following dates:

- ***initial date*** T_{in} = 12:00:00 of 16/2/2027
- ***final date*** T_{fin} = 12:00:00 of 31/5/2027

where the indication for hours has been chosen for simplicity.

Before to analyse the laser altimeter performance, let we make some considerations on the orbit results.

With reference to figure *5.1*, we can see how the coverage in longitude is practically total, while that in latitude is limited by the inclination of the orbit, then areas with latitudes major than ± 87,5° are not interested by observations.

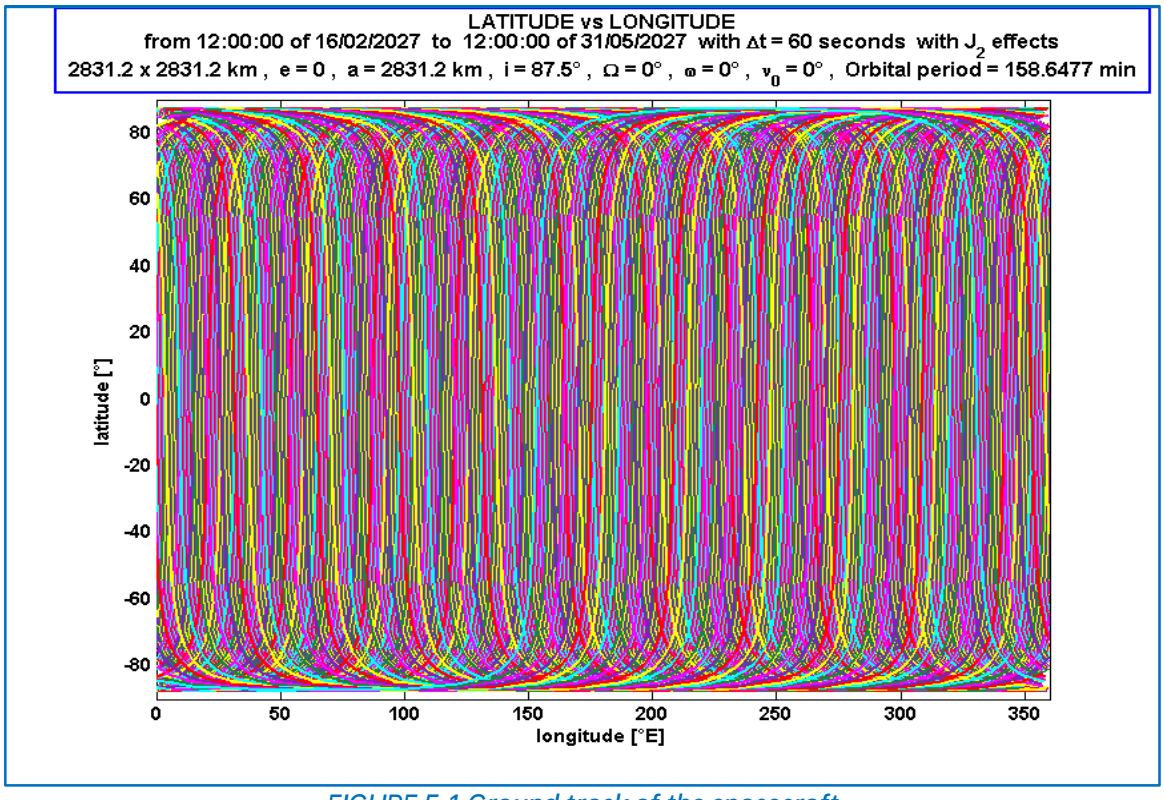

FIGURE 5.1 Ground track of the spacecraft

For this orbit, the altitude remains constant with time (figure *5.2*), with important consequences for performance which will not be influenced by this parameter. Moreover, also the velocity doesn't change during the orbit and the mission (figure *5.3*), keeping

always tangential, resulting in an uniform horizontal mapping accuracy. In figure *5.4* and figure *5.5* are reported respectively radial speed and tangential speed with respect to time.

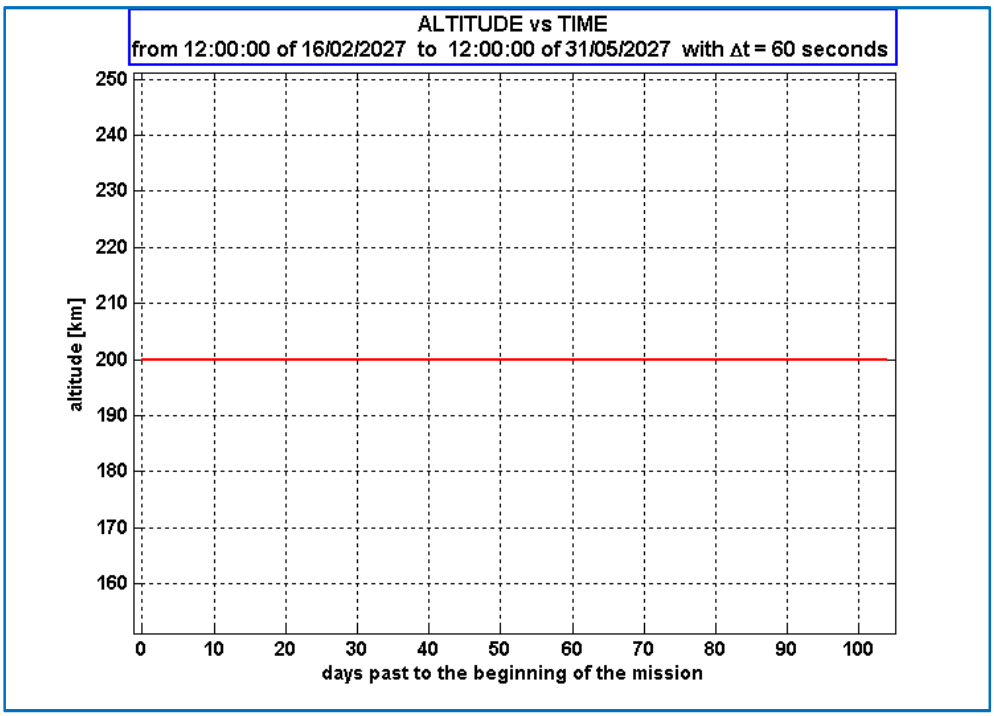

FIGURE 5.2 Altitude as function of time

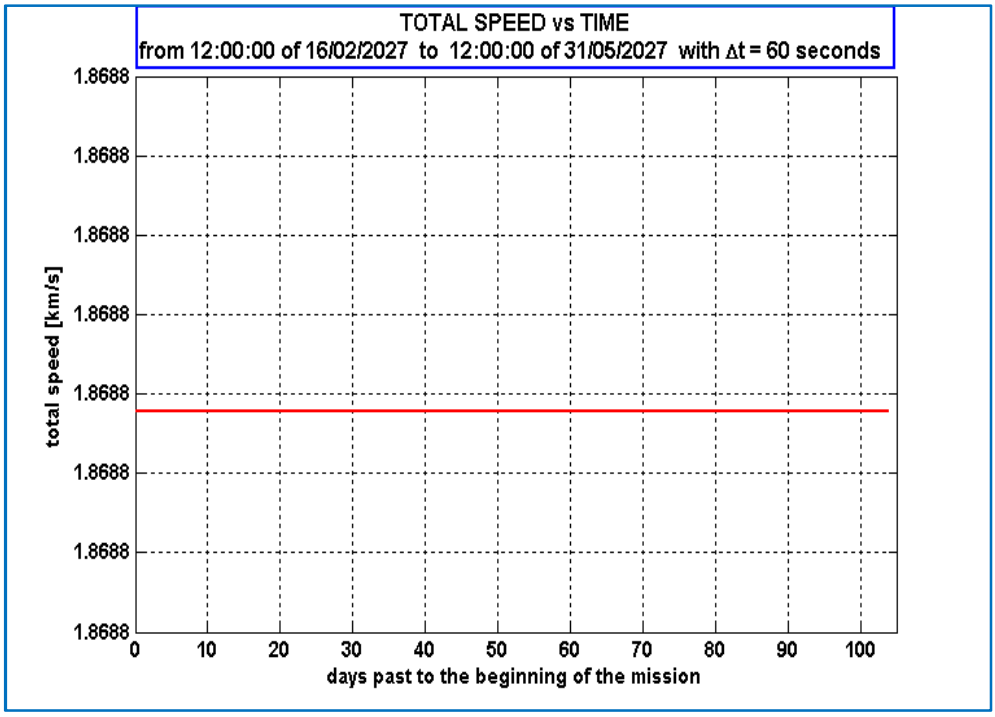

FIGURE 5.3 Total speed as function of time

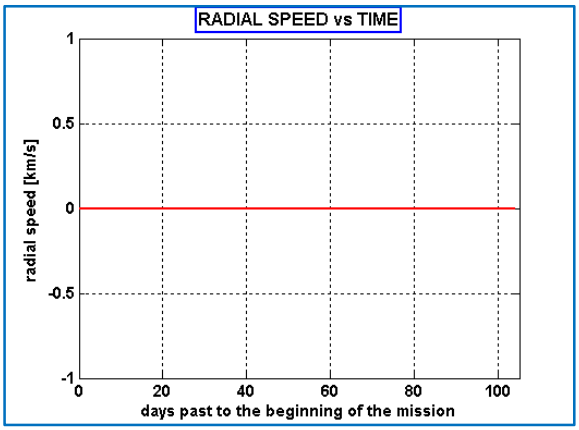

FIGURE 5.4 Radial speed as function of time

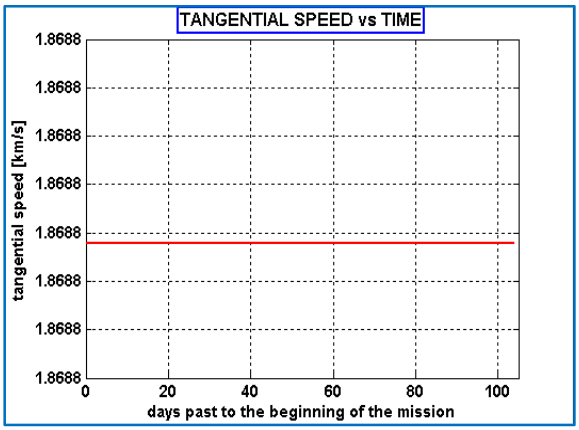

FIGURE 5.5 Tangential speed as function of time

The results of the previous figures have been obtained considering the term J_2.
Nevertheless, as we can note, the perturbing effect due to the Ganymede's non-sphericity doesn't influence neither the altitude nor the value of velocity. Indeed, it produces just a rotation of the orbit in its plane and a rotation with respect to the inertial frame, determining only a shifting of the ground-track of the spacecraft. As said for the definition of Ω, for our purpose this effect is not determinant.

After this introduction, we will examine firstly the echo pulse width varying slope and roughness, secondly the Signal to Noise Ratio and the range resolution for different values of slope, roughness and albedo, for daylight and night conditions and for two different laser wavelengths.

5.1 Echo pulse width

The spreading of the width of the received pulse with respect to the transmitted one is function of four terms (*paragraph 4.5, equation (4.5.1)*):

- *system effects* depending on the *rms* width of receiver impulse response;
- *roughness effects* depending on the *rms* value of surface roughness;
- *slope effects* depending on the altitude, the divergence of the laser beam and the value of surface slope;
- *beam curvature* effects depending on the divergence of the laser beam and the altitude.

Fixing the receiver impulse response width ($\sigma_h = 0$) and the laser beam divergence ($\theta = 0{,}2\ mrad$), because the altitude remains constant ($H = 200\ km$), the echo pulse width varies only with respect to surface slope and roughness.

Figures *5.6* shows the variation of σ_p respectively with slope for three different values of roughness, while the following table *5.1* reports some corresponding obtained values.

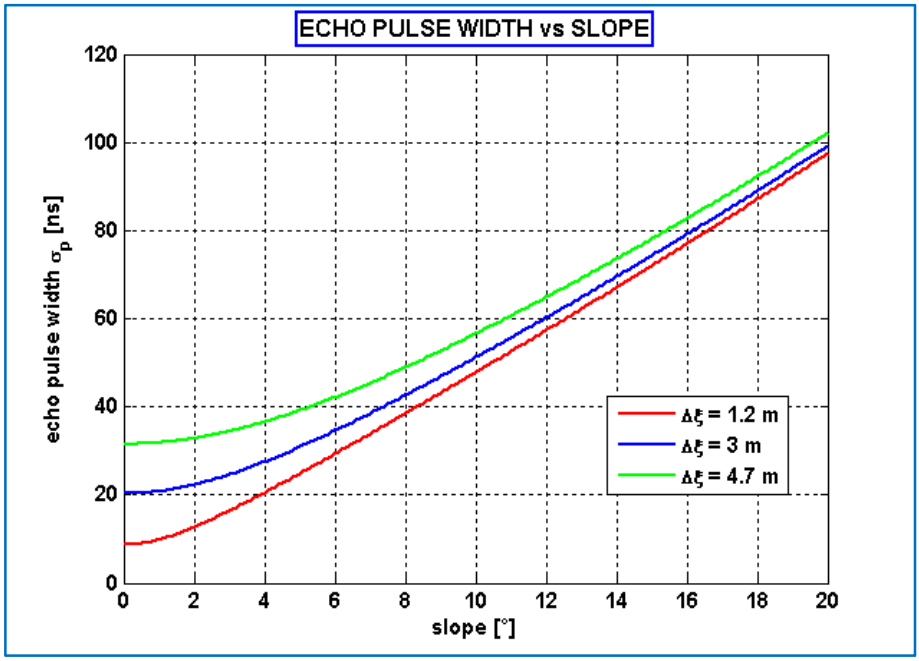

FIGURE 5.6 Echo pulse width as function of slope for different values of roughness

slope / roughness	1,2 m	3 m	4,7 m	
0°	8,6978	20,3007	31,5389	σ_p [ns]
5°	24,9140	30,9383	39,2397	
10°	47,8502	51,2456	56,6453	
15°	72,0297	74,3286	78,1493	
20°	97,5146	99,2248	102,1183	

TABLE 5.1 Values of the echo pulse width [ns] for different values of slope and roughness

As we can note, fixed the roughness, the echo pulse width increases with slope and its variations, for a given difference of slope, grow as the value of slope increases. In the same way, fixed the slope, σ_p raises with roughness and increasing value of $\Delta\xi$ the increment of σ_p becomes higher and higher. The effects of roughness are more important for low slopes (big variations in σ_p) than for high slopes (very small variations).

Being the receiver ideal ($\sigma_h = 0$), setting both slope and roughness to 0, we can also compute the contribute to pulse spreading due to laser beam divergence and altitude. With this position it is possible to verify that the effects due to laser and altitude practically do not alter the transmitted pulse width, so that the received pulse width is not spread if the lit up area is an ideal surface with a slope and a roughness null.

On the opposite, in the worst case in which both slope and roughness assume the respective maximum values (20° and 4,7 m), according to table *5.1*, the maximum echo pulse width is 102,12 ns with a spreading of 98,72 ns, considering that the transmitted laser pulse is 3,4 ns (BELA heritage).

Finally, the dependence of σ_p with time is not significant at all because this quantity, fixing slope and roughness, remains constant during the orbit and the mission. Indeed, it doesn't depend on the albedo of the flown over area of the surface and the altitude doesn't vary.

5.2 Signal to Noise Ratio

With reference to *paragraph 4.5*, the signal to noise ratio in output to the detector is directly proportional to the current due to the signal I_S and inversely proportional to the noise current I_N, which depends in turn on the noise signal current I_{NS}, the noise background current I_{NB}, the APD noise current I_A and a term representing the APD dark current I_{ND}. In particular, for making more clear the dependence of SNR from the variable quantities of our model, let we rewrite ***equation (4.5.3)*** making explicit some terms:

$$SNR = \frac{G^2\left(\frac{en_S}{\sigma_p}\right)^2}{2eB\left\{\frac{en_S}{\sigma_p}FG^2 + I_D + \frac{e}{h\nu}A_R\left(\frac{\theta_{FOV}}{2}\right)^2\eta_{RX}\eta_{APD}\eta_f\Delta\lambda_f\left[\rho I_{SUN} + I_{GAN} + \rho I_{JUP}\right]FG^2\right\} + BI_A^2}$$

where

$$n_S = \frac{E_t}{h\nu}\frac{\rho}{\pi}\frac{A_R}{R^2}\eta_{RX}\eta_{APD}\eta_{TX}\eta_f \quad \text{with} \quad h\nu = h\frac{c}{\lambda}$$

$$\sigma_p = \sqrt{(\sigma_l^2 + \sigma_h^2) + \frac{4\cdot Var(\Delta\xi)}{c^2} + \frac{4\cdot R^2\cdot\tan^2\theta}{c^2}(\tan^2\theta + \tan^2 S)}$$

$$B = \frac{1}{3\tau} \quad \text{with} \quad \tau = \sqrt{\sigma_p^2 - \sigma_h^2}$$

$$I = \frac{2\pi hc^2}{\lambda^5} \frac{1}{e^{\frac{ch}{\lambda kT}} - 1} \left(\frac{r_{emit}}{D_{emit\_receiv}} \right)^2$$

Fixing the altitude of the spacecraft R, the features of the instrument (G, E_t, A_R, η_{RX}, η_{APD}, η_{TX}, η_f, σ_l, σ_h, θ, F, I_D, θ_{FOV}, $\Delta\lambda_f$, I_A) and the mission parameters (r_{emit}, D_{emit_receiv} and T of Sun, Jupiter and Ganymede) the signal to noise ratio is function of:

- the value of surface albedo ρ depending on the flown over area at a certain time;
- the value of surface roughness $\Delta\xi$;
- the value of surface slope S;
- the laser wavelength λ;
- daylight and night conditions which take into account the difference in the Ganymede's temperature and solar radiation.

We have to analyze how SNR varies with respect to each of these quantities. Firstly, we fix the laser wavelength to $1064\,nm$ and the conditions (daylight) showing the dependence of SNR with reference to the surface characteristics (albedo, roughness and slope); then, we will see how the Signal to Noise Ratio changes varying λ and the light/temperature conditions. The values of all the parameters employed in performance analysis are reported in table *4.1*.

***SNR* variations with respect to slope and roughness.** The variations of SNR with respect to slope and roughness are related to the echo pulse width σ_p, present as $1/\sigma_p^2$ at the numerator and as $1/\sigma_p$ at the denominator. Globally, considering that σ_p increases with slope and roughness, the signal to noise ratio decreases with respect to these quantities, becoming as smaller as their values are high.

This result is intuitive because if the profile of the surface is much irregular (high slope and roughness) reflections occurs mostly in a direction different from that of laser beam arrival, therefore the number of backscattered photons in the direction of the receiver telescope is minor. This supposition is confirmed by figure *5.7*, in which the Signal to Noise Ratio is plotted as function of slope for different values of roughness, fixed the albedo to its mean value (0,43).

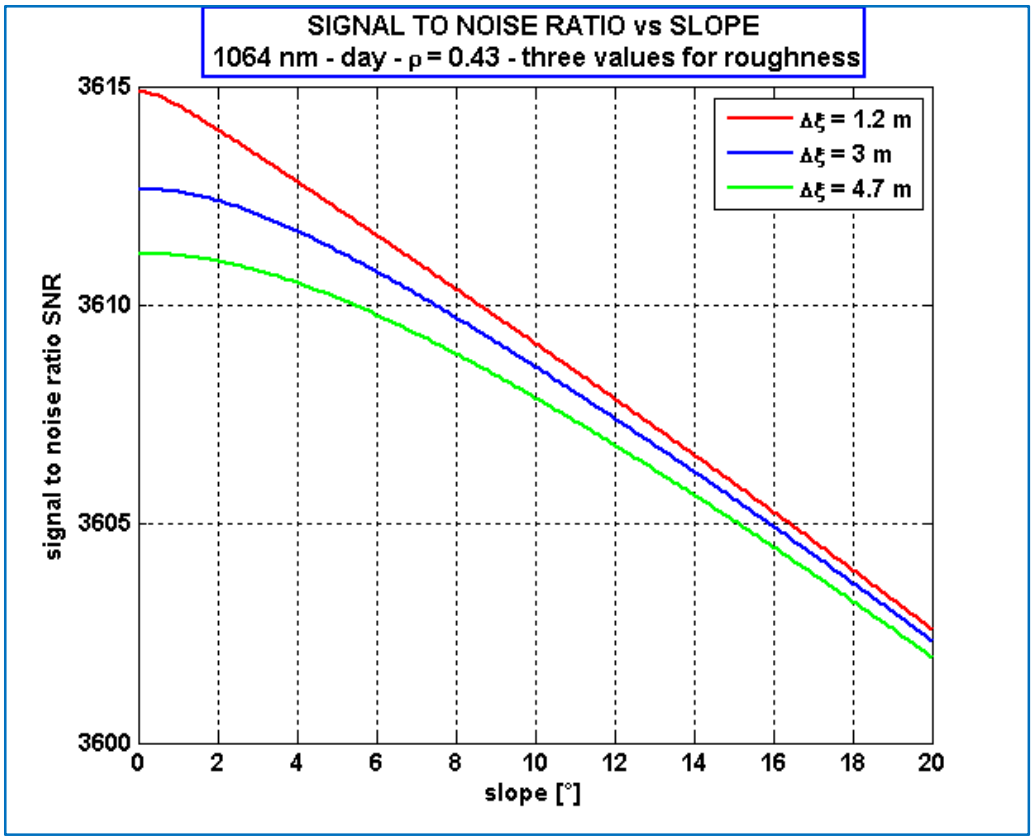

FIGURE 5.7 SNR as function of slope for different values of roughness (albedo 0,43 - daylight conditions – 1064 nm)

However, it has to be noted that, because of the relative small values of slope range (from 0° to 20°), the variation of SNR in percentage is around 0,3%. Moreover, fixed the slope, the variation due to roughness is even more small and this effect is ever less evident with increasing slope (figure *5.7*).

This trend doesn't change with the value of albedo. In particular, the decrement of SNR in the range $[0° - 20°]$ in absolute value remains almost constant also for $\rho = 0{,}25$ and for $\rho = 0{,}62$. It has to be noted that as albedo arises, the SNR value in percentage is less influenced by the slope. This consideration is shown in figure *5.8* and *5.9*, obtained considering an albedo of 0,25 and of 0,62 respectively.

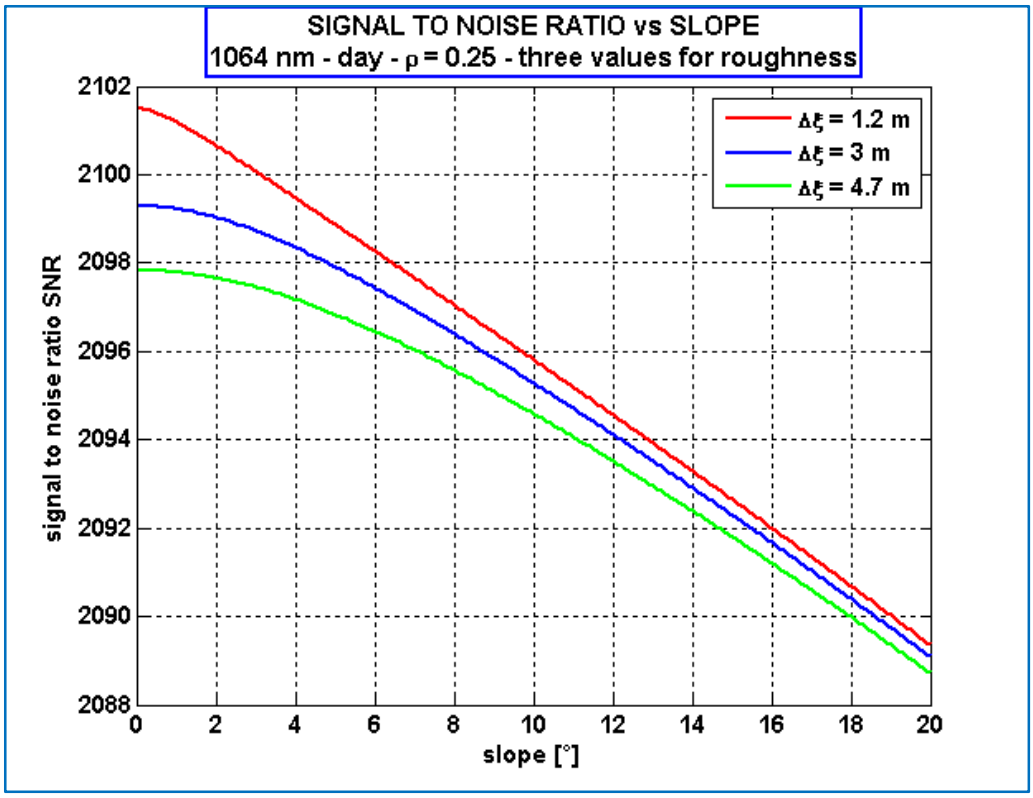

FIGURE 5.8 SNR as function of slope for different values of roughness (albedo 0,25 - daylight conditions – 1064 nm)

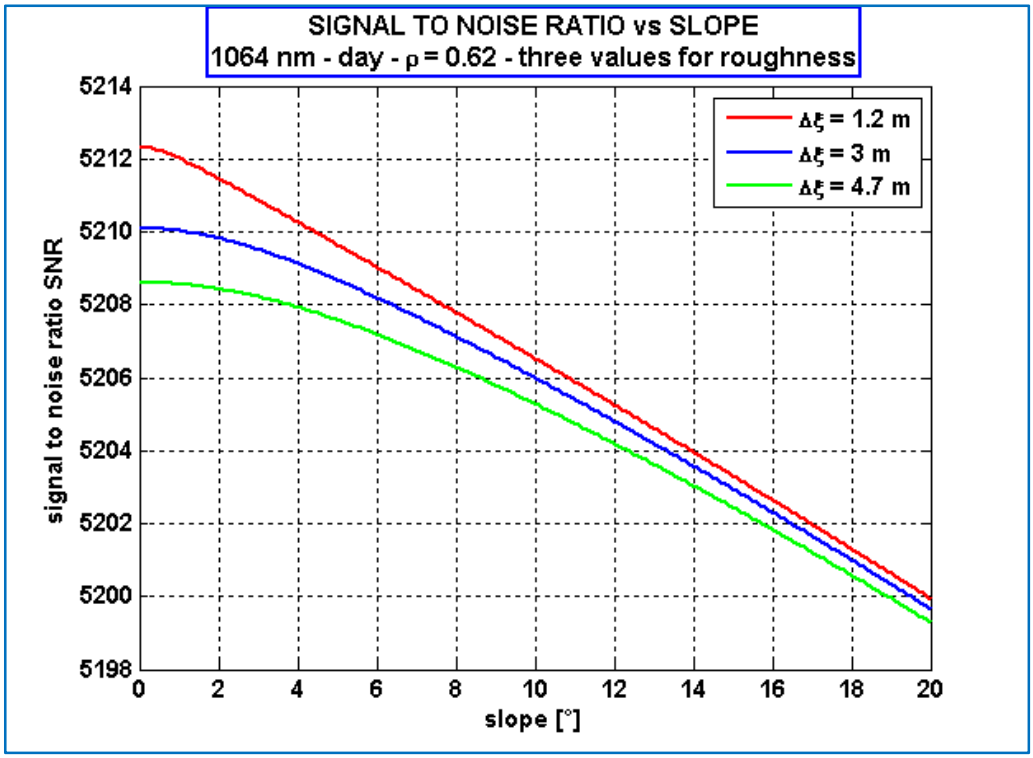

FIGURE 5.9 SNR as function of slope for different values of roughness (albedo 0,62 - daylight conditions – 1064 nm)

***SNR* variations with respect to albedo.** The value of albedo influences the number n_S of photoelectrons backscattered from the surface and collected by the instrument but also the fraction of background noise due to the radiation from the Sun and Jupiter reflected by the Ganymede's surface.

Because in the formula for SNR the numerator is proportional to the square of n_S while the denominator simply to n_S, the influence of albedo is more important for the signal than for the noise variations. An higher value of albedo leads to a greater value for the Signal to Noise Ratio as shown in figure *5.10*, where SNR is plotted as function of slope parameterizing the albedo rather than roughness. The differences due to slope are not significant because the variations of albedo are more influent than the variations in slope or roughness.

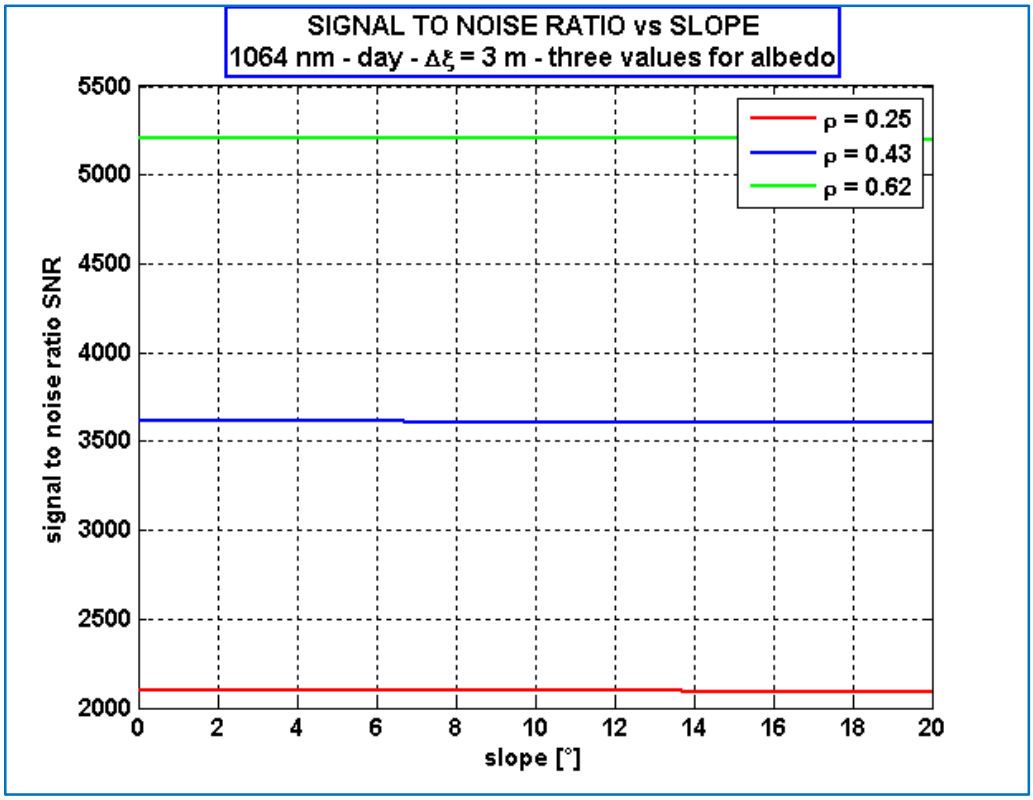

FIGURE 5.10 SNR as function of slope for different values of albedo (roughness 3 m - daylight conditions – 1064 nm)

If we consider the temporal profile of SNR, the value of albedo depends on the particular area of the surface pointed by the spacecraft at a certain time. Since we have schematized the Ganymede's surface in three kinds of terrains (low-albedo, intermediate-albedo and high-albedo terrains) if we plot the Signal to Noise Ratio as function of time we obtain a graph on three levels each corresponding to a type of terrain.

Therefore, for each time, fixed slope and roughness, the SNR will have a value according to the albedo of the zone of the surface flown over at the moment. In order to view that, we report in figure *5.11* the temporal profile of SNR obtained for the first day of the mission (just for simplicity) for different values of slope and with a mean roughness ($3\ m$).

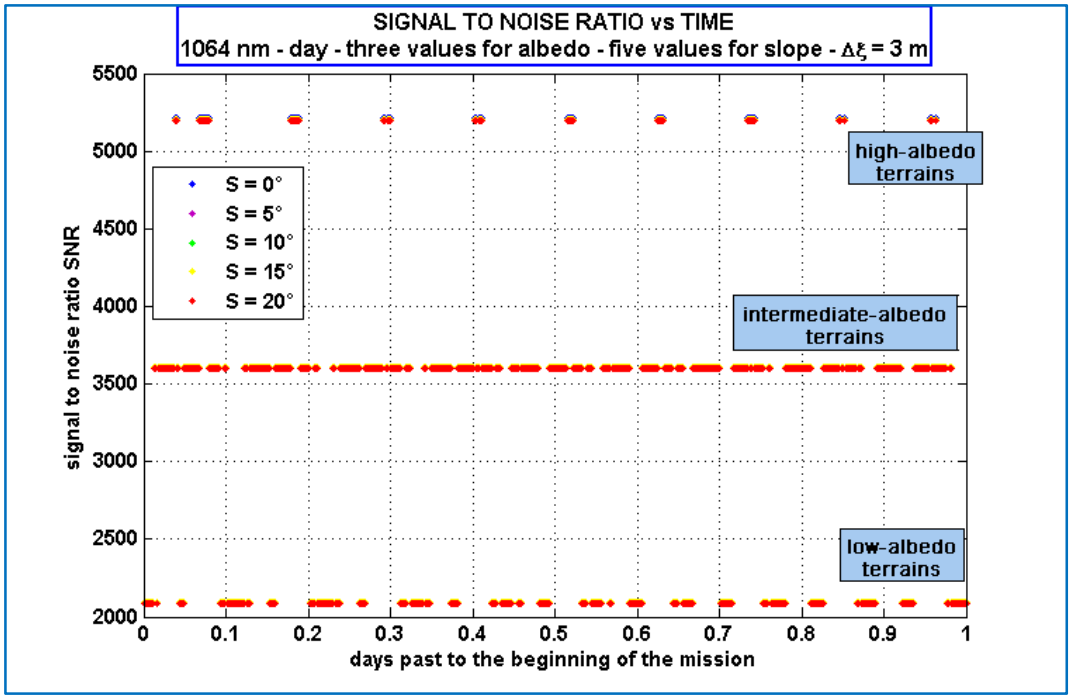

FIGURE 5.11 SNR as function of time for different values of slope (roughness 3 m - daylight conditions – 1064 nm)

As previously discussed, the variations of the Signal to Noise Ratio with slope are less evident if compared to those due to albedo. Making a zoom on the vertical axis these variations are evident in figure *5.12*, where just the band of intermediate-albedo terrains is considered.

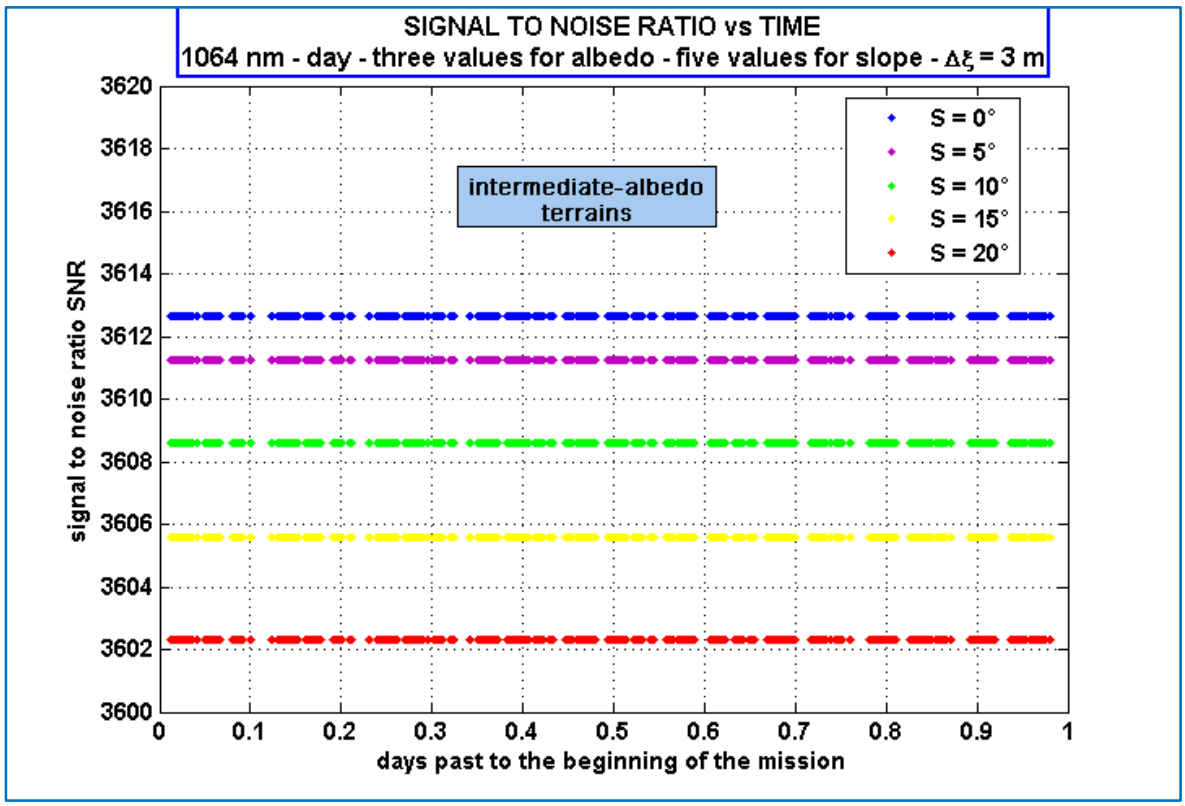

FIGURE 5.12 SNR as function of time for different values of slope (roughness 3 m – daylight conditions – 1064 nm) [zoom on intermediate-albedo terrains]

As it happens for σ_p, SNR variations for a fixed difference in slope increase as the value of slope increases and decrease as the value of roughness increases remaining these variations practically the same for the three different values of albedo. This is confirmed by the values of SNR reported in table *5.2* for different values of slope, roughness and albedo.

		roughness			
slope	albedo	1,2 m	3 m	4,7 m	
0°	0,25	2100,79	2099,28	2097,83	SNR
	0,43	3614,17	3612,65	3611,18	
	0,62	5211,63	5210,09	5208,61	
10°	0,25	2095,72	2095,28	2094,58	
	0,43	3609,05	3608,60	3607,89	
	0,62	5206,45	5206,00	5205,29	
20°	0,25	2089,31	2089,09	2088,72	
	0,43	3602,56	3602,36	3601,96	
	0,62	5199,89	5199,67	5199,29	

TABLE 5.2 Values of SNR for different values of slope, albedo and roughness (daylight conditions – 1064 nm)

***SNR* variations with respect to daylight/night conditions.** The Signal to Noise Ratio is influenced by the daylight and night conditions in the term of background noise current I_{NB} because during Ganymede night the solar radiation is absent and the temperature at surface is different from that during day: as consequence of that the power and the spectrum of emission of Ganymede change. For the radiation from Jupiter we have supposed that it is always present and it remains unvaried for both cases.

Therefore, while the signal current doesn't undergo any variation between day and night, during the day the amount of noise increases, leading to a minor Signal to Noise Ratio for daylight conditions with respect to night ones. Figure *5.13* illustrates the comparison between the two cases for SNR plotted as function of slope for a low albedo (0,25) and a low value of roughness (1,2 m). As we can see, the difference between the two curves increases, although very at all, with slope and, analyzing the plots for different values of albedo and roughness, it is possible to note how it increases also with roughness and mostly with albedo. In figure *5.14* and *5.15* are reported the same graphs of figure *5.13* varying in the first case only the roughness (set to 4,7 m) and in the second case also the albedo (set to 0,62).

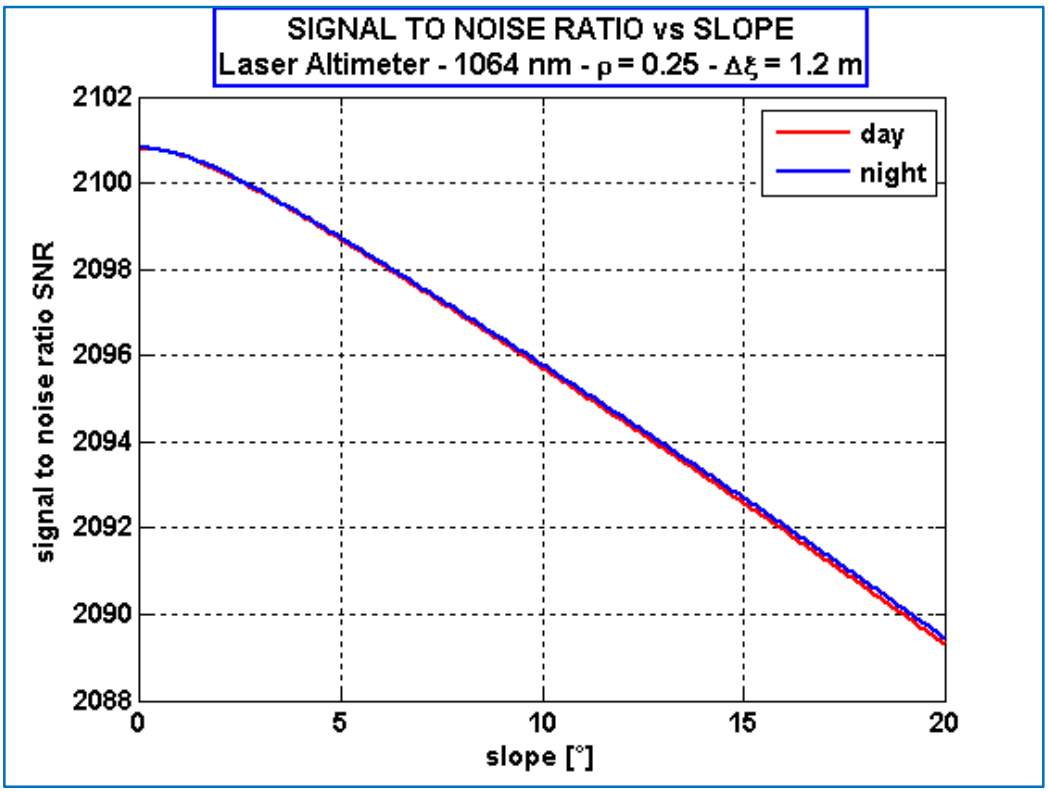

FIGURE 5.13 SNR as function of slope for daylight and night conditions (albedo 0,25 – roughness 1,2 m – 1064 nm)

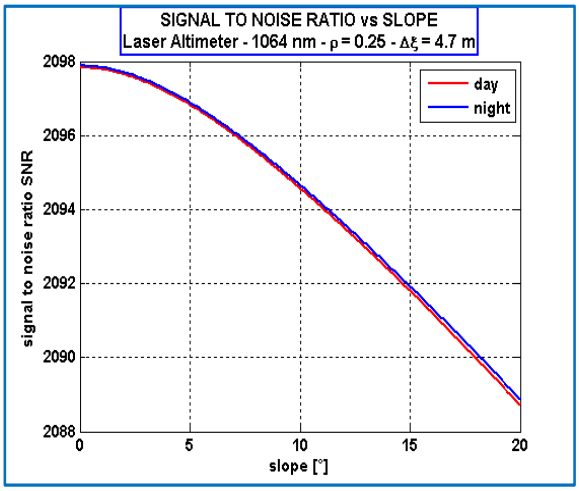

FIGURE 5.14 SNR as function of slope for daylight and night conditions (albedo 0,25 – roughness 4,7 m – 1064 nm)

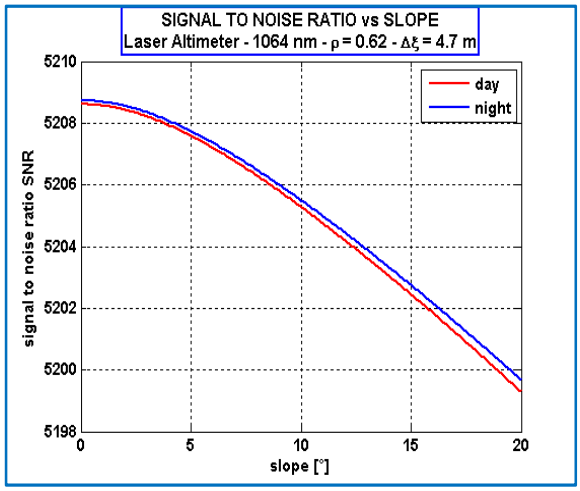

FIGURE 5.15 SNR as function of slope for daylight and night conditions (albedo 0,62 – roughness 4,7 m – 1064 nm)

In order to better estimate the variations in the Signal to Noise Ratio due to the different values of slope, roughness and albedo, refer to table *5.3*.

			condition		
slope	albedo	roughness	day	night	
0°	0,25	1,2 m	2100,79	2100,81	SNR
		4,7 m	2097,83	2097,88	
	0,62	1,2 m	5211,63	5211,66	
		4,7 m	5208,61	5208,73	
10°	0,25	1,2 m	2095,72	2095,79	
		4,7 m	2094,58	2094,67	
	0,62	1,2 m	5206,45	5206,63	
		4,7 m	5205,29	5205,50	
20°	0,25	1,2 m	2089,31	2089,46	
		4,7 m	2088,72	2088,87	
	0,62	1,2 m	5199,89	5200,27	
		4,7 m	5199,29	5199,68	

TABLE 5.3 Values of SNR for different values of slope, albedo and roughness comparing daylight and night conditions (1064 nm)

From table *5.3*, we can note that the differences between daylight and night conditions are practically negligible for all the values of slope, roughness and albedo. This behaviour of ***SNR*** is a consequence of the fact that the background noise contributes in a minimal way to the total noise and doesn't change appreciably in the passage between night and day. In particular, Ganymede is a very cold body because its temperature fluctuates between a minimum value of about **70** ***K*** during the night and a maximum value

of $\mathbf{152}\ \boldsymbol{K}$ during the day. For these temperatures the spectrum of emission is concentrated around wavelengths greater than that of the laser ($\mathbf{1064}\ \boldsymbol{nm}$). Indeed, using the Planck's law we can verify that for a temperature of $\mathbf{70}\ \boldsymbol{K}$ the emission is significant starting from about $\mathbf{10}\ \boldsymbol{\mu m}$ (figure *5.16*), while for $\mathbf{152}\ \boldsymbol{K}$ this threshold is about $\mathbf{4}\ \boldsymbol{\mu m}$ (figure *5.16*). Therefore the emission of Ganymede at laser wavelength is negligible and not very different between night and day.

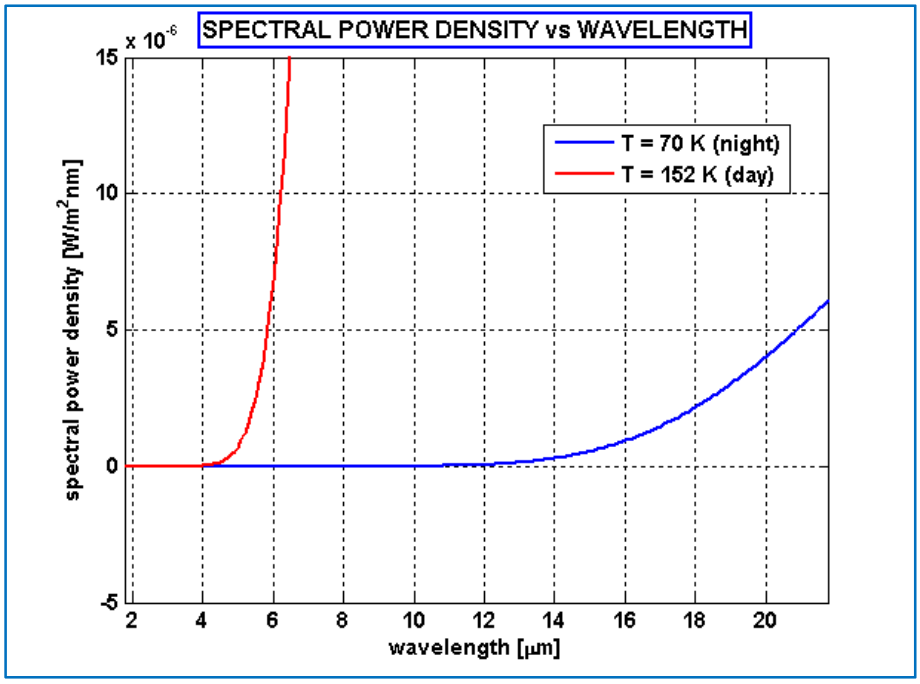

FIGURE 5.16 Spectral power density of a black body as function of wavelength for two different temperature

As for the solar radiation, instead, which is very high at $\mathbf{1064}\ \boldsymbol{nm}$, being the Sun temperature about $\mathbf{5800}\ \boldsymbol{K}$, due to the distance between Ganymede and the Sun (almost $\mathbf{780}$ millions of kilometres), just a very little portion of this radiation reaches the surface of the Jovian moon (about $\mathbf{0,023}\ \boldsymbol{W/m^2nm}$ at laser wavelength). This produces a very reduced noise during daylight conditions, responsible of the small variations in $\boldsymbol{SNR}$ observed during the day with respect to night. Because of the small value of solar irradiance at the distance of Ganymede, also for this contribute to noise there isn't a significant difference between daylight and night conditions.

$\boldsymbol{SNR}$ variations with respect to laser wavelength. As reported in table *3.2*, the laser altimeter for *JGO* has the possibility to operate at a different wavelength of $\mathbf{532}\ \boldsymbol{nm}$.

If this wavelength is adopted, laser beam frequency increases while the number of photoelectrons collected $\boldsymbol{n_S}$ for a certain transmitted energy decreases. At the same time,

also the background noise arises due not to Ganymede's radiation, which practically remains negligible, but to the major solar emission at this wavelength than at $\mathbf{1064}\ \boldsymbol{nm}$. The global effect is to reduce substantially the Signal to Noise Ratio as we can see in figure *5.17*. Moreover, because in this case the difference between night and day in terms of solar emission is greater, the laser altimeter operating at $\mathbf{532}\ \boldsymbol{nm}$ results more sensible to a variation of the conditions (compare figure *5.18* to figure *5.15*).

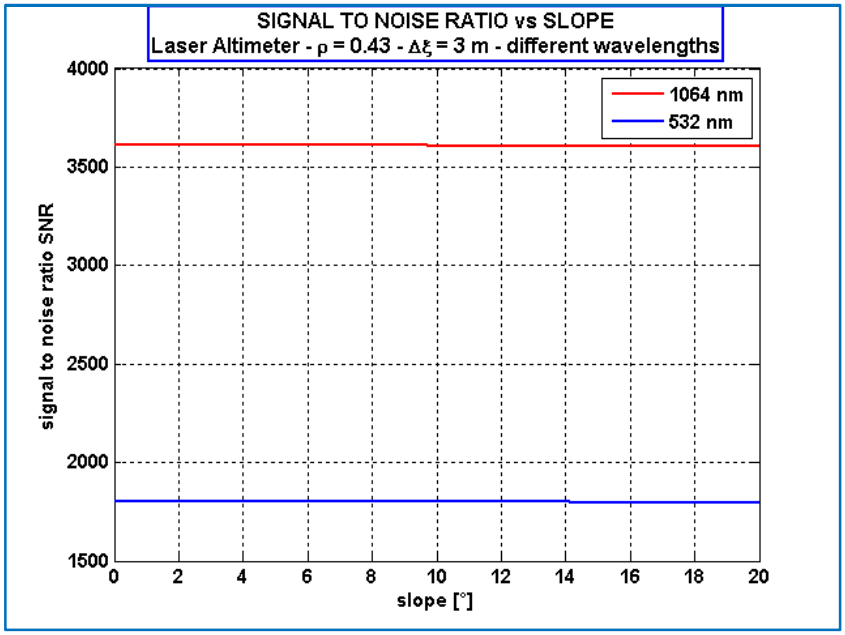

FIGURE 5.17 SNR as function of slope for two different wavelengths (albedo 0,43 - roughness 3 m - daylight conditions)

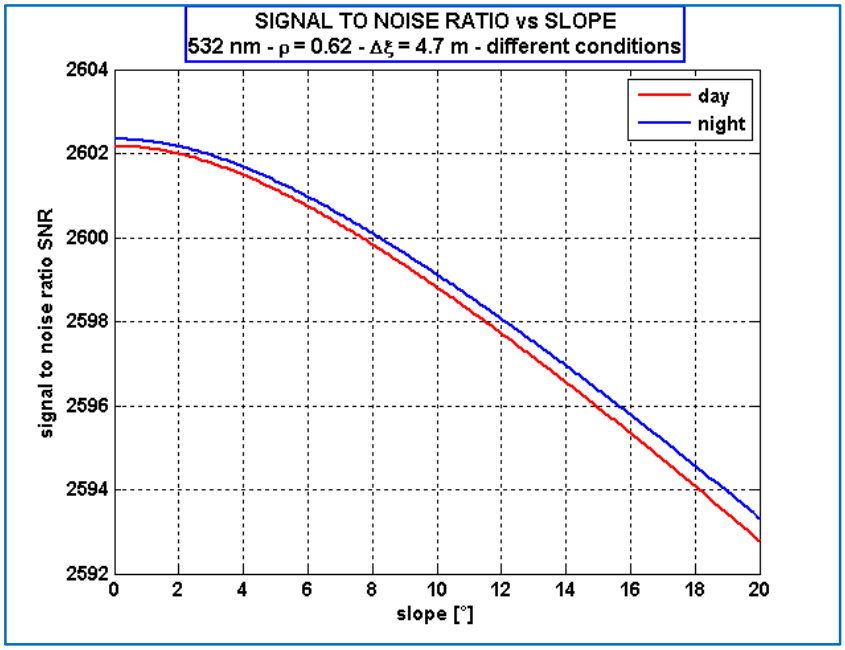

FIGURE 5.18 SNR as function of slope at 532 nm comparing daylight and night conditions (albedo 0,62 - roughness 4,7 m)

5.3 Range accuracy

The range resolution ΔR, that is the error associated with the range measurement, depends on the echo pulse width and on the signal to noise ratio (see *equation (4.5.4)*). In particular, the variations of σ_p and SNR are opposite and produce always the same effect on ΔR, being this quantity directly proportional to the first and inversely proportional to the second. Because the dependence on σ_p is in SNR, the range accuracy is function essentially of the Signal to Noise Ratio, that is slope, roughness, albedo, daylight and night conditions and laser wavelength.

As for SNR, we will analyze the various dependences and results for the range accuracy. Initially, let we suppose a wavelength of $1064\ nm$ and daylight conditions. Let us mention that the *ESA* requirement for range resolution at an altitude of $200\ km$ for all Ganymede surface is $\Delta R = 1\ m$.

***ΔR* variations with respect to slope and roughness.** An increment in slope or roughness leads to a larger echo pulse width and at the same time to a decrement in the Signal to Noise Ratio (see *paragraph 5.1* and *5.2*). Therefore, globally ΔR increases with slope and roughness, since a more irregular surface doesn't favourite the measurement. In figure *5.19* ΔR is plotted as function of slope for three different values of roughness, fixed albedo to its mean value (0,43).

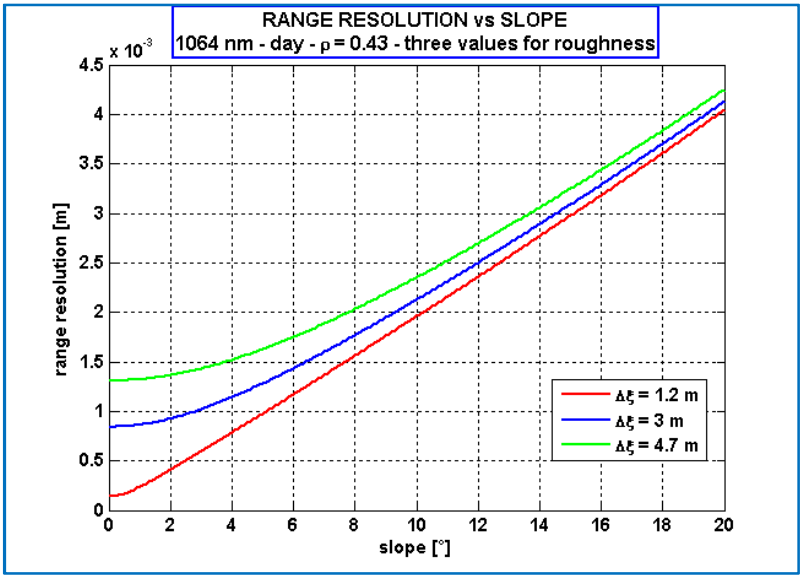

FIGURE 5.19 Range resolution as function of slope for different values of roughness (albedo 0,43 - daylight conditions – 1064 nm)

Also for ΔR the influence of roughness is greater for low values of slope and becomes ever smaller as slope increases. As we can see, the presence of the maximum slope and roughness produces a variation in the range resolution with respect to an ideal surface of just *5 mm*, due to the reduced variations of the Signal to Noise Ratio.

***ΔR* variations with respect to albedo.** The value of albedo has a more relevant effect than slope and roughness. Referring to SNR and σ_p, we expect that the range resolution decreases with albedo. In particular, comparing the curves obtained for the three different values of albedo, we note (figure *5.20*) that a low albedo (fixed slope and roughness) produces a greater error than an high albedo (figure *5.21*): the ΔR value is reduced of about $2/3$. Moreover, the range of variation for ΔR within the interval of slope increases as the albedo decreases according to the Signal to Noise Ratio trend.

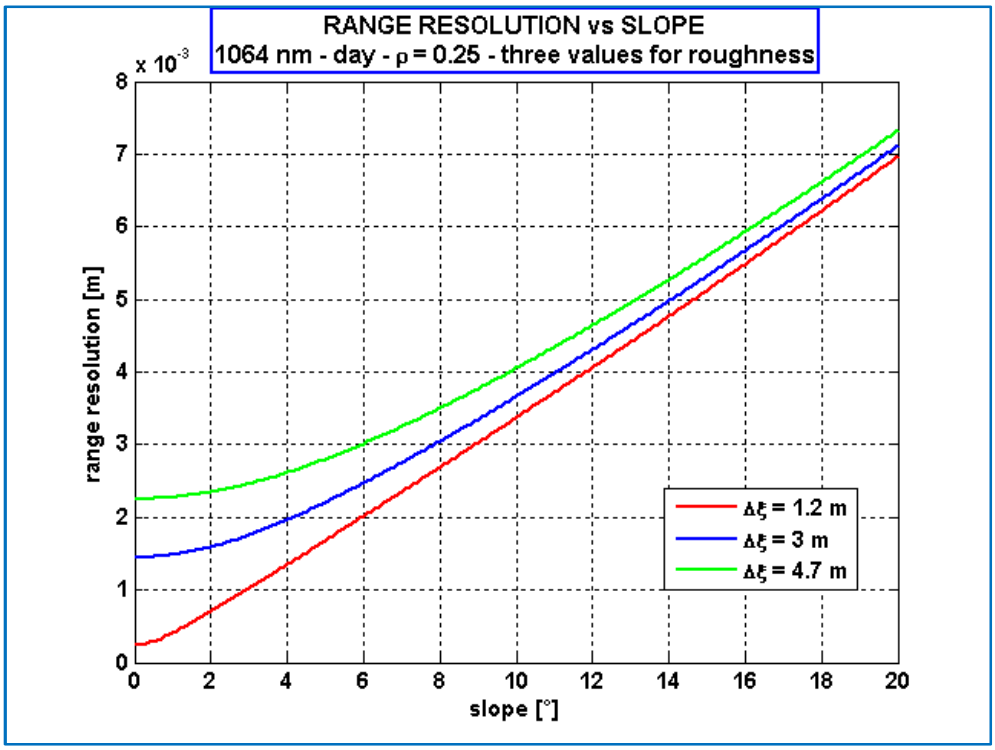

FIGURE 5.20 Range resolution as function of slope for different values of roughness (albedo 0,25 - daylight conditions – 1064 nm

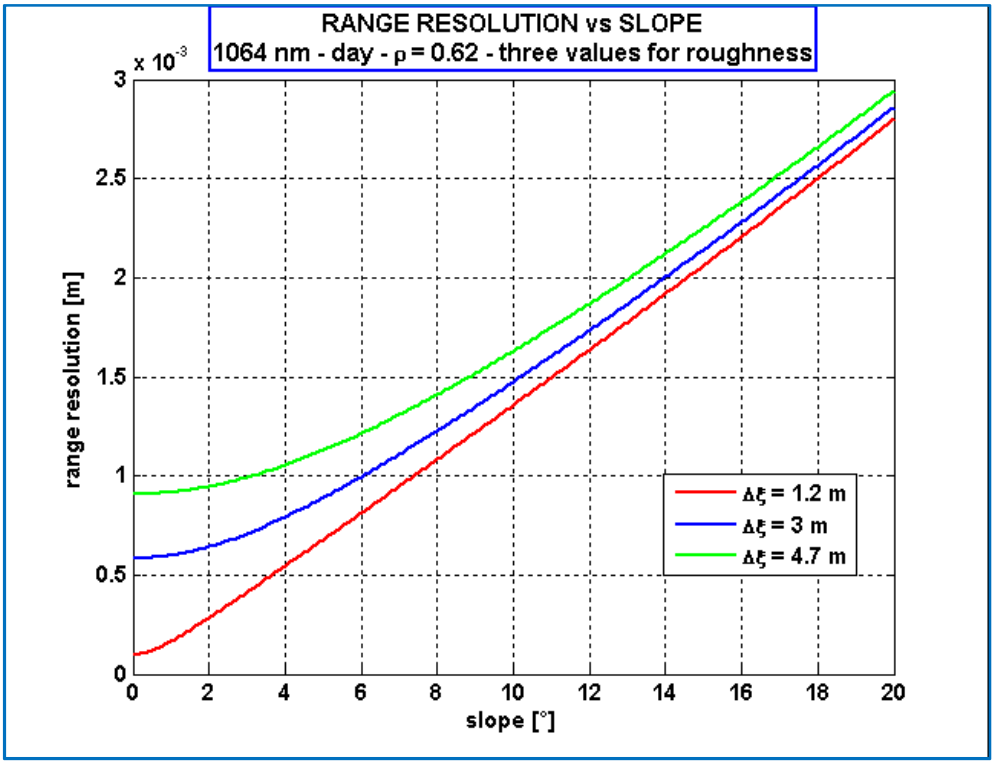

FIGURE 5.21 Range resolution as function of slope for different values of roughness (albedo 0,62 - daylight conditions – 1064 nm

For the range accuracy there is also a combined effect due to the variations of albedo and roughness (figure *5.22* and figure *5.23*). Indeed, if we plot ΔR as function of slope for different values of albedo, fixing the roughness, we note firstly that the variation of albedo is more influent at high slopes, secondly that with an increment in the value of roughness we have smoother curves and major differences among them at low slopes.

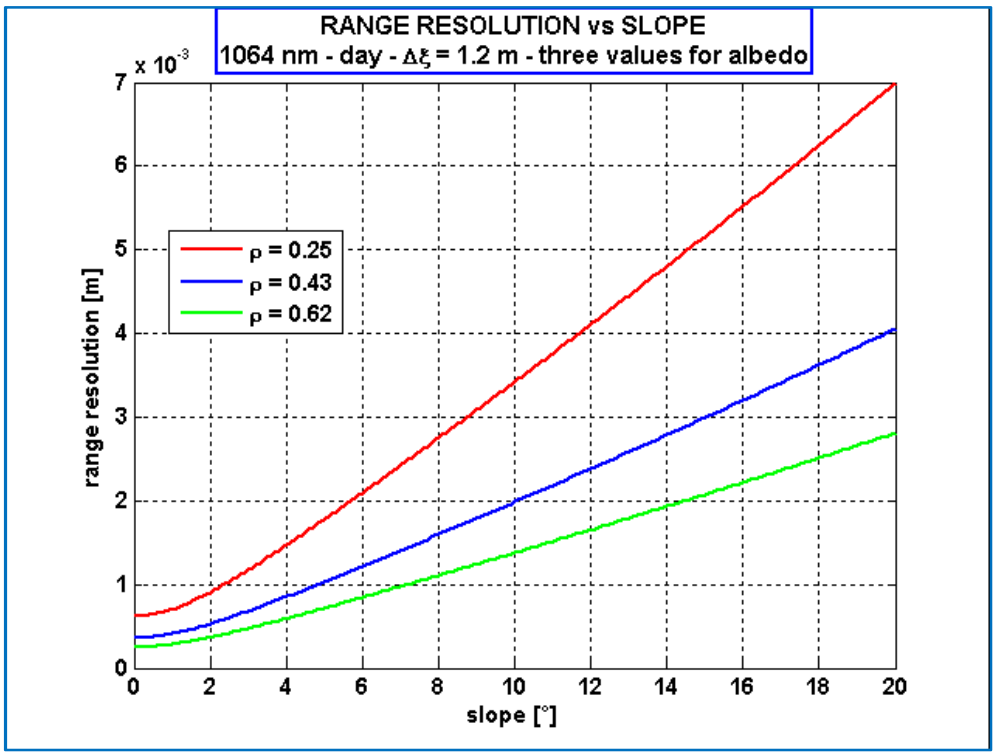

FIGURE 5.22 Range resolution as function of slope for different values of albedo (roughness 1,2 m – daylight conditions – 1064 nm)

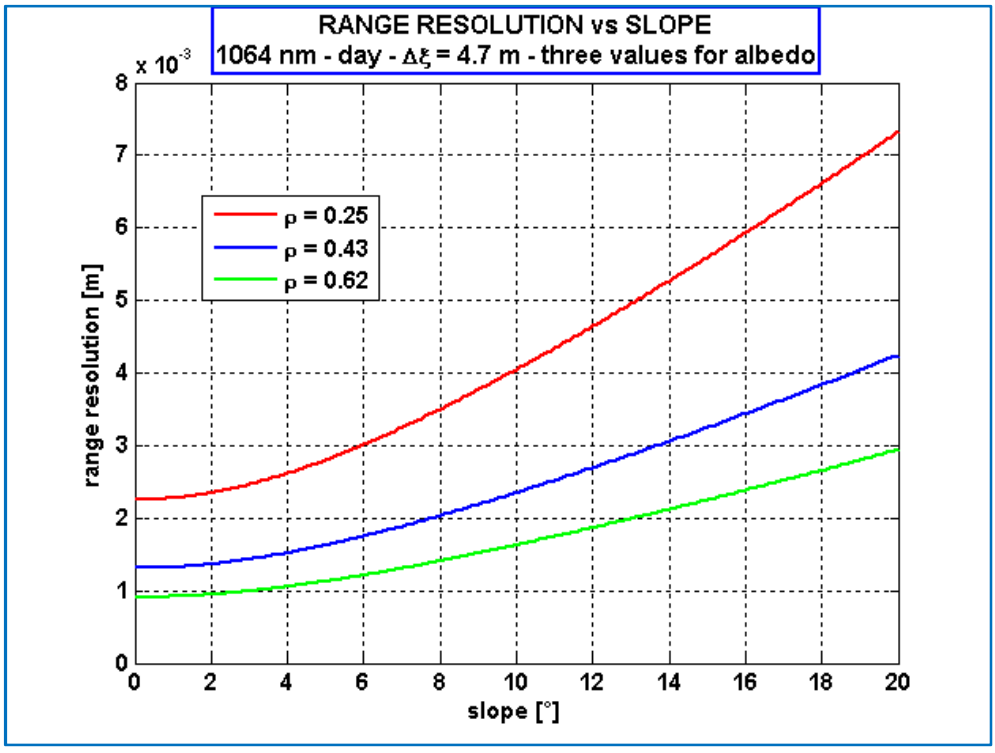

FIGURE 5.23 Range resolution as function of slope for different values of albedo (roughness 4,7 m – daylight conditions – 1064 nm)

As seen for SNR, the temporal profile of ΔR appears as a three-level graph representing the set of values of albedo. The range accuracy at a certain time will be major or minor according to what type of terrain is being pointed by the spacecraft. In figure *5.24*, are reported the ΔR with respect to time curves parameterized for three different values of slope. The differences due to albedo values become greater and greater as the value of slope increases, as previously observed (see *paragraph 5.2*).

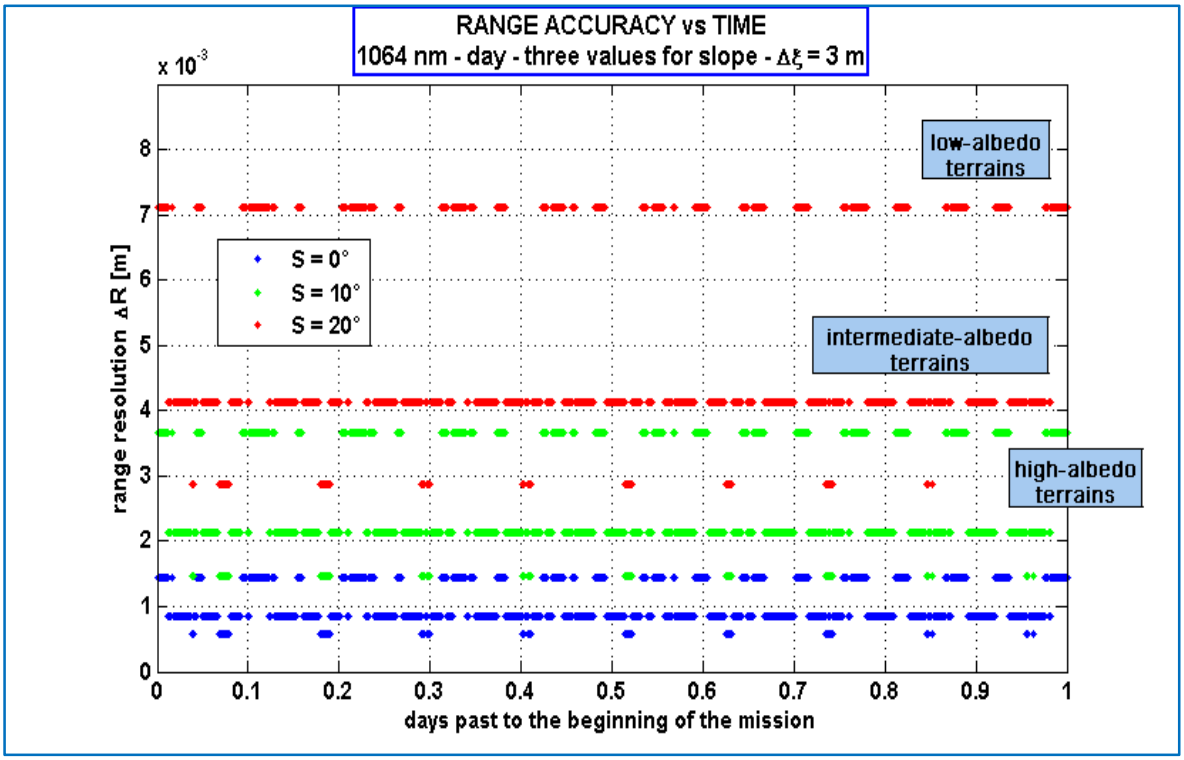

FIGURE 5.24 Range resolution as function of time for different values of slope (roughness 3 m - daylight conditions – 1064 nm)

In order to better appreciate the differences between the several cases, we report the table *5.4* which contains the values for the range resolution for various values of slope, roughness and albedo.

		roughness			
slope	albedo	1,2 m	3 m	4,7 m	
0°	0,25	0,62	1,45	2,25	ΔR [mm]
	0,43	0,36	0,84	1,31	
	0,62	0,25	0,58	0,91	
10°	0,25	3,42	3,66	4,05	
	0,43	1,99	2,13	2,35	
	0,62	1,38	1,47	1,63	
20°	0,25	6,99	7,12	7,33	
	0,43	4,05	4,13	4,25	
	0,62	2,81	2,86	2,94	

TABLE 5.4 Values of range resolution (mm) for different values of slope, roughness and albedo (daylight conditions – 1064 nm)

ΔR variations with respect to daylight/night conditions. Due to the negligible variations in the Signal to Noise Ratio in the passage from night to day, the range resolution is even less influenced by a change of these conditions. Indeed, for any combination of the values of slope, roughness and albedo, the curves representing daylight and night conditions are always superimposed, indicating values practically identical.

ΔR variations with respect to wavelength. If the laser operates at $532\ nm$ instead of $1064\ nm$, as observed in *paragraph 5.2*, we have a substantial diminution in the Signal to Noise Ratio. Therefore we expect that for this wavelength the range resolution has a notable increment as expressed by the figure *5.25*, which reports the comparison between the two possible options cases. It has to be noted how the difference for ΔR due to the laser frequency increases as the slope rises.

Analyzing the trends obtained varying in turn the value of roughness and albedo, it can be found that the differences due to the wavelength options decrease, both for high and low slopes, with an increment of ρ, fixed $\Delta\xi$ while they increase with an increment of $\Delta\xi$ (set ρ) and they are higher for low slopes in comparison with those at high slope. Moreover, also for $532\ nm$, variations between night and day are negligible.

Table *5.5* reports some values for ΔR comparing $1064\ nm$ with $532\ nm$ case.

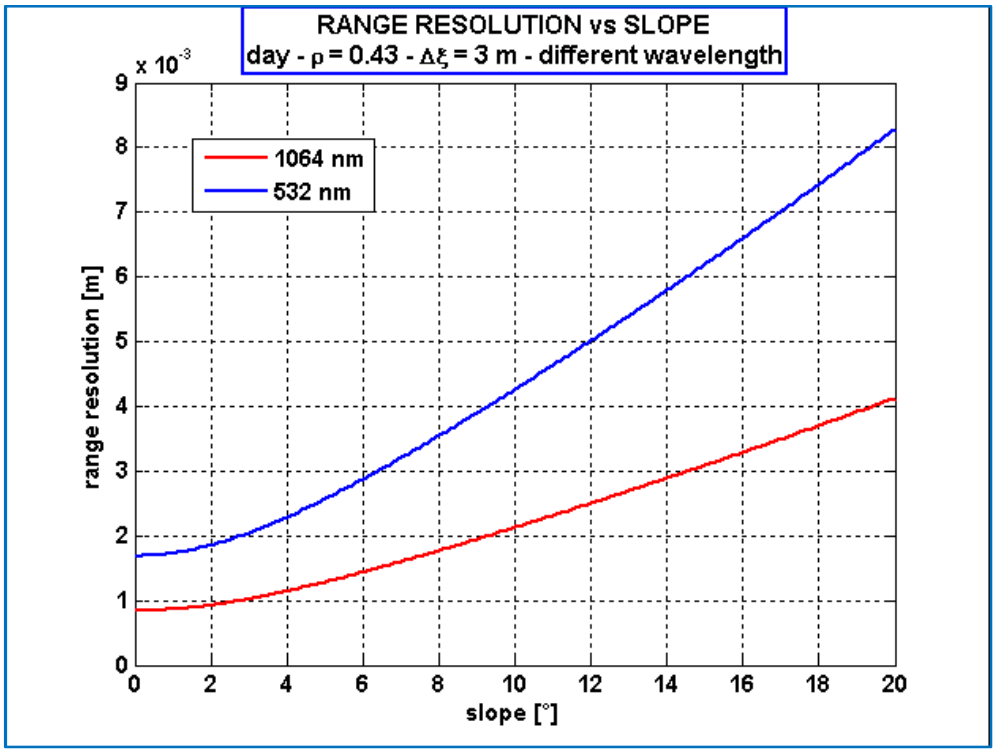

FIGURE 5.25 Range resolution as function of slope for two different wavelengths (albedo 0,43 - roughness 3 m - daylight conditions)

			wavelength		
slope	albedo	roughness	1064 nm	532 nm	
0°	0,25	1,2 m	0,62	1,24	ΔR [mm]
		4,7 m	2,25	4,51	
	0,62	1,2 m	0,25	0,50	
		4,7 m	0,91	1,81	
10°	0,25	1,2 m	3,42	6,87	
		4,7 m	4,05	8,13	
	0,62	1,2 m	1,38	2,76	
		4,7 m	1,63	3,26	
20°	0,25	1,2 m	6,99	14,10	
		4,7 m	7,33	14,75	
	0,62	1,2 m	2,81	5,63	
		4,7 m	2,94	5,90	

TABLE 5.5 Values of range resolution (mm) for different values of slope, roughness and albedo comparing 1064 nm and 532 nm cases (daylight conditions)

5.4 Performance analysis in best and worst conditions

In this paragraph we report the performance of laser altimeter for *JGO* in the best and worst conditions.

In the best case, individuated by the following assumptions

- $S = 0°$
- $\Delta\xi = 1{,}2\ m$
- $\rho = 0{,}62$
- $\lambda = 1064\ nm$
- $night\ conditions$

we get:

- $\sigma_p = 8{,}69\ nm$
- $SNR = 5211{,}66$
- $\Delta R = 0{,}25\ mm$

In the worst case, instead, characterized by

- $S = 20°$
- $\Delta\xi = 4{,}7\ m$
- $\rho = 0{,}25$
- $\lambda = 532\ nm$
- $daylight\ conditions$

we obtain the following values:

- $\sigma_p = 102{,}12\ nm$
- $SNR = 1037{,}77$
- $\Delta R = 14{,}75\ mm$

According to these values, we can assert that the requirement of $1\ m$ for the range resolution is always satisfied in all the operative conditions for the analysed instrument in the reference scenario. The very good performance can be explained considering that we have supposed an ideal receiver for the laser altimeter (with a null response impulse width and with a filter capable to adapt to each echo pulse width) and that the operative scenario

presents low (practically negligible) sources of background noise, mainly due to the low temperatures of bodies like Ganymede and Jupiter and to the enormous distance between the Jovian System and the Sun.

CONCLUSIONS

The performance for the laser altimeter which will board on *Jupiter Ganymede Orbiter* in the framework of *Europa Jupiter System Mission* have been analysed by means a software developed, during this thesis, in MatLab language. The study has pointed out how instrument performance are influenced in an evident manner by the local wide differences in albedo surface values. In same way performance do not appear appreciably sensible to topographical features as slope and roughness and to variations between daylight and night conditions, mainly due to the short range of slopes which characterizes Ganymede and the low difference in day and night temperatures. The laser wavelength, instead, has a fundamental rule: all the results seem individuate $1064\,nm$ as the better solution, both for the Signal to Noise Ratio both for the range resolution.

Although it is evident that there are variations in the performance of the optical altimeter due to the change of the flown over area of surface with the spacecraft motion, the values of range accuracy and of the Signal to Noise Ratio are more than acceptable for all the duration of the mission. In other words, all the possible operative conditions lead to high-quality performance.

The considered scenario appears much favourable for observations in the optic-near infrared spectrum. Indeed, the distance of Ganymede from the Sun reduces background noise at this frequencies and the absence of an atmosphere around Ganymede avoids absorptions of the transmitted light beam.

It has to be noted that the altimeter performance have been analysed during the *Ganymede Science Phase*, which foresees a low circular orbit (altitude $200\,km$): this condition increases the measurements accuracy for the laser altimeter, that will be developed on *BepiColombo Laser Altimeter (BELA)* heritage, which will map Mercury topography (launch on *2012*). The possibility of *JGO* to collect a very high-quality altimetric data will improve in a significant way our knowledge of the topography of Ganymede.

Even if the technology of the so-called classic laser altimeter appears to reach satisfied results, the technology developments direction for spacecraft-based altimetry is toward *Micro Laser Altimeter* based on single photon detection, with the goal of reducing drastically size and dimension of the instrument, maintaining or better improving the

performance. As of this writing this new technology is studied by *ESA*, and most probably, it will represent the future of laser altimetry for spatial applications.

Regards to the developed software, it has the advantage of remaining valid also for different missions scenario employing laser altimeters, changing the instrument and mission parameters.

The implementation of an orbital propagator combined with a performance model allows to better simulate the mission conditions and to analyze the performance for the whole duration of the mission through temporal profiles.

LIST OF ACRONYMS

AOCS	Attitude and Orbit Control Subsystem
APD	Advanced Photo-Diode
AU	Astronomical Unit
BELA	BEpiColombo Laser Altimeter
BOL	Beginning Of Life
CGG	Callisto Ganymede Ganymede
CW	Continuous Wave
DLR	German Aerospace Center
DPU	Data Processing Unit
DSM	Deep Space Manoeuvre
EAM	European Apogee Motor
EJSM	Europa Jupiter System Mission
EME2000	Earth Mean Equator and Equinox at J2000
ENA	Energetic Neutral Atoms
EPS	Electrical Power Subsystem
ESA	European Space Agency
FOV	Field Of View
GCGC	Ganymede Callisto Ganymede Callisto
GGA	Ganymede Gravity Assist
GOI	Ganymede Orbit Insertion

HGA	High Gain Antenna
HST	Hubble Space Telescope
IR	Infra-Red
IRIS	Infra-Red Interferometer Spectrometer
ISRO	Indian Space Research Organization
J2000	12:00:00 of 1 January 2000
JAXA	Japan Aerospace eXploration Agency
JEO	Jupiter Europa Orbiter
JGO	Jupiter Ganymede Orbiter
JMO	Jupiter Magnetospheric Orbiter
JOI	Jupiter Orbit Insertion
JPL	Jet Propulsion Laboratory
LA	Laser Altimeter
LALT	Laser Altimeter
LAPE	Laser Altimeter for Planetary Exploration
LASER	Light Amplification by Stimulated Emission of Radiation
LEOP	Launch and Early Orbit Phase
LGA	Low Gain Antenna
LIDAR	Laser Image Detection And Ranging
LILT	Low Intensity Low Temperature
LLRI	Lunar Laser Ranging Instrument
LOLA	Lunar Orbiter Laser Altimeter
LRO	Lunar Reconnaissance Orbiter

MESSENGER MErcury Surface Space ENvironment GEochemistry and Ranging

MGA Medium Gain Antenna

MGS Mars Global Surveyor

MLA Micro Laser Altimeter / Mercury Laser Altimeter

MLI Multi-Layers Insulator

MMH Mono-Methyl-Hydrazine

MOLA Mars Orbiter Laser Altimeter

MON Mixed Oxides of Nitrogen

MPO Mercury Planetary Orbiter

NASA National Aeronautics and Space Administration

Nd:YAG Neodymium-doped Yttrium Aluminium Garnet

NEAR Near Earth Asteroid Rendezvous

NIMS Near Infrared Mapping Spectrometer

NLR NEAR Laser Rangefinder

OP Orbital Period

PMT Photo-Multiplier tube

PM Prime Meridian

PPR Photo-Polarimeter Radiometer

PPT Peak Power Tracking

RADAR RAdio Detection And Ranging

SELENE SELenological and ENgineering Explorer

Si APD Silicon Avalanche Photo-Diode

SLA Shuttle Laser Altimeter

SNR	Signal-to-Noise Ratio
SSI	Solid State Imaging
SSMM	Solid State Mass Memory
TID	Total Ionizing Dose
TOF	Time Of Flight
TRL	Technology Readiness Levels
TSSM	Titan Saturn System Mission
UV	Ultra-Violet
UVS	Ultra-Violet Spectrometer
VEEGA	Venus-Earth-Earth Gravity Assist
V-NIR	Visible-Near InfraRed
YAG	Yttrium Aluminium Garnet

REFERENCES

Chapter 1 (Europa Jupiter System Mission)

[1] Cosmic Vision page on ESA web site:
http://sci.esa.int/sciencee/www/object/index.cfm?fobjectid=41177.
Last visit on January 2009

[2] Jupiter Ganymede Orbiter Concurrent Design Facility: summary study results (15 July 2008)

[3] Laplace Mission page on ESA web site:
http://sci.esa.int/science-e/www/area/index.cfm?fareaid=107.
Last visit on January 2009

[4] J.P. Lebreton, M. Blanc and the JSD Team: *Science requirement document (SCIRD) for the Jupiter Ganymede Orbiter of the Europa Jupiter System Mission (SCIRD EJSM/JGO)* (25 may 2008).

[5] M. Blanc et al.: *LAPLACE. A mission to Europa and the Jupiter System for ESA's COSMIC VISION programme*. (2008)

[6] J.P. Lebreton: *Europa Jupiter System Mission Jupiter, Ganymede Orbiter (EJSM/JGO), Science presentation.* (21 May 2008)

[7] LAPLACE CDF team: *Laplace Mission Analysis.* May, 21st 2008.

[8] Image from www.arianespace.com
Last visit on Janaury 2009.

[9] Vingione Guido: *Analisi delle prestazioni e progetto preliminare del processing del radar di Cassini in modalità altimetro*, Degree in Aerospace Engineering (2004).

[10] Image from Wikipedia:
http://commons.wikimedia.org/wiki/File:Gravity_assist_moving_Jupiter.svg
Last visit on January 2009.

[11] D. Senske: *Summary of the 2007 Jupiter System Observer Study*. May, 21st 2008.

[12] Reference Payload Definition Document for the LAPLACE Assessment Study. April 25th 2008

Chapter 2 (Ganymede)

[13] Wikipedia "Ganymede (moon)" web page: http://en.wikipedia.org/wiki/Ganymede_%28moon%29. Last visit on January 2009.

[14] J. D. Anderson, E. L. Lau, W. L. Sjogren, G. Schubert, W. B. Moore: *Gravitational constraints on the internal structure of Ganymede*. Letter to Nature, vol.31, November 1996.

[15] NASA JPL web page: http://ssd.jpl.nasa.gov/?sat_elem. Last visit on January 2009.

[16] J. Kwok, L. Procker, D. Senske, C. Jones: *Jupiter System Observer Mission Study: Final Report*. November 2007.

[17] NASA JPL web page: http://ssd.jpl.nasa.gov/?sat_phys_par. Last visit on January 2009.

[18] Data available at http://www.resa.net/nasa/ganymede.htm. Last visit October 2008.

[19] Wikipedia: http://en.wikipedia.org/wiki/Galilean_moons. Last visit on January 2009.

[20] NASA Jupiter web page: http://www.nasa.gov/worldbook/jupiter_worldbook.html) Last visit on January 2009

[21] R. Pappalardo et al.: *Geology of Ganymede*. Chapter 16 of: *Jupiter, The Planet, Satellites and Magnetosphere.* Cambridge University Press.

[22] Wikipedia: http://en.wikipedia.org/wiki/Cassini%E2%80%93Huygens Last visit on January 2009

[23] Wikipedia: http://en.wikipedia.org/wiki/New_Horizons Last visit on January 2009

[24] Image from Nasa JPL web site http://photojournal.jpl.nasa.gov/jpeg/PIA00600.jpg Last visit on January 2009

[25] Tosi Federico: *Osservazione del Sistema di Giove mediante spettroscopia ad immagine*, Degree in Astronomy (2003)

[26] Wikipedia: http://en.wikipedia.org/wiki/Orbital_resonance Last visit on January 2009

[27] Image from http://www.mmedia.is/~bjj/data/ganymede.

Last visit on January 2009.

[28] Astrogeology Organization research program, web page on Gazeteer of Planetary Nomenclature: http://planetarynames.wr.usgs.gov/jsp/FeatureTypes2.jsp?system=Jupiter&body=Ganymede&systemID=5&bodyID=5&sort=AName&show=Fname&show=Lat&show=Long&show=Diam&show=Stat&show=Orig. Last visit on January 2009.

[29] Image from: http://www.nineplanets.org/ganymede.html. Last visit January 2009.

[30] Image from Astrogeology Organization research program: http://astrogeology.usgs.gov/Gallery/MapsAndGlobes/large/ganymede_I2762_map.pdf. Last visit on January 2009.

[31] Image from Galileo Mission imaging diary: http://ciclops.org/ir_index_main/Galileo. Last visit on January 2009.

[32] J. Oberst et al.: *The distribution of bright and dark material on Ganymede in relationship to surface elevation and slopes*. Icarus, 140, 1999.

Chapter 3 (Laser Altimetry)

[33] Wikipedia: http://en.wikipedia.org/wiki/Laser
Last visit on January 2009.

[34] Image from http://www.howstuffworks.com/laser.htm
Last visit on January 2009.

[35] Cipriano Antimo: *Analisi di missione per l'osservazione di Mercurio mediante laser-altimetro,* Degree in Aerospace Engineering (2004)

[36] François Balembois: *The Laser: Basic Principles* (2007). Available at: http://prn1.univ-lemans.fr/prn1/siteheberge/optique/M1G1_FBalembois_ang/co/M1G1_anglais_web.html. Last visit on January 2009.

[37] Bufton J. L. : *Laser altimetry measurements from aircraft and spacecraft*
Proc. of the IEEE,Vol. 77, No. 3, March 1989

[38] CO.RI.S.T.A.: *Laser Altimeters*. Technical report to Italian Space Agency (Agenzia Spaziale Italiana) for Italian Vision for Moon Exploration study, 2007

[39] M.R. Santovito et al.: *A laser Altimeter for BepiColombo mission: Instrument design and performance model*, Planetary and Space Science, 54, 2006.

[40] MLA Messenger web page:
http://messenger.jhuapl.edu/instruments/MLA.html
Last visit on January 2009

[41] Kaguya LALT JAXA web page:
http://www.selene.jaxa.jp/en/equipment/lalt_e.htm
Last visit on January 2009

[42] LLRI ISRO web page:
http://www.isro.org/Chandrayaan/htmls/llri.htm
Last visit on January 2009

[43] LOLA NASA web page:
http://lunar.gsfc.nasa.gov/lola.html
Last visit on January 2009

[44] BELA Bepi-Colombo web page:
http://www.mps.mpg.de/en/projekte/bepicolombo/bela/
Last visit on January 2009

[45] Reference Payload Definition Document for the LAPLACE Assessment Study. April 25th 2008.

[46] H. Hussmann, K. Lingenauber: *Laser Altimeter for JGO*. German Aerospace Center (DLR), Institute of Planetary Research, September 2008.

Chapter 4 (Orbital propagator and laser altimeter performance model)

[47] Izzo Mirko: *Algoritmi di Planning del Radar Sounding Sharad per la Missione Mars Reconnaissance Orbiter*, Degree in Aerospace Engineering (2004)

[48] S. Kemble: *Interplanetary Mission Analysis and Design*, Appendix 2, Springer 2006

[49] R. R. Bate, D. D. Mueller, J. E. White: *Fundamentals of Astrodynamics*, Dover Publication, Inc. 1971

[50] P. D. Burkhart: *MSL Update to Mars Coordinate Frame Definitions* (15 August 2006) available at:
http://www.ae.gatech.edu/people/rbraun/classes/astrol08/MSLCoordFrameMemo.pdf

[51] Spice file data available at:
ftp://naif.jpl.nasa.gov/pub/naif/GLL/kernels/pck/pck00007.tpc

[52] Image from:
http://www.davincisworld.com/Satellites/OrbitalDynamics_files/image040.jpg
Last visit on January 2009

[53] Gardner S. C: *Ranging performance of satellite laser altimeters*
IEEE Transaction on Geoscience and Remote Sensing Vol 30, No. 5, Sept 1992

[54] Harding J. D., Bufton J. L., Frawley J. J. : *Satellite Laser Altimetry of Terrestrial Topography: Vertical Accuracy as a Function of Surface Slope, Roughness and Cloud Cover*, IEEE Transaction on Geoscience and Remote Sensing Vol 32, No. 2, March 1994

[55] Image from U.S.Geological Survey web site
http://www.usgs.gov/
Last visit on January 2009

[56] M.R. Santovito et al: *Performance Analysis Summary Report*. Laser Altimeter for Planetary Exploration Definition Study, 2006.

[57] Gunderson K., Thomas N., Rohner M.: *A Laser Altimeter Performance Model and Its Application to BELA*
IEEE Transaction on Geoscience and Remote Sensing Vol 44, No. 11, Nov 2006

[58] Wikipedia: http://en.wikipedia.org/wiki/Sun
Last visit on January 2009

[59] Wikipedia "Jupiter" web page: http://en.wikipedia.org/wiki/Jupiter
Last visit on January 2009

ACKNOWLEDGEMENTS

Questo lavoro rappresenta, come da tradizione, il coronamento di un percorso di studi durato oltre tre anni in cui il ragazzo pieno di sogni, curiosità e speranze per il futuro, che ricordo con nostalgia in quell'estate alla fine del liceo, ha iniziato a urtare prepotentemente con la realtà e tutte le sue difficoltà.

È iniziata una nuova vita, un nuovo ciclo che oggi si conclude, in cui le speranze a volte sono diventate delusioni e al posto dei sogni mi rimane solo una rabbiosa rassegnazione. Solo la curiosità non è mai diminuita, anzi è cresciuta col tempo chissà se per quella mia ingenuità da irrecuperabile sognatore o perché dentro di me il percorso intrapreso comincia a germogliare.

Ad ogni modo non tutto è negativo. In questi anni, infatti, ho visto nascere nuovi amori intellettuali e crescere quelli che già avevo e quando penso a tutto ciò che mi resta dopo quest'esperienza mi stupisco pur essendo cosciente che non riesco ancora ad apprezzarne tutta la sua portata e importanza.

Facendo un bilancio, la vita universitaria mi ha dato molto ma anche privato di molto e non saprei dire quale delle due cose prevalga. Sicuramente però le difficoltà sono state innumerevoli e se avessi dovuto affrontarle da solo probabilmente non sarei riuscito a venirne fuori. Perciò mi sembra doveroso ricordare in queste pagine finali tutte le persone che, direttamente o indirettamente, in piccola parte o enormemente, mi hanno offerto un sostegno. Tengo a precisare che l'ordine non sempre rappresenta un ordine affettivo.

Per cominciare, voglio ringraziare i miei genitori, mia madre *Liliana* e mio padre *Lorenzo*, e mia sorella *Gaia*, senza i quali non sarei potuto giungere fin qui raggiungendo questi obiettivi. Il loro amore e il loro appoggio morale e anche pratico è stato indispensabile, così come i loro consigli, i loro incitamenti, tutto il tempo perso a causa mia. Mi hanno insegnato quanto di buono ho, a crescere e non esiste nulla di così grande che possa ringraziarli a dovere. Inoltre, mia madre è stata fondamentale per tutti i preparativi della festa di laurea; mio padre mi ha aiutato molto nella stesura e cura della tesi e per ogni problema incontrato nello studio; mia sorella è stata molto gentile sostituendo mia madre quando non c'era e molto divertente, insieme ai suoi amici *Riccardo*, *Paolo* ed *Elisa*, per tutti quei "ironici sfottò" sui miei risultati nello studio che mi hanno spronato a fare sempre meglio.

Un grazie particolare va anche al professore nonché mio relatore *Marco D'Errico*, che mi ha trasmesso tanto nei corsi da lui tenuti e che ha fatto nascere in me una passione smisurata per la meccanica orbitale, forse anche perché si avvicina molto all'astronomia che amo da quando ero bambino. Ricordo con piacere le lezioni del corso di "Astrodinamica" (troppo poche purtroppo) in cui seguivo le sue parole con un interesse mai più provato ed era un piacere ascoltarlo.

Ringrazio molto anche la mia correlatrice dottoressa *Maria Rosaria Santovito* del Co.Ri.S.T.A. per avermi seguito costantemente nel mio lavoro, per aver corretto i miei innumerevoli errori, per tutti i preziosi consigli che non ha mai esitato a darmi (tra cui quello di scrivere la tesi in inglese) e per avermi fatto conoscere come meglio non poteva il mondo lavorativo di cui fa parte. Un ringraziamento anche a tutti i suoi colleghi, in particolare la dottoressa *Giulia Pica* per la gentile accoglienza e l'ingegner *Claudio Papa* per avermi levato molto spesso dai guai con il MatLab.

Un sentito e affettuoso ringraziamento va alla famiglia della mia fidanzata, la madre *Mary*, il padre *Sergio* e la sorella *Stefania* per tutto l'affetto di cui mi hanno circondato, facendomi sentire come un figlio. Il loro continuo interesse per me durante tutti questi anni, le varie chiacchierate e il tempo trascorso insieme è stato per me fonte di tanta allegria.

Davvero grazie al mio amico *Ivano* perché quei pochi mesi in cui abbiamo studiato insieme sono stati davvero piacevoli e fruttuosi e la sua disponibilità e cortesia raramente l'ho trovata in una persona. Indispensabile è stato anche il suo supporto con libri e appunti.

Ringrazio molto anche tutti i miei zii e cugini, in particolar modo mia zia *Maria* e mio zio *Aldo* con mia cugina *Flavia*, mia zia *Claudia* e mio zio *Alberto*, mia zia *Lucy* e mio zio *Fulvio*. Grazie anche a mia nonna *Rita* e ai nonni che ricordo con affetto *Rosa*, *Angelo* e *Carlo*. Tutte queste persone mi hanno accompagnato nella vita e aiutato a crescere.

Ringrazio anche tutti i miei amici (*Claudio*, *Adolfo*, *Giovanni*, *Ettore*, *Susy*, *Francesco*, *Gaia* e *Lello*), i ragazzi conosciuti all'università (soprattutto *Luigi*, *Gennaro*, *Claudio* ed *Umberto*) e i professori universitari.

Alla fine, solo per darle il rilievo che merita, desidero ringraziare la mia amatissima fidanzata *Veronica* che, prima ancora dell'università, mi ha piacevolmente cambiato la vita portando dentro di me emozioni uniche, rinnovando ogni attimo la voglia di vivere e dandomi la forza per superare ogni difficoltà al solo pensiero di poter essere un giorno felici insieme con in braccio un bellissimo bimbo nato dal nostro Amore. Mi è stata

costantemente vicina in ogni momento e particolarmente durante i miei studi, accettando sempre pazientemente ogni mio impegno e difficoltà, anzi cercando di tirarmi sempre su il morale. Forse non sa che basta semplicemente un suo sorriso o uno sguardo con quei suoi bellissimi occhioni azzurri per farmi rinascere. Ringrazio ogni giorno il cielo per averti incontrato, amore mio.

Grazie di cuore a tutte queste persone.

Aversa, 25 Gennaio 2009